NTNU

Norwegian University of
Science and Technology

# Virtual Impedance Techniques for Power Sharing Control in AC Islanded Microgrids

**Anders Bergheim Holvik**

Master of Energy and Environmental Engineering
Submission date: June 2018
Supervisor: Ole-Morten Midtgård, IEL
Co-supervisor: Raymundo E. Torres-Olguin, SINTEF Energi

Norwegian University of Science and Technology
Department of Electric Power Engineering

# Problem Description

This project will focus on developing power sharing control techniques for ac microgrids with multiple distributed generation units. The power-sharing within these generation units will be studied when the microgrid is operating in island mode. In order to provide improved power sharing in such a grid, the use of virtual impedance will be explored using a decentralized approach. The performance will be assessed through simulations.

# Abstract

This thesis focuses on power sharing in low-voltage, islanded ac microgrids. It is motivated by the challenges related to climate change. To achieve a successful integration of renewable energy resources in the power grid, it is likely with an increased use of small distributed generation units. A promising way of organizing these units is by the use of microgrids. With microgrids disconnected from the main grid, several challenges related to current, voltage and power flow control arise. These challenges are studied in this thesis, where a microgrid with two distributed generation units and one load is investigated while operating in island mode. The two distributed generation units in the system are implemented with significantly different output impedances, in order to examine the unequal power distribution.

Distributed control systems are developed for this system, especially focusing on the use of virtual impedances for improved power sharing. Proposed virtual impedance methods are presented. These methods reduce the effect the virtual impedances have on the voltage level.

Three different cases are considered, each of which divided into two subcases. In case 1, the microgrid system is assumed to have predominantly resistive output impedances. The subcases 1 a) and 1 b) consider the use of opposite and conventional droop control algorithms for controlling the voltage and frequency levels. The microgrid considered in case 2 is similar to the one in case 1, but with predominantly inductive output impedances. As in case 1, the conventional and opposite droop control algorithms are utilized in case 2 a) and 2 b), respectively. Case 3 is a reproduction of case 2, but in the selection of virtual impedances, the physical output impedances

are estimated to be 25 % lower than the actual values.

Simulation models are carried out in all of the cases by utilizing the software MATLAB/Simulink. Each simulation case considers the use of physical output impedance only, an existing virtual impedance method and a proposed virtual impedance method. The proposed virtual impedance methods show promising results in all cases, where the power sharing performances are the same as for the existing methods. The voltage drops due to the use of virtual impedances are however significantly reduced. All of the simulation cases show a reduction of at least 90 %.

This master's thesis is a part of the research project FME CINELDI, and the results of this thesis are planned to be verified through laboratory experiments.

Trondheim, June 2018
Anders Bergheim Holvik

# Samandrag

I denne masteroppgåva er det fokusert på vekselspenningsmikronett med lav spenning som opererer i øydrift. Oppgåva er motivert av utfordringane knytta til klimaendringar. For å oppnå vellukka integrasjon av fornybare energikjelder i kraftnettet vil det vere sannsynleg med auka bruk av distribuerte generatorar. Ein lovande måte å organisere desse enhetane er ved bruk av mikronett. Med mikronett fråkobla hovudnettet, oppstår fleire utfordringar knytta til straum-, spenning- og effektkontroll. Denne masteroppgåva tar for seg desse utfordringane, der eit mikronett med to distribuerte generatorar og ein last er undersøkt når det opererer i øydrift. Dei to distribuerte generatorane i systemet er implementert med signifikant forskjell i utgongsimpedans, for å kunne studere effektfordelinga mellom dei.

Distribuerte kontrollsystem er utvikla for systemet, der det er spesielt fokusert på bruk av virtuell impedans for å forbetre effektdeling. Foreslåtte metodar for bruk av virtuell impedans er presentert. Desse metodane vil redusere effekten dei virtuelle impedansane har på spenningsnivået.

Tre forskjellege tilfeller er studert, der kvart av dei er delt inn i to undertilfeller. I tilfelle 1 er det anteke at mikronettet har utgongsimpedansar dominert av resistive komponentar. I undertilfelle 1 a) og 1 b) er det sett på bruk av omvendt- og konvensjonell droop-kontrollar for å styre spennings- og frekvensnivå. Mikronettet i tilfelle 2 liknar på det i tilfelle 1, men med utgongsimpedansen dominert av induktive komponentar. Slik som i tilfelle 1, er den konvensjonelle droop-kontrollalgoritmane brukt i tilfelle 2 a) og omvendte droop-kontrollalgoritmane i tilfelle 2 b). Tilfelle 3 er ein

reproduksjon av tilfelle 2, men når ein velger dei virtuelle impedansane er dei fysiske utgongsimpedansane estimert 25 % lavare enn dei faktiske verdiane.

Simuleringsmodellane er utarbeida ved bruk av MATLAB/Simulink. Kvart simuleringstilfelle tek for seg fysisk utgongsimpedans, ein allereie eksisterande virtuell impedans-metode og ein foreslått virtuell impedans-metode. Dei foreslåtte virtuell impedans-metodane visar lovande resultat i alle tilfella. Desse metodane gjev same effektdeling som dei eksisterande metodane. Spenningsfalla på grunn av bruken av virtuell impedans er redusert signifikant. Alle simuleringstilfella viser ein reduksjon på minst 90 %.

Denne masteroppgåva er ein del av forskningsprosjektet FME CINELDI, og resultata frå denne oppgåva er planlagt å bli verifisert gjennom laboratorieeksperiment.

# Preface

This thesis is the result of my final semester as a student at the Department of Electric Power Engineering at The Norwegian University of Science and Technology (NTNU). The study is carried out as a part of the work package on microgrids in the research project FME CINELDI. In the work of this master's thesis, there are several contributors, and I would like to thank all of you.

In particular, I would like to thank my supervisor Ole-Morten Midtgård for guidance and making it possible to perform this master's thesis.

My greatest gratitude goes to Fredrik Tomas Bjørndalen Wergeland Göthner for invaluable help and discussions. His talent and pedagogical skills have been extremely helpful throughout my year as a fifth year student at NTNU.

I sincerely thank my co-supervisor Raymundo E. Torres-Olguin in SINTEF Energy for sharing his knowledge and experience with me. He has provided guidance in any way, and I am extremely grateful for his help.

Last, but sincerely not least, I want to thank my partner, Nora, for her support and for helping proofreading my report.

# Table of Contents

# List of Tables

# List of Figures

# Abbreviations

| | |
|---|---|
| **ac** | Alternating Current |
| **RES** | Renewable Energy Sources |
| **PV** | Photovoltaic |
| **DG** | Distributed Generation |
| **IEA** | The International Energy Agency |
| **DER** | Distributed Energy Resources |
| **dc** | Direct Current |
| **VSI** | Voltage Source Inverter |
| **PWM** | Pulse Width Modulation |
| **pu** | Per-unit |

# 1 Introduction

## 1.1 Background and Motivation

By March 2018, 195 countries have signed the Paris Agreement [2], due to the large concern climate change is posing worldwide. Thereby, they have commited to contribute to limit the global temperature rise to 2 degrees Celsius [3]. With an increasing global population [4], the world's electricity production has to be changed to a larger extent renewable energy sources (RES) if this goal should be seen as realistic [5].

Promising technologies to contribute to increased use of RES are systems based on resources such as solar, wind, hydro, and biomass [6]. These technologies have received much attention in the global society, which can be shown by the increase in total production from PV-systems and wind-turbines. From 2005 to 2015, the production of these technologies was increased by a multiple of 10 [7].

In order to increase the capacity and perform a successful integration of RES in the power grid, an increased use of small-scale generation units is expected [8]. These will be distributed at different locations in the power grid, referred to as distributed generation (DG) [9, chapter 1]. The use of RES will make the need of power electronic interfaces in the distributed generation units significant [10]. The intermittent behavior of RES will lead to increased challenges for the power system. To increase the power

capacity of a grid, these units can be connected in parallel. This brings new challenges related to the power delivery and stability [11].

The traditional power grid is dominated by unidirectional power flows and production mainly based on large synchronous generators. The development towards more renewable generation leads to, in addition to the already mentioned distributed generation, new aspects such as energy storage units located in the grid. This leads to bidirectional power flows, having customers who both consume and produce energy. These are referred in the literature as *prosumers* [12].

Because of the current evolution within DG, the traditional control techniques based on large, synchronous generators are not necessarily valid in the future power grid [9, chapter 1]. New control techniques have to be developed, which should both meet the new challenges and comply with the advantages related to upcoming technologies and generation units with power electronic interfaces.

The challenges related to the integration of RES can be faced through the approach of a small version of a power system which contains distributed generation and energy storage, referred in the literature as microgrids. The definition of a microgrid includes that it has clearly defined electrical boundaries, local control systems and flexible loads [9, chapter 1]. This can be advantageous for the purpose of integrating DG, secure power supply and meeting challenges related to bidirectional power flows, prosumers and intermittent generation [9, chapter 1]. Microgrids can operate connected to the main grid, but also as isolated grids. The latter mode of operation is frequently referred to as "island mode", and requires some kind of energy storage and local control systems.

In the island mode of operation, control of power flow, voltage and frequency are essential. Each generation unit will include a local control system, which is responsible for the voltage and frequency levels in the mi-

crogrid. This mode of operation can contribute to secure the power supply in case of unintended disconnection from the main grid [9, chapter 1]. It can also contribute to secure the power supply in rural areas without connection to the main grid. According to The International Energy Agency (IEA), 70 % of rural areas without electricity access have to connect to off-grid solutions or mini-grids in order to achieve this access in the future [13]. In the small grids established in these areas, the research on islanded microgrids can be beneficial.

When connected to the grid, microgrids are seen as single units by the main grid, because of their local control systems [14]. The voltage level is normally stabilized due to the main grid, which makes the main control task related to the power supplied from the DG units [15].

The local control system of a microgrid can be utilized by using either a centralized or a decentralized control approach. In a centralized approach, the control systems located at the DG units follow commands from the microgrid's central controller [16]. When utilizing this approach, the central controller can control the different units relative to each other. Compared to a decentralized approach, power flow control and safe operation of the microgrid are simplified [6] [17]. The centralized approach also brings challenges, for instance by the high costs related to the need of communication [9, chapter 1]. The centralized controller is designed for a specific microgrid, which makes it more challenging if the microgrid is expanded with additional units or in case of a DG failure [18]. With the microgrid dependent on the centralized controller, a failure related to the control or its communication can break down the whole microgrid operation.

A microgrid controlled through a decentralized approach has more intelligent controllers located at the DG units compared to a microgrid controlled by a centralized approach[16]. The decentralized control has more challenges related to the interaction between the DG units, including power

flow issues [18] [16], since the control is done locally. With local measurements, this control approach is more reliable when it comes to DG failure or in case of expansions of the microgrid. Because of these advantages, this thesis will focus on the decentralized control approach. This approach has the intention of making a more general study since the controllers are not dependent on a specific microgrid system. Even if the decentralized controllers are less dependent on communication, it is worth to mention that they are not totally communication-less. The communication is related to the higher levels of control, which operates at a relatively slow sampling rate. The consequences of issues related to this communication will, therefore, be smaller than in case of a centralized controller. In this thesis, the high level control is outside of the scope.

The distributed control, located at the DG units, will be the primary focus of this work. The microgrid studied will be operating in island mode, where power flow challenges will be studied in detail, developing control systems for the purpose of a well-functional islanded microgrid. The results of this thesis will form the foundation for future laboratory experiments utilized through the research project FME CINELDI.

## 1.2 Relation to Specialization Project

In the fall of 2017, the author wrote a specialization project entitled "Control of Power Electronics in Microgrids" [19]. Some sections in this thesis contain material reused from the specialization project, where most of the material is modified. The relevant chapter from the specialization project is given in App. J. The sections which include some reused material are:

- Section 2.6 about the voltage source inverter.
- Section 3.4.1 about different droop control algorithms.
- Section 3.4.3 about virtual impedance.

- Section 3.1 about circulating currents.
- Section 3.2 about the hierarchical control structure.
- Section A about the park transform.

## 1.3 Objectives

The general objective of this master thesis is to:

- Investigate control of power sharing in low-voltage islanded ac microgrids with linear loads.

In particular, the following objectives have been considered:

- Develop a distributed control system for paralleled DG units operating in an islanded microgrid.
- Investigate how virtual impedance can be used with droop control algorithms to improve power sharing.
- Examine the concepts through a developed microgrid system in MATLAB/Simulink.

## 1.4 Methodology and Scope

In order to achieve the aforementioned objectives, this thesis will study the local control systems in a three-phase islanded ac microgrid. It considers a decentralized control approach, focusing on the distributed control. The higher levels of control are assumed to be ideal i.e. the controllers provide constant references to the inner controllers under study.

The microgrid investigated is loaded with a single linear load, modelled as a constant impedance. Neither harmonic oscillations or losses related to the inverters are taken into consideration. The system is assumed to be

balanced, and it is focused on the steady-state behavior. Two DG units are considered in the microgrid, and these are modelled as ideal dc voltage sources. To study the power sharing performance, the impedances of the distribution lines connected to the DGs are significantly different. The goal is to make the two DG units equally share the power drawn from the load.

The microgrid system is modelled in MATLAB/Simulink, where local control systems for the inverters connected to the two DGs are developed. This includes current and voltage control. Active and reactive power are controlled by regulating the voltage and frequency. This is utilized through droop control algorithms and the use of virtual impedances.

## 1.5 Outline

This section presents the outline of the thesis.

Chapter 2 presents the microgrid system used in this thesis. Some of the microgrid's fundamental components are explained, in addition to important definitions.

In chapter 3, it is elaborated on power flow control in microgrids. Definitions, including common control structures, are explained before the control systems utilized in this thesis are studied in detail. In this chapter, concepts such as droop control and the use of virtual impedance are introduced. Both already existing virtual impedance methods and proposed solutions will be elaborated on.

Chapter 4 presents the case studies utilized through this work. Six different cases are considered, where the use of droop control and virtual impedances are the primary focus. This chapter is summarized with a discussion of the results, related to the theory presented in chapter 3.

Finally, chapter 5 provides the final remarks in the thesis.

# 2 System Description

In order to study the control of power sharing in ac microgrids and examine control concepts, a specific microgrid system is used. This chapter will present the system, including some of its most important components. Lastly, the per-unit system used in this thesis will be presented in this chapter.

## 2.1 Microgrid System

Microgrids exist in many forms, in terms of distributed energy resources (DERs), loads, and topology. The complexity and behavior are dependent on the number of loads and DERs, in addition to their characteristics. This study will aim for a generalization, and the conclusions drawn can therefore indicate consequences in other microgrids. The investigated system is chosen on the basis of this generalization.

The system examined in this thesis is depicted in Fig. 2.1. As shown in the figure, the microgrid includes one residential load, represented as a linear, resistive-inductive component. In order to secure reasonable values for the system, a microgrid benchmark presented in [20] is used.

The microgrid has two DG units, where each of them is connected to an LCL-filter in order to reduce harmonic oscillations. Both of the DG units are modelled as ideal dc voltage sources, which means that a conversion

from dc to ac-voltage has to be done in order for the units to operate in an ac microgrid. For this purpose, Voltage Source Inverters (VSIs) are used, which will be elaborated in section 2.6.

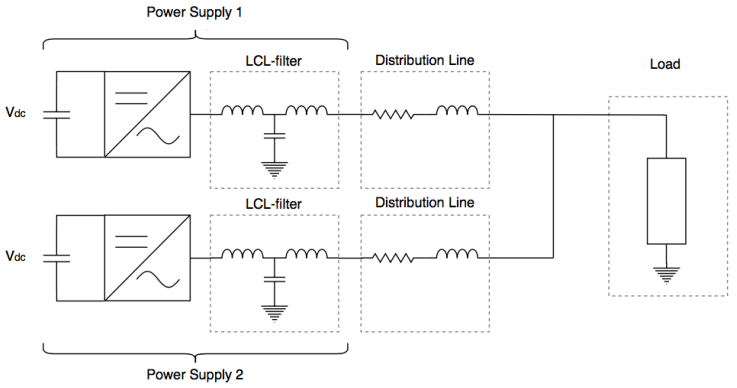


**Figure 2.1:** The investigated system

In general, microgrids can operate both grid-connected and isolated from the main grid. The difference between the two modes are significant, both in terms of advantages and challenges. In grid-connected mode, the microgrid can both import energy from and export energy to the main grid. As seen from the microgrid, the main grid can be considered as stiff, which means that it governs the voltage and frequency levels in the system [21]. In this mode, the voltage control is less complicated compared to the island mode of operation. The inverters are normally controlled to inject power according to maximum power point tracking of the DG units [15]. The grid-connected mode also allows the microgrid to provide ancillary services to the main grid, including reactive power supply and contribution to energy demand management [9, chapter 3].

Microgrids operating in island mode are not electrically connected to the main grid. Thus, the main grid will not affect the microgrid's operation. In this mode, voltage and frequency levels are exclusively controlled by the DG units, connected through VSIs. This makes the power sharing among

several DG units challenging in an isolated microgrid, for instance, due to a difference in line impedances, different voltage levels or local loads [22]. Challenges related to power sharing will be the primary focus throughout this thesis. The microgrid in Fig. 2.1 will be the investigated system, used to highlight both challenges and solutions. Circulating currents and power sharing issues while operating in island mode will be the main concern, focusing on control techniques to solve issues related to this.

In the following, components and definitions that play a central role in this thesis will be introduced, beginning with the distributed generation.

## 2.2 Distributed Generation

The main objective of this thesis is to study the power sharing among the inverters connected to the DG units in the microgrid system. The DG units are modelled as ideal dc voltage sources. This modelling does not take the size of these units, neither in terms of power or storage capacity into consideration. Both inverters are assumed to produce the required amount of power at any time, where the goal is to make the two inverters equally share the load drawn from the load.

## 2.3 Low-Pass Filter

In order to filter high-frequency harmonics, low-pass filters are located at the inverters' output. When selecting this kind of filter, there are several options. The harmonics can be filtered through a simple inductor, referred to as an L-filter. Two other common alternatives are LC- or LCL-filters, both designed by a combination of inductors and capacitors [23].

The low-pass filters selected for this work are LCL-filters, which of the alternatives is the cheaper since the inductors can be smaller than when us-

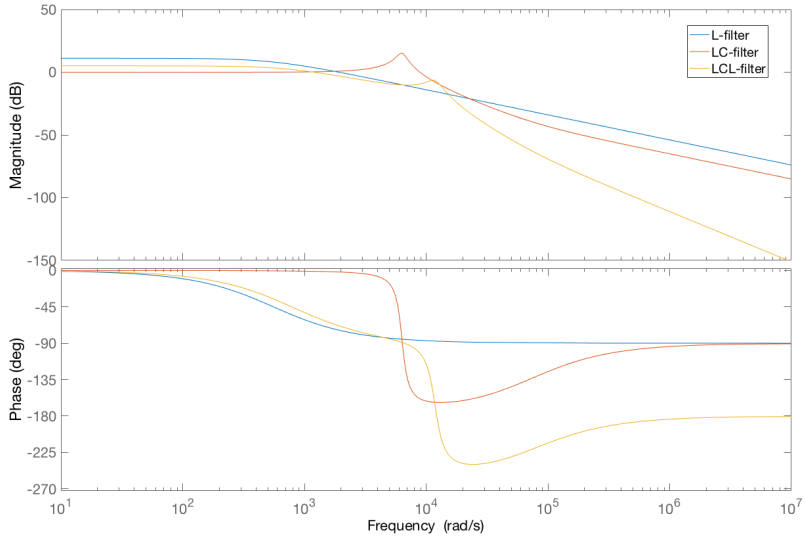


**Figure 2.2:** Bode plots for three different low-pass filter alternatives

ing L- or LC-filters [24]. The use of filters including capacitors also ease the inverters' voltage control, as will be further explained in Chapter 3. A disadvantage of using the LCL-filter is a resonant peak at the cut-off frequency [23]. This frequency has to be selected to differ significantly from the inverter's switching frequency, in order to avoid amplification of possible harmonics. A comparison between the L-, LC- and LCL-filter is shown in the bode plot in Fig. 2.2. The figure depicts the resonant peak and shows that the LCL-filter provides a strong attenuation for high frequencies. An LCL-filter is illustrated in Fig. 2.3. In this figure, $L_1$ denotes the inverter-side inductor, while $L_2$ is the inductor on the grid-side. $R_1$ and $R_2$ are their belonging resistances. $C$ is the filter capacitor, with its resistance, $R$. From Fig. 2.3, the resonant frequency and the transfer function can be derived [25] [26]. This transfer function, including the transfer functions for the L- and LC-filter are shown in App. B.

In addition to the aforementioned arguments, the LCL-filters are the

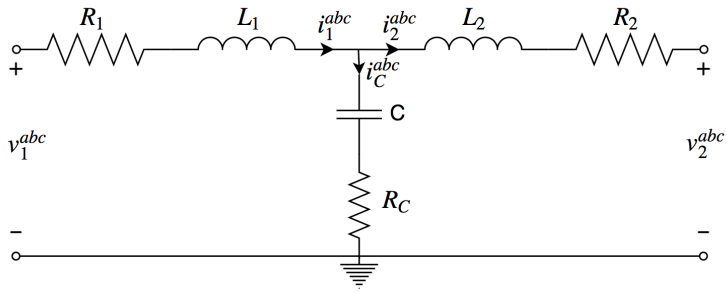


**Figure 2.3:** Schematic of a low-pass LCL-filter

available low-pass filters in the smart grid laboratory available for SINTEF Energy and NTNU. The inductors and capacitors in these filters are listed in Tab 2.1. In order to make the work useful for further research, it is convenient to make the simulations match the available laboratory equipment.

| **Parameters** | **Value** |
|---|---|
| Inverter Side Inductor | 500 $\mu$H |
| Grid Side Inductor | 200 $\mu$H |
| Capacitor | 50 $\mu$F |

**Table 2.1:** Parameters of the LCL-filters available in the Smart Grid Laboratory

### 2.3.1 Filter Resistors

The resistances in the inductors and the capacitor, $R_1$, $R_2$, and $R_C$, are relatively low. In [25], values are provided by Siemens AS in Trondheim. The resistances are in this publication given as 1 % in per unit, which is the same value assumed in this thesis. The LCL-filters with and without these resistances have similar behavior, as shown by the bode plots in Fig. 2.4. A comparison between the two alternatives shows that the resistors have negligible influence on the filters' resonant frequency. Since the behavior

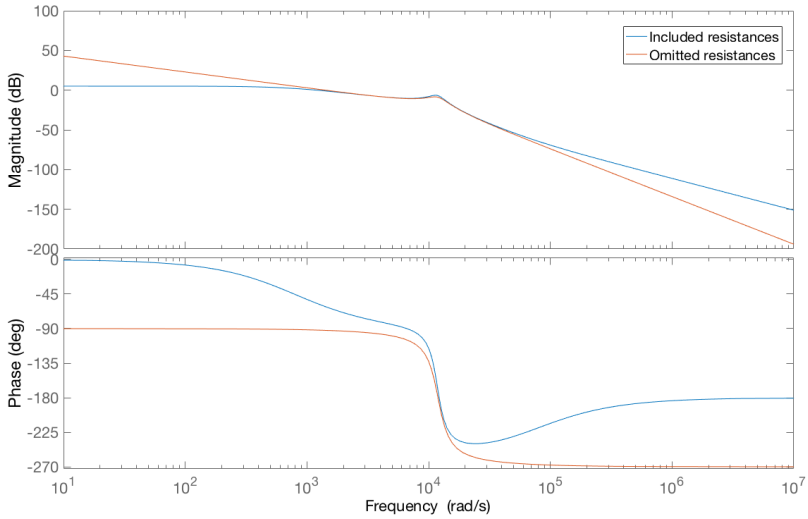


**Figure 2.4:** Bode plots for LCL with internal resistors included and omitted

of the filters is similar without the resistors, $R_2$ and $R_C$ are omitted in this work's analyses. A small inverter-side resistor is however included since this is used to select parameters for the inner controllers in Section 3.3. The bode plots are given in Fig. 2.2 and 2.4 are provided by the MATLAB script given in App. C.

## 2.4 Distribution Lines

The distribution lines in a grid are dependent on the voltage level used for power transfer. This work focuses on a low-voltage microgrid, and as shown in Tab. 2.2 [1], these feeders will typically be dominated by the resistive components.

As will be further explained in Section 3.4.1, the power sharing control techniques used in this work are highly affected by the values of the line impedances, in addition to possible components located between the

| Type of Line | R [Ω/km] | X [Ω/km] | Ratio, R/X |
|---|---|---|---|
| Low Voltage | 0.642 | 0.083 | 7.7 |
| Medium Voltage | 0.161 | 0.190 | 0.85 |
| High Voltage | 0.06 | 0.191 | 0.31 |

**Table 2.2:** Typical line parameters for different voltage levels [1]

load's connection and the power supply. In order to study these effects, the distribution lines in this thesis are modelled as a combination of resistors and inductors. A balanced system is assumed, and the three lines in a three-phase system are considered equal.

The line impedances in this thesis will have a similar R/X-ratio as in Tab. 2.2. Low-voltage lines with an R/X-ratio of 7.7 will be used, which correlates with the low-voltage microgrid in [20], where the lines have a ratio between approximately 3 and 10. The lengths of the distribution lines in this thesis are 500 meters and 800 meters.

In some of the investigated cases, the grid includes components that contribute to a more inductive behavior, such as isolating transformers. Shorter distribution lines are considered in these cases, which give a total output impedance equal to the impedance of the 500 meter and 800 meter lines. This includes both the inductive components and the line impedances. The total output impedance of the inverters will in these cases have an R/X-ratio of 0.31, equal to the high-voltage lines given in Tab. 2.2. The equivalent inductance of the inductive components is then close to the value used for isolating transformers in [27], which is used to secure that reasonable values are used.

## 2.5 Load

The investigated microgrid system contains one linear load shared by two inverters. The load is chosen resistive-inductive, in order to be able to

study both the active and reactive power flow. It is modelled as a constant impedance, adjusted to extract the nominal power at the nominal voltage. By (2.1), it is evident that a reduced voltage level will lead to a decreased power to the load. In this equation, $V_{LL}$ is the amplitude of the voltage across the load, while Z is the load's impedance. The load's apparent power is denoted as S.

$$S = \frac{V_{LL}^2}{Z} \tag{2.1}$$

The size of the load is chosen to model a residential load, as given in the benchmark microgrid [20]. The load consists of both a resistive and an inductive component, which is convenient in order to study both the active and reactive power sharing.

## 2.6 Voltage Source Inverter

A VSI is used to convert the dc-voltage to ac-voltage by using semiconducting switches. Since the DG units are based on dc-voltages, the VSIs are central in the operation of the microgrid under study. The local control of the microgrid is also done through a control system for each VSI. A representation of a three-phase VSI is shown in Fig. 2.5, having an input dc-voltage $V_{dc}$ and output line-to-line voltage $V_{LL}$.

The output voltage $V_{LL}$ is decided by the VSI's switching, in addition to the input dc-voltage at the inverter [28, chapter 8]. The semiconducting switches in the VSI are controlled through a separate control circuit, often by pulse-width modulation, which is described in the following section.

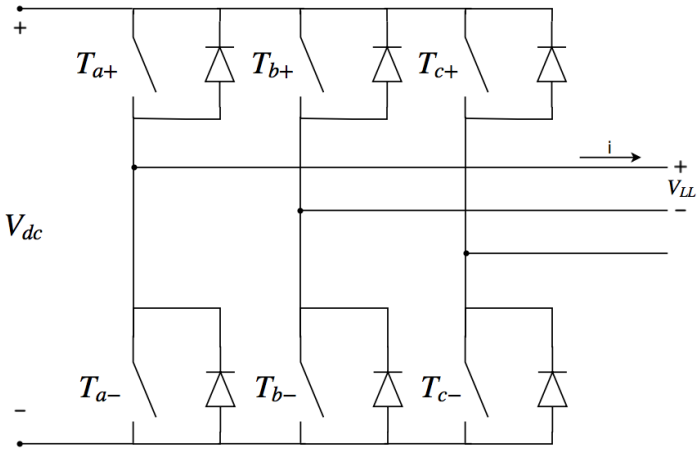


**Figure 2.5:** Representation of a voltage source inverter

### 2.6.1 Pulse-Width Modulation

To control the VSI's semiconducting switches, the sinusoidal pulse-width modulation (PWM) technique is frequently used. The method uses a voltage control signal, $v_{control}$, in comparison with a high-frequency triangular waveform. This is denoted $v_{tri}$, and is often called the carrier signal. The control signal represents the reference output voltage, and typically has an amplitude of 80 % of the triangular wave [28, chapter 8].

A PWM-scheme for phase $a$ in a three-phase system is shown in Fig. 2.6. With Fig. 2.5 as a basis, the switch $T_{a+}$ conducts if $v_{control} > v_{tri}$, while it is open when $v_{tri} > v_{control}$. This results in an output phase voltage as shown in the Fig. 2.6. The switching frequency of the semiconducting switches is equal to the frequency of the carrier signal [28, chapter 8]. The control signals of the three phases are 120 ° shifted, where all of the phases are compared to the same triangular wave. The three phases are by this method controlled independently of each other [28, chapter 8].

The output voltage in Fig. 2.6 is a sinusoidal wave including high fre-

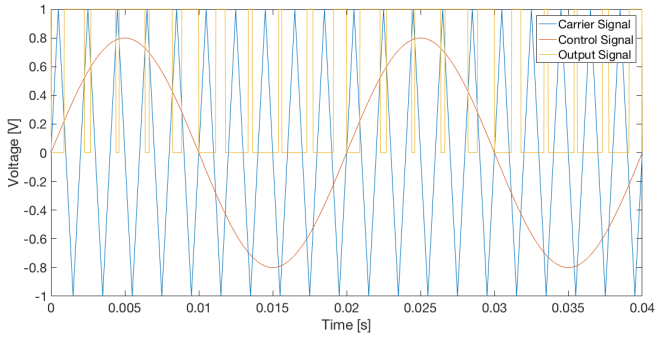


**Figure 2.6:** Pulse-width modulation

quency components. In order to filter out high-frequency components, a low-pass filter can be used, resulting in a sinusoidal waveform at the output of the filter. Harmonic oscillations appear as multiples of the switching frequency, and should be minimized in the output voltage [28, chapter 8]. The voltage signal will also be affected by switching losses, blanking time and on-state losses. Converter losses and harmonic components are both beyond scope of this thesis. Therefore, the inverters, including the semiconducting switches, are assumed to be ideal and lossless in the development of the controllers. It is worth to mention that the frequency of the carrier signal in Fig. 2.6 is chosen very low, in order to clearly illustrate the PWM-operation. This signal will normally have a much higher frequency compared to the control signal.

### 2.6.2 Average Model VSI

An inverter without harmonic components will appear as a voltage source with purely sinusoidal outputs. This can be obtained by using an average model VSI. In addition to harmonics, the average model does not take losses related to the inverter or the detailed topology into consideration [29]. However, this modelling approach of a VSI is still satisfactory when

the phenomena studied are related to the fundamental frequency. Because of the simplifications done when using the average model, simulations can be performed with a larger step size compared to the PWM. Therefore, the computational time related to simulations can be reduced. In Fig. 2.7, a representation of an average model VSI is depicted. The output voltage of the inverter is represented by $v_a$, $v_b$ and $v_c$, which are measured after the filter resistance, R, and inductance, L, on the ac-side. $V_{dc}$ is the input dc-voltage at the average model inverter.

In Fig. 2.8, the output signal from a VSI in MATLAB/Simulink is shown both by using the average model and a switching model where a PWM with the switching frequency assumed in this thesis is used. The switching frequency is chosen on the background of a datasheet for an inverter with similar voltage and power rating [30]. Only one of the phases are shown. By studying this figure carefully, it can be observed that there are slightly more harmonics at the output of the switching model. These harmonics are not a part of this study. Thus, the average model is used in this work's simulations, due to its reduced computational time [31].

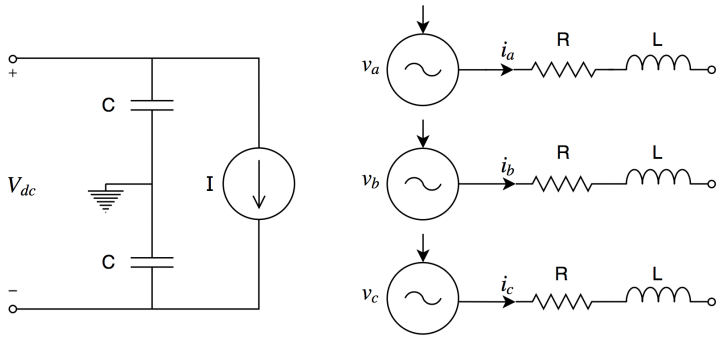


**Figure 2.7:** Schematic showing a three-phase average model VSI

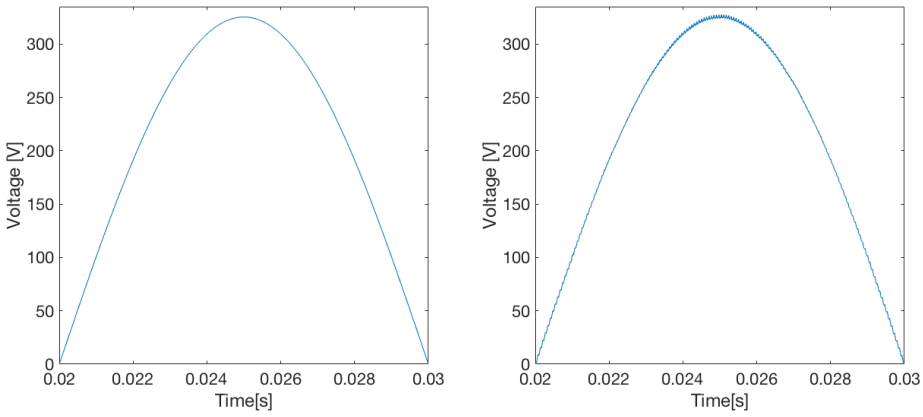


(a) Average model (b) Switching Model

**Figure 2.8:** The output voltage from an average model and switching model VSI

## 2.7 Per-Unit System

In order to simplify calculations and utilize a generalization, the per-unit (pu) system is used in the representation of the physical quantities. These pu-values are given by a set of base-values, defined in (2.2) to (2.6). The nominal line-to-line voltage, current and frequency are denoted by $V_n$, $I_n$ and $f_n$. The subscript *base* denotes base values, where V, I, S and $\omega$ denote voltage, current, apparent power and frequency.

$$V_{base} = \frac{\sqrt{2}}{\sqrt{3}} V_n \tag{2.2}$$

$$I_{base} = \sqrt{2} I_n \tag{2.3}$$

$$S_{base} = \frac{3}{2} V_{base} I_{base} \tag{2.4}$$

$$Z_{base} = \frac{V_{base}}{I_{base}} \tag{2.5}$$

$$\omega_{base} = 2\pi f_n \tag{2.6}$$

The base values for inductance and capacitance are then given by (2.7) and (2.8).

$$L_{base} = \omega_{base} Z_{base} \tag{2.7}$$

$$C_{base} = \frac{1}{\omega_{base} Z_{base}} \tag{2.8}$$

The use of the pu-system is of particular interest in the microgrid's control system. The following chapter will elaborate on control of islanded microgrids, focusing on power sharing challenges in particular.

# 3 | Power Flow Control

In order to be able to develop power sharing control techniques, challenges and solutions related to the topic will be presented in this chapter. First, circulating currents will be defined and discussed. Subsequently, the control structure used in this work will be presented, including a more detailed explanation regarding each control level. This includes voltage and frequency control, droop control techniques and elaboration on how virtual impedances can be used to improve the power sharing performance.

## 3.1 Circulating Current

The use of paralleled inverters is advantageous when it comes to increased reliability and power rating, and is also one of the characteristics of islanded microgrids [11]. However, this organization of DG units also brings challenges. The generation of circulating currents is one of these, which will be presented in this section.

DG units operating in parallel with different output voltages, output impedance or phase can cause currents not only flowing from the generation to the loads but also between the generation units. These currents are referred to as circulating currents, and can be large and potentially damaging. In a traditional power grid with large synchronous generators, the line impedances normally reduce these currents, while the smaller line

impedances in microgrids make the circulating currents a major challenge [14].

The circulating currents can lead to increased losses and overloaded inverters, in addition to reductions in power quality and efficiency [32]. Since the voltages in islanded microgrids are set by the paralleled inverters without a stiff grid, the challenges related to circulating currents are of particular interest in this mode of operation [14]. As mentioned in Chapter 1, a decentralized control approach has more issues related to circulating currents than a centralized controller, where there are fewer challenges related to the interaction between the inverters [18] [16].

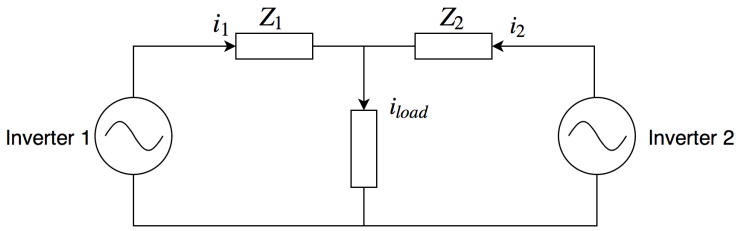


**Figure 3.1:** Two inverters with different line impedance, delivering power to the same load

To illustrate the concept of circulating currents, a single-phase system where two inverters feed a load with a load current $i_{load}$ is shown in Fig. 3.1. The ideal relative load of inverter $j$ is given by $h_j$, while the output impedance, the total impedance located between the inverters' output and the load, is given as an impedance, $Z_j$. The sum of the relative loads of n inverters is given by (3.1). With an actual current from inverter $j$ given as $i_j$, the circulating current from this inverter, $\Delta i_j$, is defined as in (3.2) [33].

$$\sum_{j=1}^{n} h_j = 1 \tag{3.1}$$

$$\Delta i_j = i_j - h_j \cdot i_{load} \tag{3.2}$$

Ideally, (3.1) and (3.2) show that the circulating currents of all inverters are zero. A case where the two inverters in Fig. 3.1 are meant to share the load equally can, for instance, be considered. If the two inverters each feed 50% of the load, no circulating current will occur. With one of the inverters having a relative load which differs from the ideal, circulating currents may be generated, causing the aforementioned issues. This can typically be the situation for two inverters with equal output voltage, but different line impedance. This case will be further investigated in this thesis.

In an unbalanced three-phase system, circulating currents can occur between the phases, making the challenge even more complex [33]. This is however not considered in this thesis, due to the assumption of a balanced three-phase system. This assumption also makes the definition of circulating current presented in (3.2) valid for a three-phase system, which will be used further in the analyses.

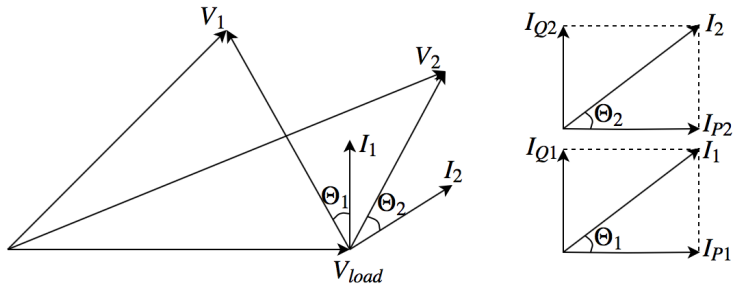


**Figure 3.2:** Active and reactive component of circulating currents

In order to obtain a more accurate analysis, the active and reactive components of the circulating currents can be considered separately as shown in Fig. 3.2 [33]. In this figure, $V_{load}$ denotes the voltage at the load's connection point, while $V_1$ and $V_2$ denote the output voltage of their respective

inverters. The output currents of the same inverters are given as $I_1$ and $I_2$, where $\Theta$ denotes the angle between the voltage and the current. Each of the currents can be divided into an active and reactive component, with subscript P and Q, respectively. The difference between the two inverters active output current will give the active circulating current, while the difference between the reactive currents will give the reactive circulating current.

This classification is done in [34], where the analysis shows which parameters effect the active and reactive power flow. Here, a two-inverter system with equal phase voltages and similar line impedances is assumed. The paper shows that a difference in output voltage may cause both active and reactive circulating currents. The effect of these two components is dependent on the grid's R/X-ratio, in addition to the control methods used. In order to design a control system which limits the generation of circulating currents, a more thorough analysis of the active and reactive power flow is given in Section 3.4.1.

In the following, this thesis will focus on minimizing steady state circulating currents. Virtual impedance in addition to droop control can be used for this purpose [34] [35]. Due to its good power sharing results and the applicability for a decentralized control approach [36], this combination is also the preferred method in this work. The next sections will give detailed explanations of these methods and their control techniques.

## 3.2 Hierarchical Control Structure

In islanded microgrids, which mainly consist of paralleled DG units and loads, the main control tasks include maintaining stable voltage and frequency, in addition to power flow control. Stability challenges tend to be more challenging in an islanded microgrid than in a grid-connected micro-

grid, due to no stiff, stabilizing grid [37]. Several approaches can be used for controlling the microgrid, where a hierarchical control structure is chosen in this work.

As presented in [38], a hierarchical control structure can be divided into four different levels, numbered from zero to three. The control speed decreases with increasing level, where the level zero has the fastest control loop [6]. A representation of the different control levels is illustrated in Fig. 3.3, which shows that the higher levels of control are dependent on the lower.

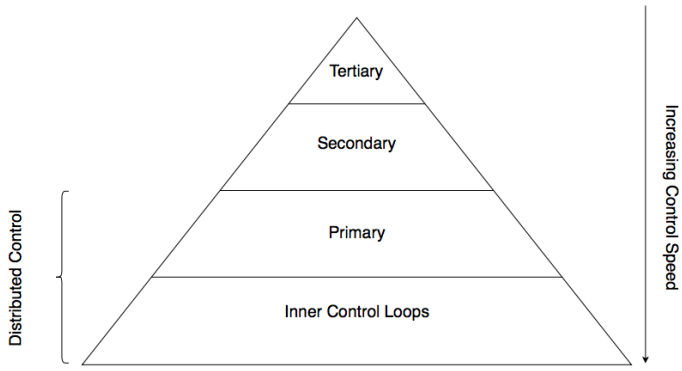


**Figure 3.3:** Hierarchircal control structure

The inner control loops are at level zero, which include the local control for each device. This control level includes the inverter's current and voltage control which are necessary to keep the system stable. Level one, the primary control, focuses on the microgrid as a whole, and makes sure the interaction between paralleled inverters is sufficient. Droop control and the use of virtual impedance operate on this level of control.

The secondary and tertiary control represent the two uppermost levels. The secondary control secures that the electrical levels are within certain limits. It can also make sure that the microgrid is synchronized with the

main grid. Tertiary control is present in case of a grid-connected microgrid. This level controls the exchange of energy between the main grid and the microgrid.

The various control levels can be utilized differently. The mechanisms can be based on a centralized control, a master slave control, or a decentralized control [39]. In this thesis, a decentralized control is chosen on the background of having an easily expandable system with plug-and-play capability. Decentralized control can be utilized through a controller with or without communication, where this thesis is focused on a communication-less controller in the primary control. This choice is motivated by the same arguments as for choosing the decentralized approach. In addition to these arguments, motivations for this approach are that a communication-less controller will be more reliable in case of downtime and to avoid the costly alternative of long distance communication lines [9, chapter 3].

In the following, this chapter will provide detailed explanations of the control systems, which aim for sufficient power sharing in the islanded microgrid.

## 3.3 Inner control

The inner control is responsible for the voltage and current levels at the output of the inverters. For each inverter, the current through the inverter-side inductor and the voltage across the capacitor in the LCL-filter are controlled. This is done through a cascaded control structure, by using the synchronous reference frame [40]. The control structure is shown in Fig. 3.4. The synchronous reference frame gives stationary quantities in a balanced system. Since PI-controllers provide zero steady-state error with such quantities, they are chosen for the controllers [41, chapter 9]. A description of the synchronous reference frame is given in App. A.

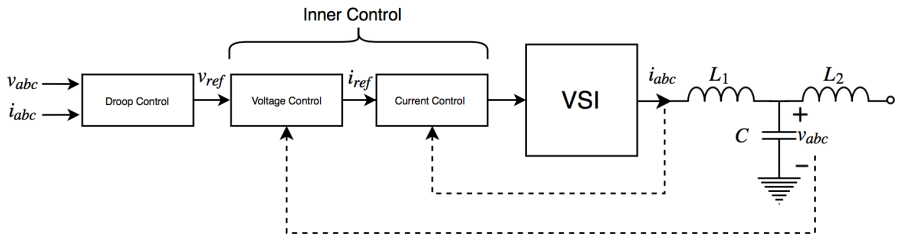


**Figure 3.4:** The cascaded control loop

Since an islanded mode of operation is considered, the voltage level is completely controlled by the inverters in the microgrid. In this mode of operation, the voltage control is the main objective of the inner control loops. In the next sections, the structure of these control loops will be presented.

### 3.3.1 Vector Control

The control system is based on the synchronous reference frame, where a vector control principle is used to achieve accurate voltage and current control. By having the d-axis aligned with the reference voltage vector [42, chapter 5] and using a per-unit representation, the reference voltage vector's d-axis component is equal to the per-unit voltage level. Since the q-axis is 90 °shifted from the reference voltage vector, its q-axis component is equal to zero. The assumption of a balanced three-phase system makes the 0-component always equal to zero. Therefore the 0-component is omitted in this thesis.

### 3.3.2 Current Controller

The current controller is the innermost control loop and has the fastest dynamics. It is designed to control the current flowing in the inductor $L_1$ in the LCL-filter, as shown in Fig 3.5.

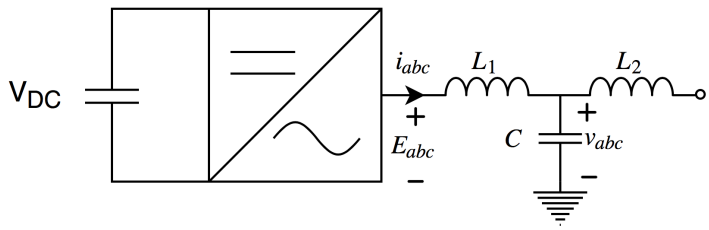


**Figure 3.5:** Three-phase inverter

By applying Kirchoff's voltage law on the system in this figure, (3.3) can be found.

$$E_{abc} = R \cdot i_{abc} + L_1 \frac{di_{abc}}{dt} + v_{abc} \tag{3.3}$$

where $E_{abc}$ is the voltage level before the LCL-filter, while $v_{abc}$ is the voltage after the filter. The current through the inverter-side inductor is denoted as $i_{abc}$, while $R$ is the resistor of the grid-side inductor, $L_1$.

In the synchronous reference frame, the dynamics can be presented as in (3.4), where the superscripts denote if it is the d- or q-axis component.

$$L_1 \cdot \frac{d}{dt}\begin{bmatrix} i^d \\ i^q \end{bmatrix} = \begin{bmatrix} E^d \\ E^q \end{bmatrix} - \begin{bmatrix} v^d \\ v^q \end{bmatrix} - R\begin{bmatrix} i^d \\ i^q \end{bmatrix} + \begin{bmatrix} 0 & \omega L_1 \\ -\omega L_1 & 0 \end{bmatrix}\begin{bmatrix} i^d \\ i^q \end{bmatrix} \tag{3.4}$$

Since a balanced system is assumed, only the d- and q-axis components of the synchronous reference frame are considered.

Accurate current responses are secured by designing the current controller based on these equations. The last term in (3.4) represents cross-coupling effects between the d- and q-axis components. To be able to control these axis components independently from each other, the last term in (3.4) is cancelled through decoupling terms. This is shown in the control system, which is presented in Fig. 3.6. The time delay related to the switching in the VSI is given by (3.5) [43, chapter 3]. Since average model inverters are used in the simulations, this time delay, $T_d$, is based on an assumed switching frequency, denoted $f_{sw}$.

$$T_d = \frac{1}{2 \cdot f_{sw}} \tag{3.5}$$

In addition to the decoupling terms, the controller contains feed-forward terms of the voltage level, presented in the same figure. This makes the control system independent of the voltage level. The decoupling- and feed-forward terms ease the tuning of the PI-controller since the proportional and integrator gain then can be selected independently of the voltage level and cross-coupling effects.

To avoid interference with noise related to the switching frequency [44, chapter 8], the natural frequency of the closed current loop is selected based on (3.6). This is used to select the parameters of the PI-controllers.

$$\omega_{0,i} = \frac{w_{sw}}{10} = \frac{2\pi f_{sw}}{10} \tag{3.6}$$

### 3.3.3 Voltage Control

The design of the voltage control loop is done through a similar approach as for the current controller. It is however designed to control the voltage across the capacitor in the LCL-filter, instead of the current flowing in the inverter-side inductor in the filter. The voltage controller is developed by

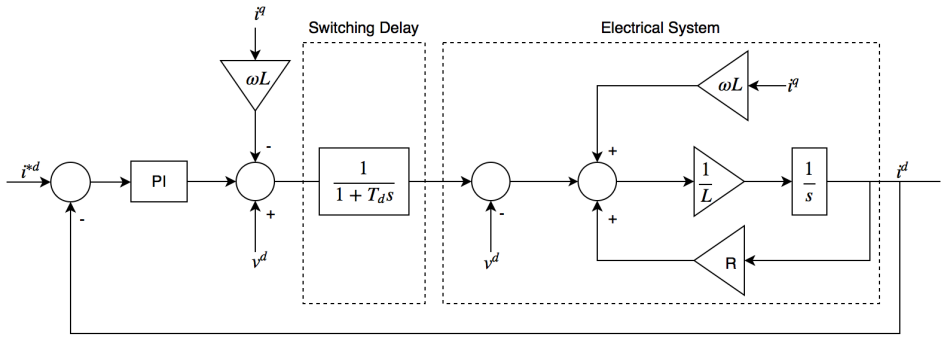


(a) d-axis

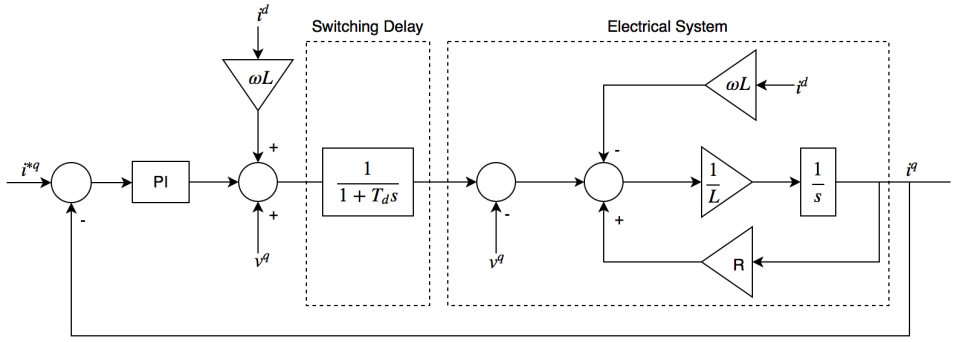


(b) q-axis

**Figure 3.6:** Block diagrams showing the current controller

assuming that the current control loop is much faster than the voltage controller. Under this assumption, the current control loop can be represented as unity seen from the voltage control level. The delays related to the current control are neglected, as they are assumed to be much smaller than the delays from the voltage controller. By applying Kirchoff's current law on the system in Fig. 3.5, the dynamics of the voltage can be found, as shown in (3.7).

$$i - i_L = C\frac{dv_c}{dt} \tag{3.7}$$

This equation can be transformed into the synchronous reference frame to get the equation shown in (3.8).

$$C \cdot \frac{d}{dt}\begin{bmatrix} v^d \\ v^q \end{bmatrix} = \begin{bmatrix} i^d \\ i^q \end{bmatrix} - \begin{bmatrix} i_L^d \\ i_L^q \end{bmatrix} + \begin{bmatrix} 0 & \omega C \\ -\omega C & 0 \end{bmatrix} \begin{bmatrix} v^d \\ v^q \end{bmatrix} \tag{3.8}$$

In this equation, $i^d$ and $i^q$ are the d- and q-axis components of the current flowing through the inverter-side inductor, which is represented by $L_1$. $v^d$ and $v^q$ are the d- and q-axis components of the voltage across the capacitor in the LCL-filter. The internal resistor of the grid-side inductor is denoted by $R$, while $\omega$ is the system's frequency.

By using the same approach that was shown for the current controller, the voltage controller contains decoupling and feed-forward terms to cancel the cross-coupling and load current dependency. The voltage controller is shown in Fig. 3.7.

To secure sufficient difference in the current and voltage controllers' bandwidths, the natural frequency of the closed voltage loop is selected based on (3.9).

$$\omega_{0,v} = \frac{\omega_{0,i}}{10} = \frac{2\pi f_{sw}}{100} \tag{3.9}$$

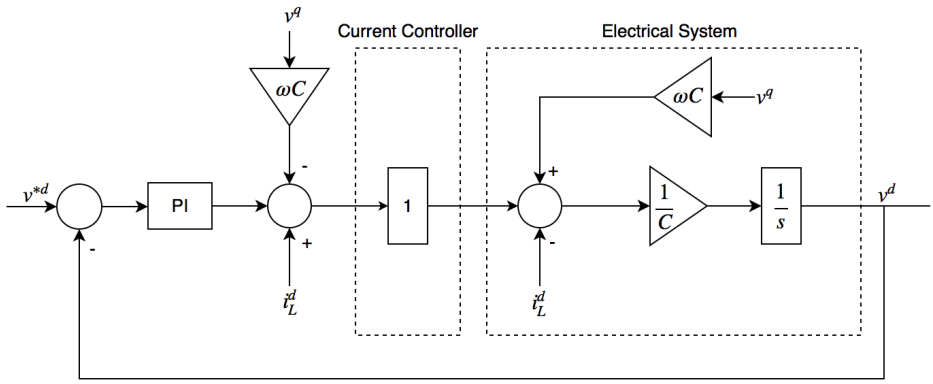


(a) d-axis

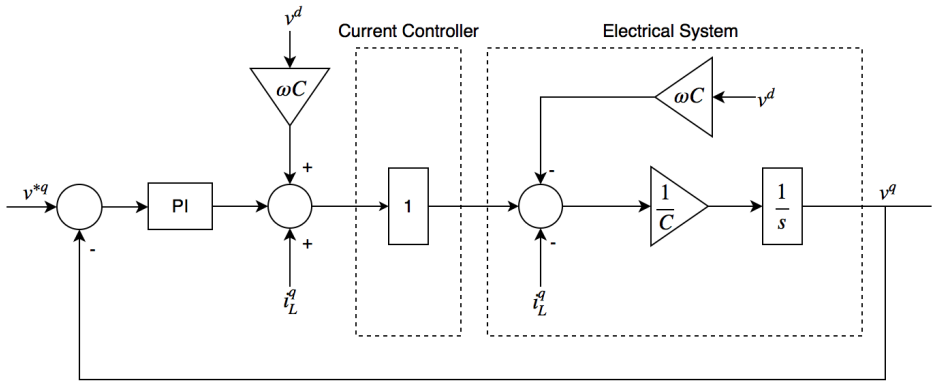


(b) q-axis

**Figure 3.7:** Block diagrams showing the voltage controller

### 3.3.4 PI-Controllers

The implementation of current and voltage controllers is done through a classical setup with a PI-controller in series with the electrical system. A feedback of the relevant quantity is given, as shown in Fig. 3.8. In order to obtain a fast and accurate response, the proportional- and integrator gain of

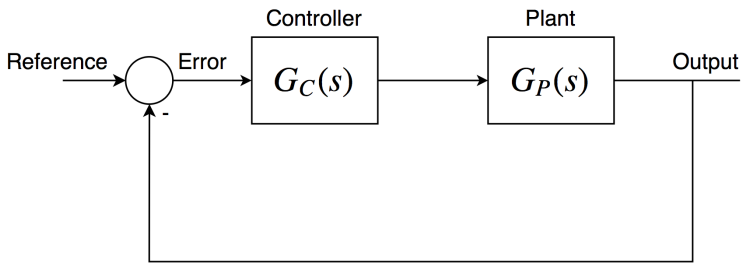


**Figure 3.8:** General block diagram for the approach for the inner controllers

the PI-controller have to be selected carefully.

In the selection of these parameters, a pole placement method is utilized. This entails an approximation of the physical process, expressing the process by the dominant pole only. Consequently, the decoupling terms explained for the voltage- and current controllers are assumed to ideally compensate for the cross-coupling effects. Delays related to switching are neglected in the current controller, while the inner current loop is represented as unity when designing the voltage controller. The electrical systems can then be presented as the transfer function shown in (3.10), where the constants $c_1$ and $c_2$ are defined based on the specific system [45].

$$G_{dominant} = \frac{c_1}{s + c_2} \tag{3.10}$$

The tuning of the PI-controllers is decided based on the characteristic polynomial in the denominator of the closed-loop transfer function, given by (3.11) [41, chapter 4]. The closed loop transfer function is presented in (3.12), where $K_p$ and $K_i$ are the parameters of the relevant PI-controller. These parameters are equal for the controller on the d- and q-axis.

$$P(s) = s^2 + 2\xi\omega_0 s + \omega_0^2 \tag{3.11}$$

$$G_{cl} = \frac{K_i \cdot c_1 + K_p \cdot c_1 s}{s^2 + (c_2 + K_p \cdot c_1)s + K_i \cdot c_1} \tag{3.12}$$

By combining (3.11) and (3.12), the parameters of the PI-controller can be decided by (3.13) and (3.14).

$$K_p = \frac{2\xi\omega_0 - c_2}{c_1} \tag{3.13}$$

$$K_i = \frac{\omega_0^2}{c_1} \tag{3.14}$$

The damping coefficient, $\xi$, is chosen to 0.7 both for the voltage and current controller, in order to achieve well damped oscillations and relative low overshoot [41, chapter 4]. The natural frequency, $\omega_0$, can then be decided for each controller to get the desired response.

The tuning of the PI-controllers used in the current- and voltage control loops is shown in App. E, and bode plots showing the stability margins are shown in App. F. The MATLAB-code for making these plots are given in App. G.

## 3.4 Primary Control

The primary control level takes care of the interaction between inverters in the islanded microgrid considered in this thesis. This is done through control of the voltage and frequency levels. With a distributed and communication-less control approach, the primary control is based on measurements performed locally at the inverters. The use of droop control methods is examined. This section presents the algorithms utilized, including in-depth explanations about the use of virtual impedance for power sharing purposes.

### 3.4.1 Droop Control

Droop control algorithms seem promising in order to accommodate the aforementioned objectives for the microgrid under investigation [36], and are therefore chosen to be used in the primary control loop. Through the study of different cases for the microgrid, two different methods are utilized: The conventional and the opposite droop control. These will be presented in this section.

Without a need for communication between inverters, droop control takes advantage of the relation between the voltage and the frequency in the grid, and the power supplied by the inverters [46, chapter 9] [39]. The frequency and voltage levels communicate if there is under- or overproduction in the microgrid, which is used to adjust the power supplied by the inverters. This is done through a higher level of control, by adjusting the set points for active and reactive power.

The droop control is located at the inverters, where the operation of each unit will adapt to the entire system. Because of this, the control strategy is well suited for expansions in the grid. Since the utilization of droop control does not require high-speed communication, this may lead to significant reductions in costs compared to a centralized controller [9, chapter 3], in addition to high reliability.

To explain the concept of droop control, a power flow through the line in Fig. 3.9 is studied. With an output impedance represented by Z, the active and reactive power flow in the line is given by (3.15) and (3.16) [39] [47].

$$P = \frac{U_1^2}{Z} cos(\Theta) - \frac{U_1 U_2}{Z} cos(\Theta + \delta) \tag{3.15}$$

$$Q = \frac{U_1^2}{Z} sin(\Theta) - \frac{U_1 U_2}{Z} sin(\Theta + \delta) \tag{3.16}$$

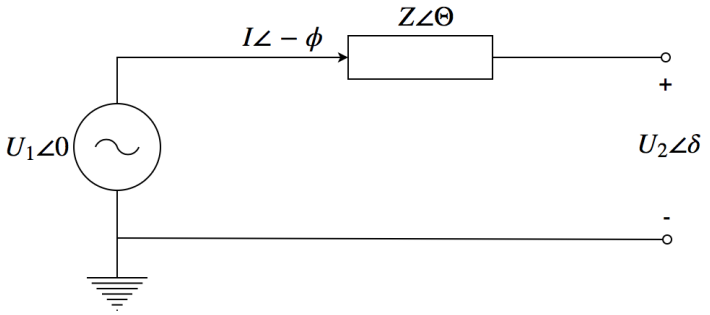


**Figure 3.9:** A representation of power flow through a distribution line

$\delta$ represents the power angle, while $\Theta$ is the angle of the output impedance, Z. $U_1$ and $U_2$ are the voltage levels at the respective locations shown in Fig. 3.9. In a low-voltage microgrid, the output impedance is often dominated by a resistive component.

All components located between the inverter's output and the load are a part of the inverter's output impedance [48]. Even if the line has a resistive behavior, these components, such as transformers and filters, will also contribute to the output impedance. In the microgrid considered in this work, LCL-filters are located at the output of the inverters, and the grid-side inductor will contribute to the output impedance, making it more inductive [36].

In the following, inverters with a dominating inductive output impedance will be considered, leading to the conventional droop control method. In addition, the opposite droop control method will be derived, which is based on an output impedance dominated by a resistive component. Both methods are derived based on (3.15) and (3.16).

### Conventional Droop Control

Even if most low-voltage microgrids have line impedances dominated by a resistive term, components such as transformers and LCL-filters can contribute to a more inductive behavior. In the case of small line impedances, the output impedance can become predominantly inductive.

With inductive output impedances, the conventional droop control method can be used to control the power sharing. In the derivation of this method, (3.15) and (3.16) form the basis, in addition to two important assumptions:

*The output impedance is purely inductive.* This makes the impedance in (3.15) and (3.16), $Z$, equal to a pure reactance, $X$. The impedance angle, $\Theta$, will then be equal to 90°.

*The power angle, $\delta$, is assumed to be small.* This assumption is done on the background of a relatively small phase difference between the voltage at the output of the inverter and at the loads' connection point. By this, $sin(\delta) \simeq \delta$ and $cos(\delta) \simeq 1$ can be used in the derivations.

Applying the simplifications in (3.15) and (3.16), results in an expression for $\delta$, as shown in (3.17). The voltage drop across the output impedance can be expressed by (3.18) [39] [49].

$$\delta \simeq \frac{XP}{U_1 U_2} \tag{3.17}$$

$$U_1 - U_2 \simeq \frac{XQ}{U_1} \tag{3.18}$$

(3.17) and (3.18) show that the power angle, $\delta$, which is directly related to the frequency [50, chapter 4.3.3], is dependent on the active power. The voltage drop, $U_1 - U_2$, on the other hand, is related to the reactive power. This is the basis for the conventional droop characteristic, as represented in (3.19) and (3.20) [6].

$$\omega - \omega_{ref} = m_P(P_{ref} - P) \tag{3.19}$$

$$E - E_{ref} = n_Q(Q_{ref} - Q) \tag{3.20}$$

This characteristic is based on a rated voltage and frequency, denoted $E_{ref}$ and $\omega_{ref}$. The active and reactive droop coefficients are given as $m_P$ and $n_Q$. They decide the relation between frequency and active power, and voltage and reactive power, respectively. E, $\omega$, P and Q are the measured values of voltage, frequency, active power and reactive power. $P_{ref}$ and $Q_{ref}$ are the set points for active and reactive power [39]. These are determined by a higher level of control, which normally is dependent on communication in order to adapt to the load of the system [51]. These upper levels of control are beyond scope of this thesis. The conventional droop characteristic is summarized in Fig. 3.10 [6]. In this figure, the loaded active- and reactive power are denoted along the x-axes. As shown, an increased active load leads to a reduction in the frequency, while the output voltage is reduced if more reactive load is added to the system.

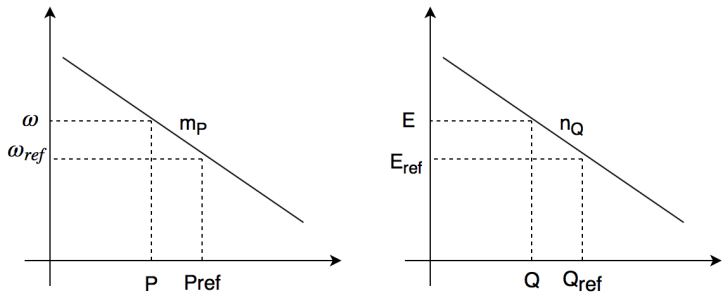


**Figure 3.10:** The characteristic of the conventional droop control

This characteristic can be utilized in the conventional droop control method, where the active power fed into the line is controlled based on fre-

quency deviations, while deviations in voltage control the reactive power supply [52] [39]. The deviations are determined by the droop coefficients, which are given based on (3.21) and (3.22) [36].

$$m_P = \frac{\Delta\omega_{max}}{P_{change}} \tag{3.21}$$

$$n_Q = \frac{\Delta E_{max}}{Q_{change}} \tag{3.22}$$

$\Delta\omega_{max}$ is the maximum allowed frequency deviation due to a load change in active power, $P_{change}$. The maximum allowed voltage change, $\Delta E_{max}$, is in a similar way related to a load change in reactive power, $Q_{change}$. Often, $\Delta\omega_{max}$ and $\Delta E_{max}$ are decided based on the maximum deviations allowed in the grid [36]. The droop coefficients also affect the power sharing among inverters, where larger droop coefficients lead to better power sharing. However, the coefficients have upper limits, where increasing them would lead to instability in the system [53]. Within the stability limits, the choice of droop coefficients is a trade-off between the power sharing performance and the deviations in voltage and frequency. The relation between the droop coefficients of different inverters will be equal to the relation between the power supplied from the same inverters in an ideal microgrid. In order to make two DG units share the power equally, the droop coefficients should, therefore, be designed equally in size.

With close to purely inductive output impedances, the conventional droop control method is an effective way to adjust frequency and voltage relative to the supplied power. While the active power is shared equally among inverters, this method has certain challenges related to reactive power sharing. A difference in output voltage or output impedances, which can occur with distribution lines of different lengths, often causes unequal reactive power supply from the inverters [36] [54]. As a result, reactive cir-

culating currents are generated. This is one of the challenges to be further investigated in this thesis, including a study of how virtual impedance can be utilized to minimize these circulating currents.

A real distribution line will always contain a combination of resistive and inductive components. However, purely inductive distribution lines can cause an unstable response, as discussed in [9, chapter 3]. This enhances the importance of choosing realistic values for the output impedances, including a combination of resistance and reactance. It also has to be taken into consideration when deciding the virtual impedance values, which will be further discussed later in this thesis.

In the case studies presented in Chapter 4, the implementation of a conventional droop controller is as shown in Fig. 3.11. The basis of the controller is the conventional droop characteristic, given by (3.19) and (3.20). The droop coefficients, $m_P$ and $n_Q$, are selected based on (3.21) and (3.22). In case of a load change equal to half a residential load, the frequency and voltage deviations are selected to be 0.1 Hz and 2.3 V, respectively.

Figure 3.11 shows that only the d-axis component of the voltage, $v^d$, is related to the droop characteristic, while the q-axis component, $v^q$, is forced to be zero. The output frequency obtained from the droop controller is integrated, which gives a constantly changing angle, $\omega t$. This angle is used in the transformation between the abc- and the synchronous reference frame. By utilizing this approach, the voltage vectors at the output of the inverters are aligned with the d-axis in the synchronous reference frame. For a review of the synchronous reference frame, see App. A.

As shown in Fig. 3.11, the measured active and reactive power are filtered through low-pass filters. This makes the droop controller less affected by high frequency components in the system, and contributes to a sufficient difference in bandwidth between the inner control loops and the droop controller [55]. However, a low cutoff-frequency will make the droop

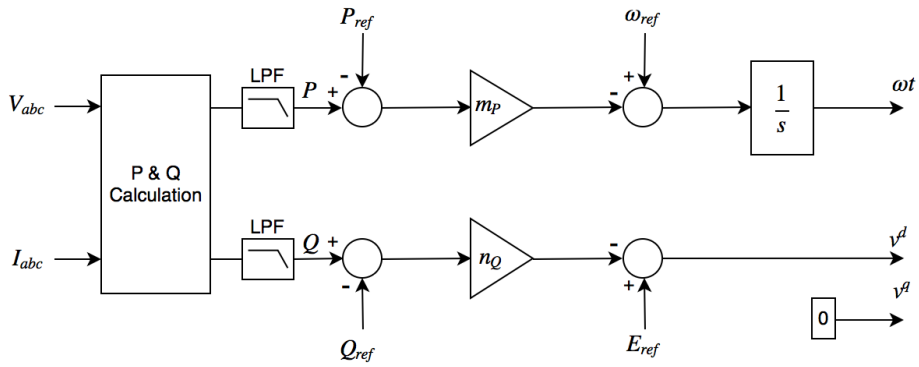


**Figure 3.11:** Implementation of the conventional droop control method

controller have a slow performance, which degrades the power sharing performance. In this thesis, the cutoff-frequency of the low-pass filters are selected by an iterative process, but with a value close to the one in [55]. All the parameters used in the droop controllers are given in App. D.

### Opposite Droop Control

Since low-voltage microgrids often have output impedances dominated by resistive components, a droop characteristic that is based on an assumption of purely resistive output impedances can also be used [52]. This is often referred to as the opposite droop control method, which can be explained based on (3.15) and (3.16). This is done through the same procedure as for the conventional droop control method, but with a different set of assumptions:

*The output impedance is purely resistive.* The output impedance, Z, is denoted R, having an impedance angle, $\Theta$, equal to 0.

*The power angle, $\delta$, is assumed to be small.* As in the case of conventional droop control, this leads to $sin(\delta) \simeq \delta$ and $cos(\delta) \simeq 1$.

By using (3.15) and (3.16) together with these assumptions, expressions for $\delta$ and the voltage drop can be derived, shown in (3.23) and (3.24).

$$\delta \simeq -\frac{RQ}{U_1 U_2} \tag{3.23}$$

$$U_1 - U_2 \simeq \frac{RP}{U_1} \tag{3.24}$$

Compared to the conventional droop characteristic, (3.23) and (3.24) show opposite relations: The power angle, $\delta$, and hence the frequency, are dependent on the reactive power, while the voltage drop depends on the active power [39] [56]. This is the basis of the opposite droop control, with characteristic given by (3.25) and (3.26) [52].

$$\omega - \omega_{ref} = m_Q(Q - Q_{ref}) \tag{3.25}$$

$$E - E_{ref} = n_P(P_{ref} - P) \tag{3.26}$$

The droop coefficients are denoted $n_P$ and $m_Q$, and are shown graphically in Fig. 3.12.

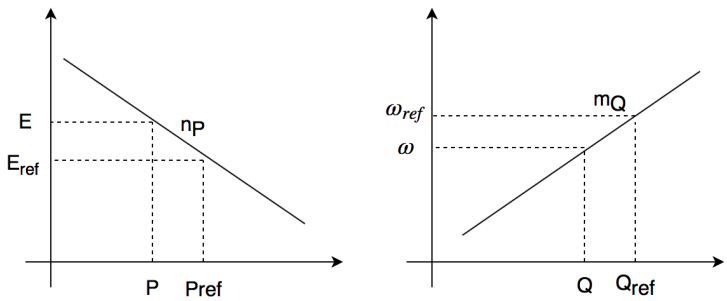


**Figure 3.12:** The characteristic of the opposite droop control

As for the conventional droop control, the droop coefficients are chosen based on active and reactive power change, and maximum deviations in voltage and frequency related to these changes. The design is then given

as shown in (3.27) and (3.28). The coefficients can, in the same way as for the conventional droop control, be used to control the power sharing among inverters.

$$m_Q = \frac{\Delta\omega_{max}}{Q_{change}} \tag{3.27}$$

$$n_P = \frac{\Delta E_{max}}{P_{change}} \tag{3.28}$$

The opposite droop characteristic has a direct relation between the voltage drop across the output impedance and the active power flow. Because of this, two inverters with mismatching output impedance will induce active circulating currents. This is analogous to the conventional droop control's power sharing, but the circulating currents are related to the active power flow instead of the reactive. The opposite droop control has advantages compared to the conventional droop control when it comes to direct voltage control [52] and harmonic power sharing [56]. The overall system is more damped, and phase errors will hardly affect the active power sharing [56]. Because of the above-mentioned advantages, the opposite droop control algorithm may be preferred over the conventional droop control in some cases. However, the conventional droop control is more commonly used, for instance because of better active power sharing [9, chapter 3].

In the modelling that will be presented in Chapter 4, the opposite droop control is implemented as shown in Fig. 3.13. The control is similar to the conventional droop control, with the voltage vector aligned with the synchronous reference frame, and based on the relations given in (3.25) and (3.26). As for the conventional droop control, low-pass filters are used to filter the measured output power. Both the low-pass filters and the criteria used to design the droop coefficients are the same, and is given in App. D.

Mismatching output voltages and physical output impedances are ele-

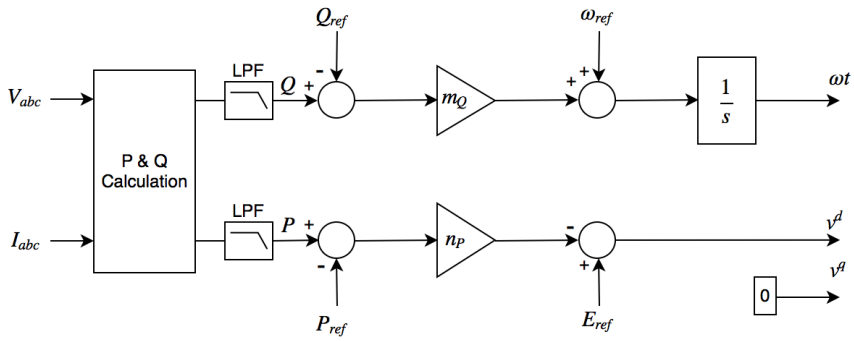


**Figure 3.13:** Implementation of the opposite droop control method

ments that affect the power sharing when using droop control algorithms, where another is the angle of the physical output impedance. Challenges related to this are presented in the following section.

### 3.4.2 Mixed Output Impedance

When using local measurements for voltage and frequency, it is convenient to utilize the mentioned droop control algorithms for a decentralized control approach. When it comes to power sharing, the challenges related to differences in output impedances have already been mentioned. The characteristics of the conventional and opposite droops are based on assumptions of either a purely inductive or purely resistive output impedance. In a real microgrid, the output impedance exists of both resistance and reactance, as described in Section 2.4. This results in a coupling between active and reactive power, making both of them depending on voltage and frequency levels [57]. More complicated power sharing challenges are then present, with many proposed solutions reviewed in [57].

Since the conventional droop control is based on the assumption of purely inductive output impedances, several issues arise when the control method is applied in systems with resistive or mixed output impedances.

The conventional droop control used in a system with predominantly resistive output impedances can provide a stable and well functional performance, as discussed in [54]. However, the stability margins are smaller, and the challenges related to reactive power sharing often increase when having predominantly resistive output impedances while using the conventional droop control [54]. If the control parameters are not selected carefully, stability issues often arise, especially when having local loads and large output impedances [58] [59]. The active power has a minor effect on the stability challenges, while the reactive droop coefficient $n_Q$ and the output resistance is of great importance. According to [58], the use of conventional droop control in a predominantly resistive microgrid provides bad transient behavior for the power control in grid-connected mode. In island mode, the challenges are even more complicated, causing worse reactive power sharing and increased stability issues.

Also when applying the opposite droop control to a predominantly inductive output impedance, issues related to stability appear. The opposite droop control is rarely used in microgrids with predominantly inductive output impedances, because of these stability challenges and the importance of accurate active power dispatch. The conventional droop control's similar behavior and compatibility with synchronous generators are often preferable [52], in addition to the accurate active power sharing. By selecting the droop coefficients carefully, the conventional droop control can provide virtual inertia to the system [60]. However, there are cases where the opposite droop control's direct voltage control is preferable, in addition to the more stable operation with predominantly resistive output impedances [52] [54].

Even if the droop control algorithms provide unstable responses with certain output impedances, the use of virtual impedances is an effective method to modify the output impedance of the inverters. It can effec-

tively achieve stable, well performing responses, almost regardless of the actual output impedance of the inverters [61]. In the following sections, power sharing issues will be further investigated through the use of virtual impedances as a part of the inverters' control system. The output impedance of an inverter will be denoted by physical output impedance, in order to avoid confusion when the concept of virtual impedance is introduced. The combination of physical output impedance and virtual impedance is denoted by equivalent output impedance.

### 3.4.3 Virtual Impedance

The previous sections have explained concepts and challenges related to power sharing in islanded microgrids. This section will elaborate on techniques used to improve the power sharing. Virtual impedance is a control mechanism which is frequently used for this purpose, often in combination with droop control [36] [62]. This is also the focus of this thesis. An introduction to virtual impedances, including different areas of utilization will be given in this section. Design considerations, both for existing methods and proposed virtual impedance methods will be presented. The implementation of the virtual impedances used in the simulation models is explained.

In addition to power sharing, virtual impedances are used in converter control for applications such as harmonic voltage compensation and increased stability [63]. The concept is divided into two categories in [63]: Inner- and outer virtual impedance. Inner virtual impedance-loops are used for harmonic compensations and current limiting purposes, and the signal from the loop is applied at the PWM. Harmonic voltage compensation, control of power flow, mitigation of unbalanced voltage and sharing between nonlinear loads in a power system are done by the use of outer virtual impedance, which modifies the reference signal of the controller.

The two categories of virtual impedances are both used to shape the

equivalent output impedance of the converter. Because of its many applications, the value of this impedance has to be decided based on its purpose. In [64], the values of the virtual impedances are studied in order to optimize the microgrid's performance. The virtual impedances can help to keep the voltage within certain limits, have sufficient reactive power sharing, provide system damping and decouple the active and reactive power. In general, a virtual impedance imitates the behaviour of an actual impedance, without experiencing losses. The non-physical concept of negative impedance can also be added to the inverters thorugh the use of virtual impedance [63].

Since this work is focused on the challenges related to power sharing of fundamental components, the microgrid system presented in Chapter 2 will be used for the investigation of the use of virtual impedance in microgrid. The utilization of outer virtual impedance loops is studied in order to improve power sharing between linear loads. First, an elaboration on outer virtual impedance techniques will be performed. In the following, outer virtual impedance is simply denoted virtual impedance.

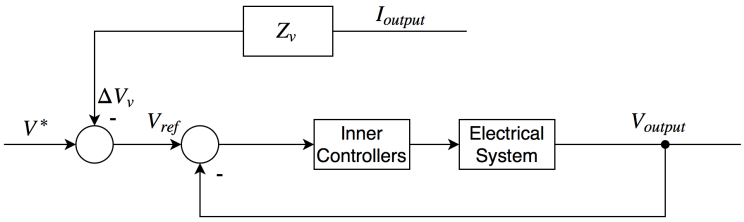


**Figure 3.14:** Block diagram showing an outer virtual impedance loop

A diagram showing the general design for virtual impedance loops is shown in Fig. 3.14 [62]. The voltage reference is modified by the output current, $I_{output}$, and the virtual impedance, denoted by $Z_v$. As shown in the figure, the voltage reference from the droop control, $V^*$, is subtracted a voltage drop caused by the virtual impedance, $\Delta V_v$, which gives the reference

to the inner control loops, $V_{ref}$. This approach can both change the magnitude and the impedance angle of the equivalent output impedance. The selection of the virtual impedances have to be done carefully, both when it comes to the relation between the resistive and reactive components, but also regarding the impedances' total size.

A distinct disadvantage of applying virtual impedances is their tendency of reducing the voltage reference, as is evident from (3.29). This has to be taken into consideration when the value of the impedance is selected. By applying a combination of positive and negative virtual impedances, this thesis will suggest virtual impedance designs that limit the negative effects on the voltage. A thorough review of advantages and disadvantages regarding virtual impedance in combination with droop control is given in [36].

$$V_{ref} = V^* - \Delta v_v = V^* - Z_v \cdot I_{output} \tag{3.29}$$

In (3.29), $V^*$ denotes the voltage reference from the droop controller, while $\Delta v_v$ is the voltage drop due to the virtual impedance. $I_{output}$ is the output current and $Z_v$ the virtual impedance. $V_{ref}$ is the voltage reference applied to the inner control.

### Existing Designs

As mentioned above, virtual impedances are commonly used in combination with droop control algorithms in order to improve active and reactive power sharing. The virtual impedances can be used to compensate for possible differences in physical output impedance among inverters. According to literature, this method is effective both in terms of active and reactive power sharing [65], because the two inverters get equal equivalent output impedance. The virtual impedance is then selected to make the equiva-

lent output impedance, including the physical output impedance and virtual impedance, be equal for all inverters in the system. The basic method can be explained by (3.30), and is referred to as output impedance matching [65]. $Z_{o,i}$ denotes the output impedance of inverter *i*, which is the sum of all impedances between the inverters' output and the load, as seen from the inverter. The virtual impedance applied to inverter *i* is referred to as $Z_{v,i}$.

$$Z_{o,1} + Z_{v,1} = Z_{o,2} + Z_{v,2} \tag{3.30}$$

Virtual impedance can also be used with the primary goal of changing the impedance angle of the equivalent output impedance. When utilizing the conventional droop control, positive inductive- or negative resistive virtual impedances can be added to low-voltage grids in order to provide inductive equivalent output impedance for the inverters [47] [66] [67]. In addition, this may contribute to increasing the stability margins [54]. The method takes advantage of the conventional droop control's accurate active power sharing. This method is often preferred rather than the opposite droop when the physical output impedances are dominated by predominantly resistive line impedances [9, chapter 3].

A similar method can be utilized for the opposite droop control method, but instead of a virtual inductor, the virtual impedance applied has a relatively large resistive value [68] [56]. When virtual impedances are used to make the equivalent output impedances have a more inductive or resistive behavior, the size of the virtual impedances is normally selected to dominate the physical output impedances [56] [9, chapter 3] [27]. This ensures proper decoupling of the active and reactive power. In case of unequal physical output impedances of the inverters, the relative difference between the equivalent output impedance is reduced, which has a positive effect on the power sharing [56]. In addition to improving the power sharing, the resistive virtual impedances contribute to an increased damping of

the system [68].

### Proposed Designs

With existing virtual impedance designs, power sharing is significantly improved. However, the voltage drops related to these designs can be relatively large [69]. This section will, therefore, propose virtual impedance designs that are able to reduce the voltage drops.

The first proposed solution suggests a new virtual impedance design in order to utilize output impedance matching, where one virtual impedance is divided into two. In the approach taken in [9, chapter 3], a virtual impedance is added to the inverter with the lower physical output impedance, in order to make the equivalent output impedance of the two inverters equal. If virtual impedances are added to both inverters, the voltage drop over the virtual impedances can be heavily reduced. The proposed solution for matching the output impedances includes a negative virtual impedance at the inverter with the higher physical output impedance and a positive virtual impedance added to the inverter with the lower physical output impedance. Each virtual impedance is consequently half the value of the virtual impedance that would be applied if using the existing design approach, with one virtual impedance only. Thus, the voltage drop due to the use of virtual impedances will be significantly reduced by this method.

If virtual impedances are used to obtain predominantly inductive- or resistive equivalent output impedance, the virtual impedances are often selected to be relatively large. Because of their size, the virtual impedances lead to a significant voltage drop. In order to reduce this voltage drop, a solution including a complex virtual impedance are suggested.

When this second proposed solution is applied with the conventional droop control, the virtual impedances include positive virtual inductors and negative virtual resistors. The decoupling of active and reactive power

is by this technique even stronger than by using only inductive virtual impedances. In addition, the voltage drops across the virtual impedances are significantly reduced. The virtual resistor has to be selected smaller in magnitude than the resistive part of the physical output impedance, to avoid the equivalent output impedance to be purely inductive, which can lead to an unstable behavior [9, chapter 3].

A similar approach can be taken when using the opposite droop control, where the virtual impedances will consist of a positive resistor and negative inductor. The negative inductor is suggested equal in magnitude as the largest physical output inductor, since the inductors do not contribute to any stabilizing effect. The resistance is selected to be dominating compared to the larger physical output impedance in the system, as for the more conventionally used virtual impedance method.

In the following, the implementation of the virtual impedances used in the modelling will be presented.

### Implementation

With improved power sharing and limiting circulating currents as the main objectives, this section will elaborate on how the virtual impedance loops used in this work are implemented. The implementation of the virtual impedance loops is done in the synchronous reference frame by using per unit values. This makes the different levels of control compatible with each other since the inner control loops are implemented in this way, as explained in Section 3.3.

The applied virtual impedances are designed as resistive-inductive virtual impedances, where the virtual voltage drop is represented in (3.31).

$$\Delta v_{virtual,abc} = R \cdot i_{abc} + L\frac{di_{abc}}{dt} \tag{3.31}$$

In the implementation of virtual impedances, (3.31) is transformed to the synchronous reference frame by using the park transform. This results in (3.32), which leads to (3.33). Since the system is assumed to be balanced, the 0-component is omitted in the virtual impedance implementation.

$$\Delta v_{virtual,dq0} = Ri_{dq0} + L\frac{di_{dq0}}{dt} + j\omega L i_{dq0} \tag{3.32}$$

$$\begin{bmatrix} \Delta v_{virtual,d} \\ \Delta v_{virtual,q} \end{bmatrix} = R \begin{bmatrix} i_d \\ i_q \end{bmatrix} + L \cdot s \begin{bmatrix} i_d \\ i_q \end{bmatrix} + \begin{bmatrix} 0 & -\omega L \\ \omega L & 0 \end{bmatrix} \begin{bmatrix} i_d \\ i_q \end{bmatrix} \tag{3.33}$$

In order to achieve a voltage level less affected by high-frequency oscillations, low pass-filters are used in the implementation. This is essential when using these virtual impedance loops, due to the derivative term [63] in (3.33). The filters contribute keeping the voltage drops caused by the virtual impedance within reasonable limits, since the derivative terms and high-frequency current components can cause large voltage deviations. Figure 3.15 shows the implementation of virtual impedance used in this work, including the low-pass filters. A disadvantage of using the low-pass filters is that they cause a phase shift that may change the behavior of the virtual impedance [63]. The low-pass filters also cause a slightly slower dynamic response, as they add an additional time delay to the system. The low-pass filters used in the virtual impedance implementation is chosen with a cut-off frequency which equals the frequency of third harmonic oscillations in the system. The exact value is given in App. D.

In the next chapter, simulations verifying the effects of using virtual impedance will be carried out. The proposed virtual impedance methods will be compared to the existing virtual impedance methods covered by the literature review. The power sharing and the output voltage level when

utilizing the different methods will be the primary focus in the analysis.

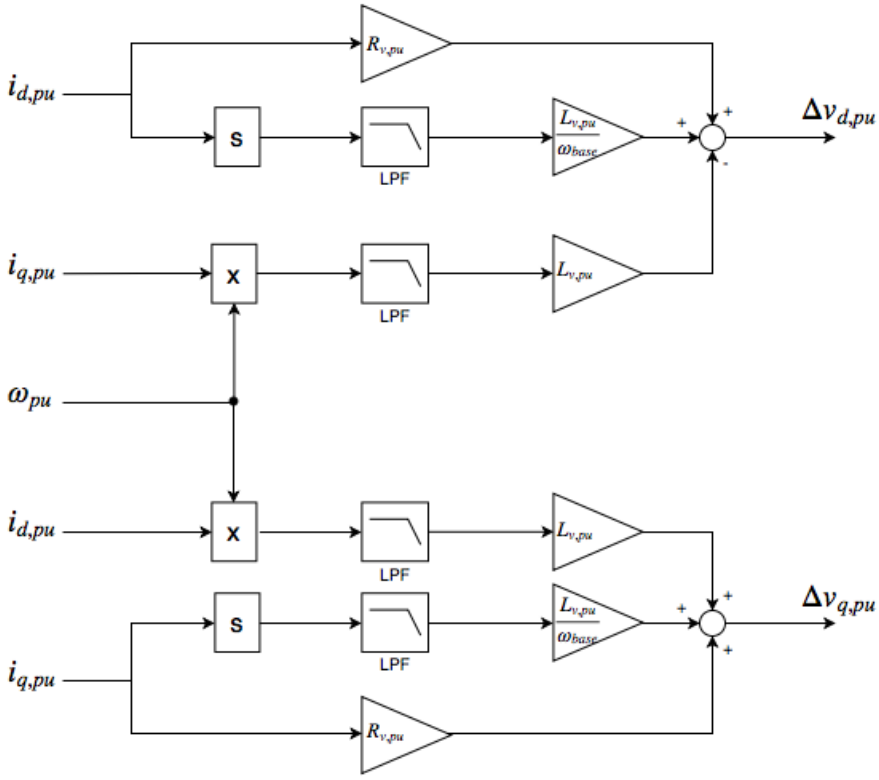


**Figure 3.15:** Schematic of the implementation of virtual impedance

# 4 | Cases Studies

This chapter contains simulations for three different cases, in order to show how virtual impedances can be used to improve power sharing and mitigate circulating currents. Simulations are done for two different microgrid systems, both of which can be presented by the general system presented in Chapter 2. Figures showing the models in Simulink is shown App. I and responses of the different controllers utilized are demonstrated in App. H.

Case 1 presents a microgrid with predominantly resistive physical output impedances, and the results from this case are presented in Section 4.2. This section is divided into two subsections, and includes simulations where both conventional and opposite droop control is utilized in the primary control loop. In case 2, the system has predominantly inductive physical output impedances. The analysis performed is similar as in case 1, with two different subcases for utilizing two different primary control loops. This is presented in Section 4.3. Case 3 is a reproduction of case 2, but in the selection of virtual impedances, the physical output impedance of the inverters is estimated to be 25 % lower than the actual values. This is presented in Section 4.4.

In general, the simulations for each subcase can be divided into three:

1. The conventional- or opposite droop control method is utilized in the primary control loop, without any use of virtual impedance.

2. A commonly used method including virtual impedance is applied to the control system.

3. A proposed virtual impedance method is implemented, which reduce the effect the virtual impedances are having on the voltage.

The first section will introduce general parameters used in the cases, followed by a presentation of the simulation results. The chapter will then be summarized with a discussion of the results.

## 4.1 General Parameters

Since the simulation models are based on the system introduced in Chapter 2, most of the parameters are equal for all the different cases. The parameters are selected based on the mentioned benchmark microgrid [20], in order to secure realistic values for a low-voltage microgrid. Some values are also selected based on the available equipment in the Smart Grid Laboratory at NTNU/SINTEF Energy in Trondheim [70]. The simulations and conclusions drawn in this work can be valuable for future research on the topic, where the Smart Grid Laboratory is likely to be used.

**Table 4.1:** General parameters

| **Parameter** | **Value** |
|---|---|
| Power Rating | 5.7 kVA |
| Nominal Voltage (line-to-line) | 400 V |
| Nominal Frequency | 50 Hz |
| Inverter Side Filter Inductor | 500 $\mu$H |
| Inverter Side Filter Resistance | 0.28 $\Omega$ |
| Grid Side Filter Inductor | 200 $\mu$H |
| Filter Capacitance | 50 $\mu$F |

The general parameters used in the simulations are shown in Tab. 4.1. As described in Chapter 3, there are several control loops related to the

microgrid control. The parameters of the controllers are chosen based on the techniques discussed in the same chapter, and are listed in Tab. 4.2. Appendix D shows quantities used for deciding the control parameters, in addition to other simulation parameters. Base values used for the per-unit system are also shown there.

**Table 4.2:** Control parameters

| **Parameter** | **Symbol** | **Value** |
|---|---|---|
| Proportional Gain PI-Controller in Current Control | $K_{pi}$ | 0.2270 |
| Integral Gain PI-Controller in Current Control | $K_{ii}$ | 1595.2 |
| Proportional Gain PI-Controller in Voltage Control | $K_{pv}$ | 1.8368 |
| Integral Gain PI-Controller in Voltage Control | $K_{iv}$ | 1236.6 |
| P/$\omega$ Droop Coefficient, Conventional Droop | $m_P$ | 2.5937e-4 |
| Q/V Droop Coefficient, Conventional Droop | $n_Q$ | 0.0015 |
| P/V Droop Coefficient, Opposite Droop | $n_P$ | 9.4943e-04 |
| Q/$\omega$ Droop Coefficient, Opposite Droop | $m_Q$ | 4.1851e-04 |

## 4.2 Case 1: Resistive Output Impedance

In low-voltage microgrids without local loads, the physical output impedance of the inverters is often dominated by the line impedances [56]. As discussed in section 2.4, this gives mainly resistive output impedances. The behavior of such a grid will be studied in this section, utilizing different primary control loops. A diagram showing the system investigated in case 1 is depicted in Fig. 4.1. The LCL-filters are omitted in the diagram, while virtual impedances are shown with dotted lines.

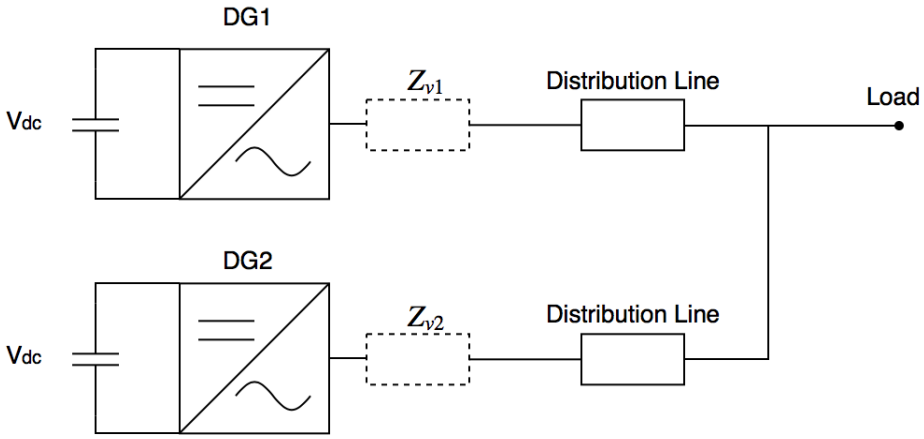


**Figure 4.1:** The investigated system in case 1

In case 1 a), the primary control is implemented by using the opposite droop control method, while in 1 b), the conventional droop control is utilized. Virtual impedances are added to the inverters in both simulations, in order to improve the power sharing performance.

The parameters of predominantly resistive distribution lines are based on the typical line impedance of low-voltage distribution lines, as discussed in Section 2.4. The lengths of the two lines are 500 and 800 meters, which at the nominal frequency have physical output impedances as shown in Tab. 4.3. The distribution lines attached to inverter 1 and 2 are represented by

**Table 4.3:** Physical output impedances for the resistive-dominating microgrid used in case 1

| Parameter | Value |
|---|---|
| $Z_{L1}$ | $0.5136 + j0.0664\Omega$ |
| $Z_{L2}$ | $0.3210 + j0.0415\Omega$ |

the subscript L1 and L2, respectively.

### 4.2.1 Case 1 a): Opposite Droop Control

Since the opposite droop control is designed based on a predominantly resistive output impedance, this method is a natural starting point when investigating the microgrid under study in case 1. The simulation of this system is divided into three time periods, each with a length of two seconds.

- 0-2 seconds: The opposite droop control is implemented without use of virtual impedances.
- 2-4 seconds: A virtual impedance is added to the inverter closest to the load, in order to make the output impedance of the two inverters match each other. This virtual impedance is equal to the difference between the two inverters' physical output impedance.
- 4-6 seconds: Both inverters have virtual impedances implemented in their control systems. The closest inverter has a virtual impedance half of the value used in the previous time slot. The other has a virtual impedance with the same magnitude, but with opposite sign.

The values of the virtual resistance and inductance used in this simulation are listed in Tab. 4.4. The subscript indicates which inverter the virtual resistances and inductances are located at, while the superscript denotes the time period. Time period number 1 is the first time slot where virtual

**Table 4.4:** Virtual resistance and inductance used in case 1 a)

| Parameter | Value |
|---|---|
| $R^1_{v2}$ | 0.1926 Ω |
| $L^1_{v2}$ | 79.26 $\mu H$ |
| $R^2_{v1}$ | -0.0963 Ω |
| $L^2_{v1}$ | -39.63 $\mu H$ |
| $R^2_{v2}$ | 0.0963 Ω |
| $L^2_{v2}$ | 39.63 $\mu H$ |

impedance is used in the simulation, in this case between t = 2 s and t = 4 s. The second time period denotes when the proposed virtual impedance is implemented, here from t = 4 s to t = 6 s. This makes, for instance, $R^2_{v1}$ the virtual resistance added to inverter 1 between t = 4 s and t = 6 s. This notation is also used in the following cases.

The active and reactive power flows from the two inverters are shown in Fig. 4.2. Disregarding the transient periods, this figure shows that the reactive power is shared equally among the two inverters. During start-up and when adding virtual impedance at t = 2 s, transient periods, both with a duration of around 0.5 seconds, occur. The difference in delivered reactive power is however relatively small, also through these periods. When changing from one virtual impedance to the proposed virtual impedance method with two virtual impedances at t = 4 s, there is no noticeable change in the supplied reactive power from the two inverters.

Figure 4.2(a) shows that inverter 2, which is closest to the load, feeds around 56 % of the active power the first two seconds. The remaining 44 % of the active power delivered to the load is fed by inverter 1. When adding a virtual impedance at t = 2 s, the active power sharing is improved, resulting in approximately zero circulating current. The change from a single virtual impedance located at the closest inverter, to the proposed method using two smaller virtual impedances hardly affects the active power sharing. The

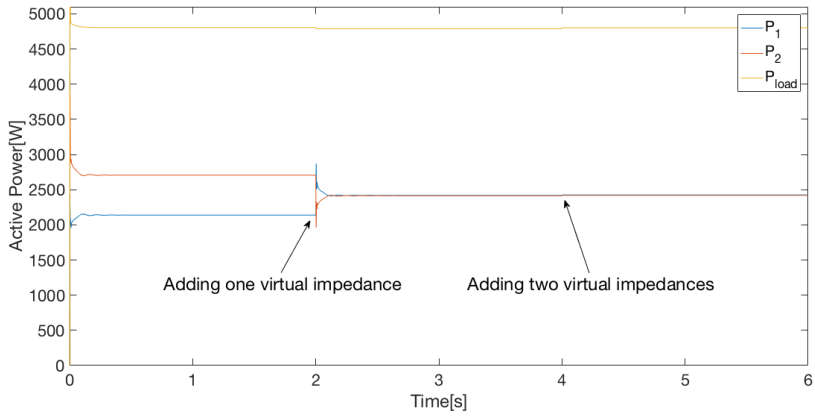


(a) Active Power

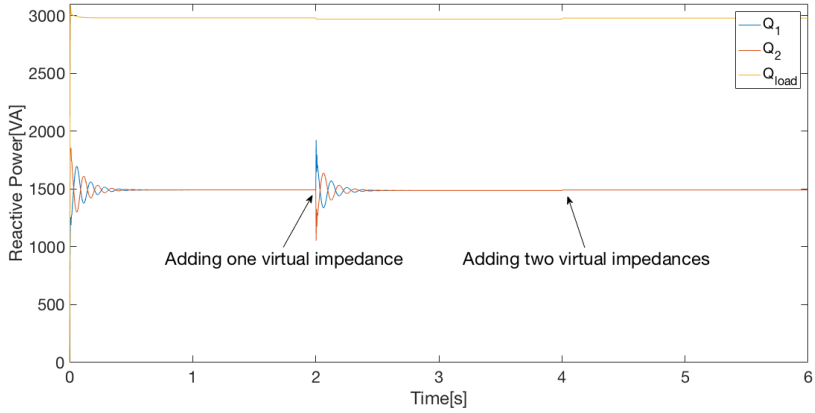


(b) Reactive Power

**Figure 4.2:** Power Flows with predominantly resistive physical impedance and opposite droop control

power supplied from the two inverters is therefore equal after t = 2 s.

The proposed impedance-matching method, which divides the single virtual impedance into two smaller virtual impedances, serves its purpose when it comes to the output voltage level. The two virtual impedances are equal in magnitude, but opposite in signs. With approximately the same power sharing as for one larger virtual impedance, Fig. 4.3 shows the ad-

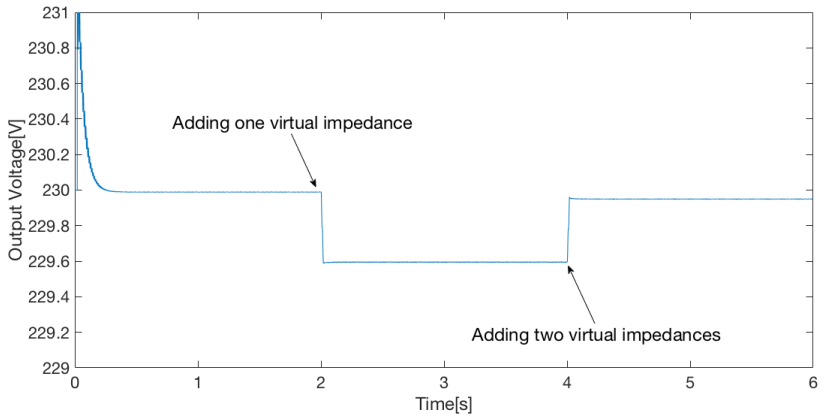


**Figure 4.3:** Output voltage with predominantly resistive physical impedance and opposite droop control

vantage of using this method. The voltage level at the load's connection point is increased at t = 4 s, close to the level delivered without using virtual impedances, from t = 0-2 s. By the proposed virtual impedance method, the voltage drop is reduced from 0.4 V to 0.04 V, i.e. with 90 % compared to the conventional virtual impedance method.

### 4.2.2 Case 1 b): Conventional Droop Control

As explained in Section 3.4.1, the characteristic of the conventional droop control can make it preferable compared to the opposite droop control, even in case of a predominantly resistive physical output impedance. The behavior of such a system is investigated through two separate simulations. The second simulation is divided into two, where two different virtual impedance methods are examined.

- First simulation: The conventional droop control is implemented without the use of virtual impedances.
- Second simulation, 0-2 seconds: Both inverters have inductive vir-

tual impedances, which is equal in size to the largest physical output impedance of the two inverters.

- Second simulation, 2-4 seconds: In addition to the inductive terms, negative virtual resistors are added to the inverters' control systems.

The values of the virtual resistances and inductances in the second simulation are listed in Tab. 4.5, using the same notation as in case 1 a). Time period 1 is here from t = 0 s to t = 2 s in simulation 2, while the second time period from t = 2 s to t = 4 s.

**Table 4.5:** Virtual resistance and inductance used in case 1 b)

| **Parameter** | **Value** |
|---|---|
| $L_{v1}^{1}$ | 1.6484 Ω |
| $L_{v2}^{1}$ | 1.6484 $mH$ |
| $R_{v1}^{2}$ | -0.2568 Ω |
| $L_{v1}^{2}$ | 1.6484 $mH$ |
| $R_{v2}^{2}$ | -0.2568 Ω |
| $L_{v2}^{2}$ | 1.6484 $mH$ |

In the first simulation, the use of the conventional droop control clearly leads to an unstable response, as shown by the power flows depicted in Fig. 4.4. The two inverters counteract each other, causing large and increasing circulating currents. The power flow from both inverters alternate, which indicates that the virtual impedance is essential for a stable operation. Before t = 0.25 s, inverter 2 feed more than the reactive power needed at the load alone, leading to an equivalent negative power flow from inverter 1. Just half a second later, the case is changed to be opposite, where inverter 1 is feeding the whole load. Figure 4.4(a) shows that the active power has a similar performance, also with a clearly unstable response.

In Fig. 4.5, the corresponding power flows are shown after the virtual impedances are applied to the system. The system is stable, with close

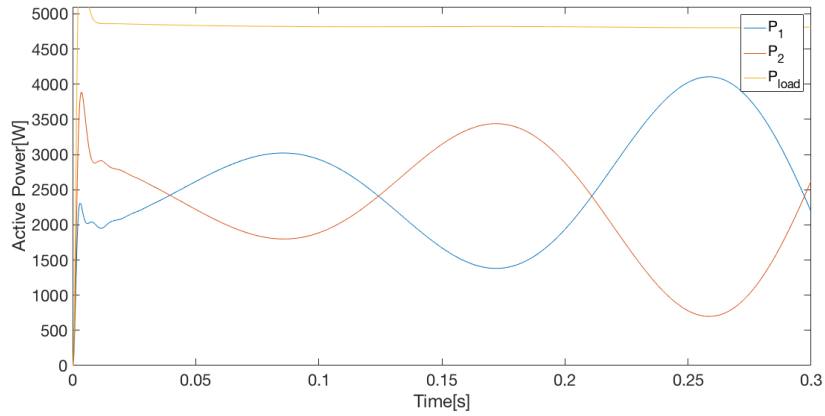


(a)

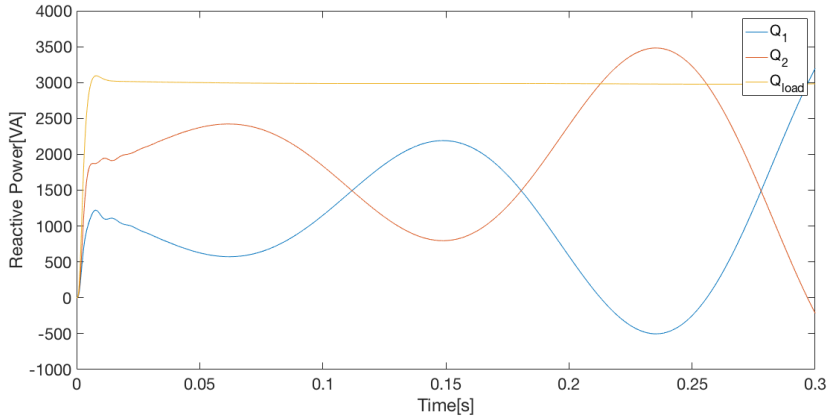


(b)

**Figure 4.4:** Power flows in the first simulation with predominantly resistive physical impedance and opposite droop control

to zero active circulating currents. The reactive power sharing is shown in Fig. 4.5(b). The load's reactive power is shared with 41 % supplied from inverter 1, and 59% from inverter 2. As in the previous case, there is no significant difference between the power sharing performance of the proposed- and the conventionally used virtual impedances. The phase-to-ground voltage is depicted in Fig. 4.6, and shows that the purely inductive

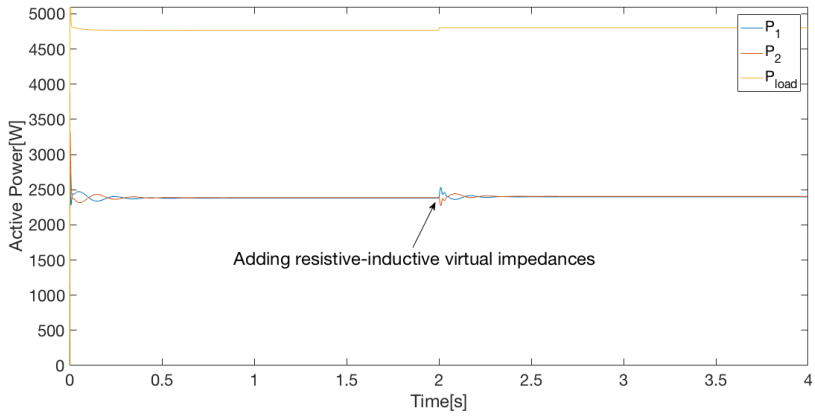


(a)

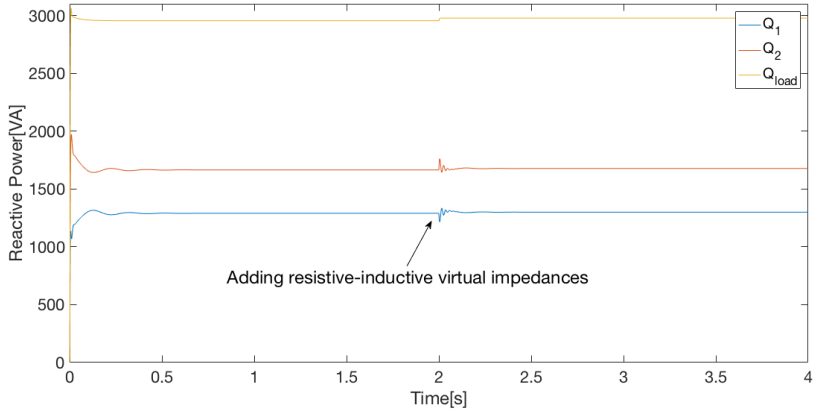


(b)

**Figure 4.5:** Power flows in the second simulation with predominantly resistive physical impedance and opposite droop control

virtual impedances cause a voltage drop of around 1 V. By adding negative resistors to the virtual impedances, the voltage drop is reduced by around 95 %.

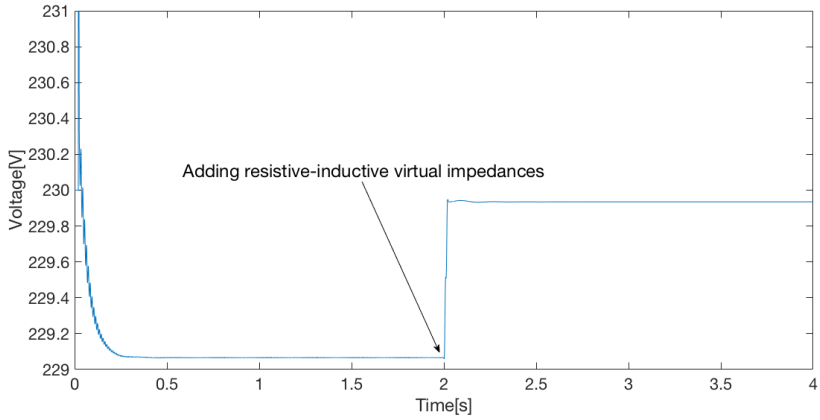


**Figure 4.6:** Output voltage in the second simulation with predominantly resistive physical impedance and opposite droop control

## 4.3 Case 2: Inductive Output Impedance

The output impedance of a microgrid can be dominated by the inductive behavior of components such as isolating transformers [71]. This is the case to be studied in this section, by using the conventional droop control in case 2 a) and the opposite droop control algorithm in case 2 b). A diagram showing a microgrid system including isolating transformers is depicted in Fig. 4.7.

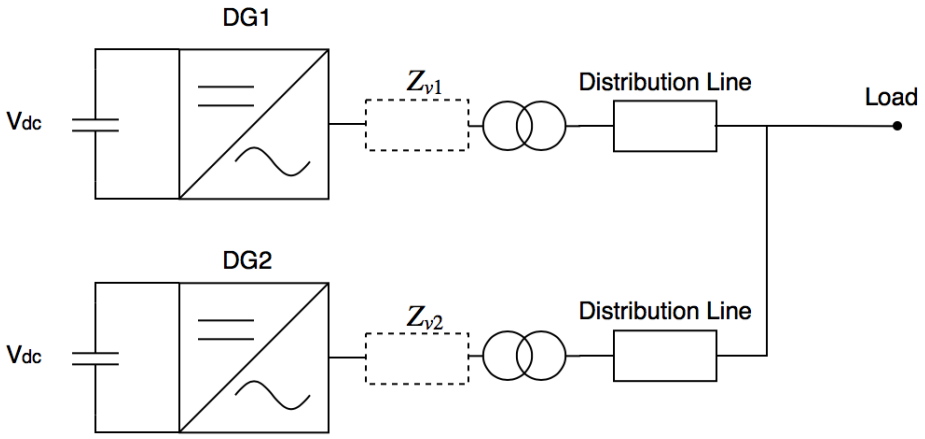


**Figure 4.7:** The investigated system in case 2

The parameters of the distribution lines used in the simulations, in this case, are based on the simulations from case 1, as explained in Section 2.4. The physical output impedance is equal as in case 1, but with a contribution from inductive components the distribution lines are 3-4 times shorter than in the previous case. The exact physical output impedances used in the simulations are presented in Tab. 4.6.

**Table 4.6:** Physical output impedances used in the inductive-dominating microgrid in case 2 and case 3

| Parameter | Value |
|---|---|
| $Z_{L1}$ | $0.1488 + j0.4969\Omega$ |
| $Z_{L2}$ | $0.0930 + j0.3100\Omega$ |

### 4.3.1 Case 2 a): Conventional Droop Control

The use of conventional droop control with predominantly inductive physical output impedances is presented in this section. As the other simulations, this one is divided into three time slots to easily compare the different methods. The methods presented here are similar to the methods in case 1 a).

- 0-2 seconds: The conventional droop control is implemented without the use of virtual impedances.
- 2-4 seconds: A virtual impedance compensating for the difference in physical output impedance is added.
- 4-6 seconds: The inverter located furthest from the load will have a positive virtual impedance equal to half of the value used in the previous time slot. A virtual impedance equal in size, but opposite in sign is added to the closest inverter.

The virtual impedances used in the simulations, in this case, are shown in Tab. 4.7, where t = 2-4 s and t = 4-6 s is denoted by time period 1 and time period 2, respectively.

The power sharing among the two inverters is depicted in Fig. 4.8, which distinctly shows that the power sharing performance of the conventional droop control is good when it comes to the active power. Ignoring the transient periods, the active circulating current is close to zero throughout the whole simulation period.

**Table 4.7:** Virtual resistance and inductance used in case 2 a)

| Parameter | Value |
|---|---|
| $R_{v2}^{1}$ | 0.0558 Ω |
| $L_{v2}^{1}$ | 0.592 $mH$ |
| $R_{v1}^{2}$ | -0.0279 Ω |
| $L_{v1}^{2}$ | -0.296 $mH$ |
| $R_{v2}^{2}$ | 0.0279 Ω |
| $L_{v2}^{2}$ | 0.296 $mH$ |

When it comes to the reactive power, this is unequally shared between the two inverters until t = 2 s. Inverter 1 accounts for 44 % of the reactive power delivered to the load, while inverter 2 supplies 56 %. This power sharing error is effectively solved by the use of virtual impedance, which is shown from t = 2 s. Both of the virtual impedance techniques effectively lead to same steady-state power sharing performance.

The phase-to-ground voltage level, depicted in Fig. 4.9, shows that the use of the proposed virtual impedance method leads to reducing the voltage drop by 94%, from 0.31 V to 0.02 V.

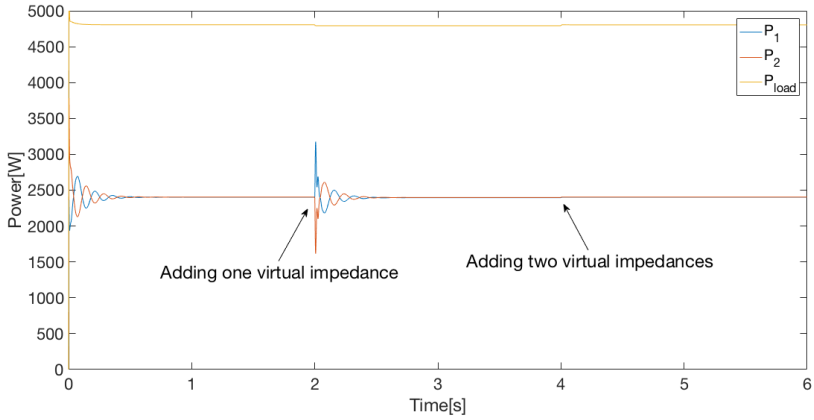


(a)

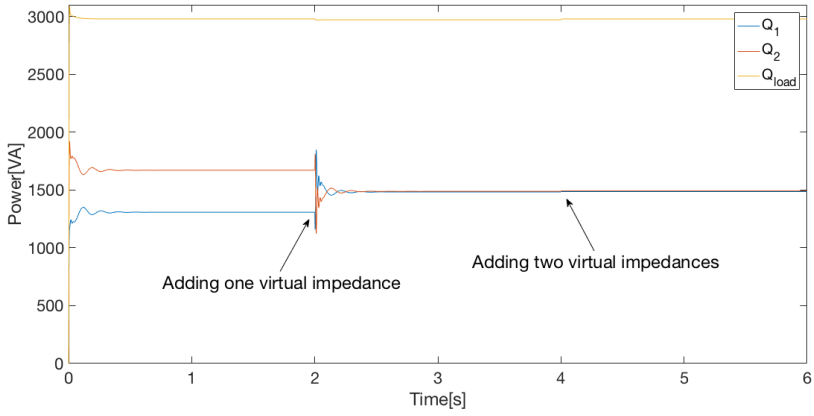


(b)

**Figure 4.8:** Power flows with predominantly inductive physical impedance and conventional droop control

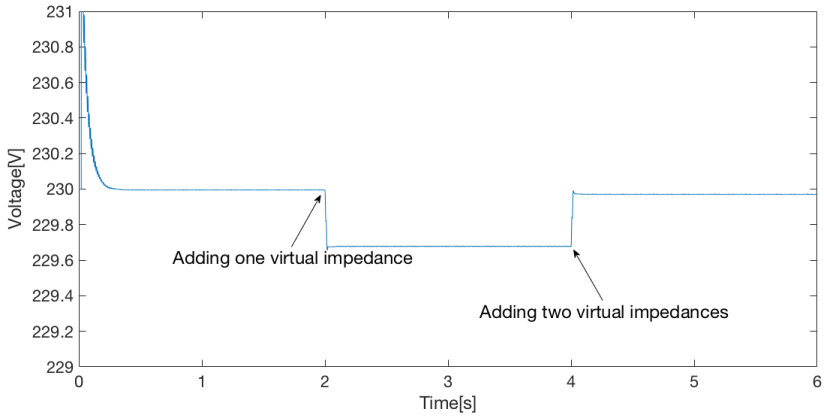


**Figure 4.9:** The output voltage with predominantly inductive physical impedance and conventional droop control

### 4.3.2 Case 2 b): Opposite Droop Control

As discussed in Section 3.4.1, the opposite droop control is normally used in cases with predominantly resistive physical output impedances. Because of the advantages of the opposite droop control discussed in Section 3.4.1, the opposite droop control can also be an option in grids with inductive physical output impedances [72]. The approach taken in this case is similar to the one used in case 1 b). Three different methods are utilized, carried out as two separate simulations.

- First simulation: The opposite droop control is implemented without the use of virtual impedances.
- Second simulation, 0-2 seconds: A resistive virtual impedance is added to both inverters to make the equivalent output impedance appear as predominantly resistive.
- Second simulation, 2-4 seconds: In addition to the resistive components, negative inductive virtual impedances are added. These are equal in size to the resistive component of the largest physical output impedance in the system.

**Table 4.8:** Virtual resistance and inductance used in case 2 b)

| Parameter | Value |
|---|---|
| $R^1_{v1}$ | 0.518 $\Omega$ |
| $R^1_{v2}$ | 0.518 $\Omega$ |
| $R^2_{v1}$ | 0.518 $\Omega$ |
| $L^2_{v1}$ | -789.3 $\mu H$ |
| $R^2_{v2}$ | 0.518 $\Omega$ |
| $L^2_{v2}$ | -789.3 $\mu H$ |

The use of opposite droop control with predominantly inductive physical output impedance lead to a clearly unstable response, as shown in

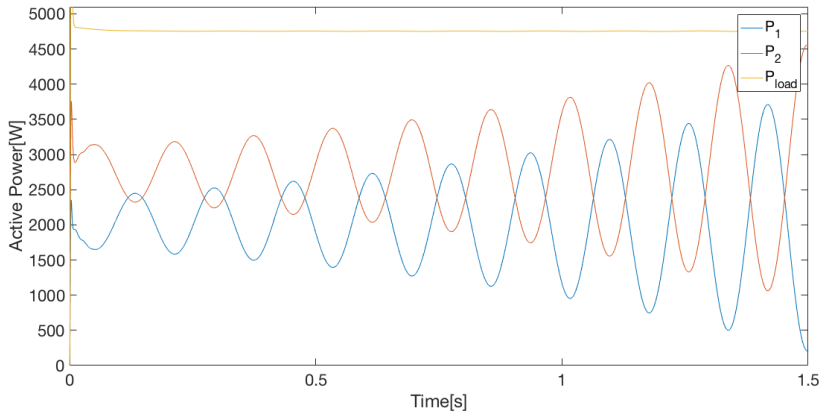


(a)

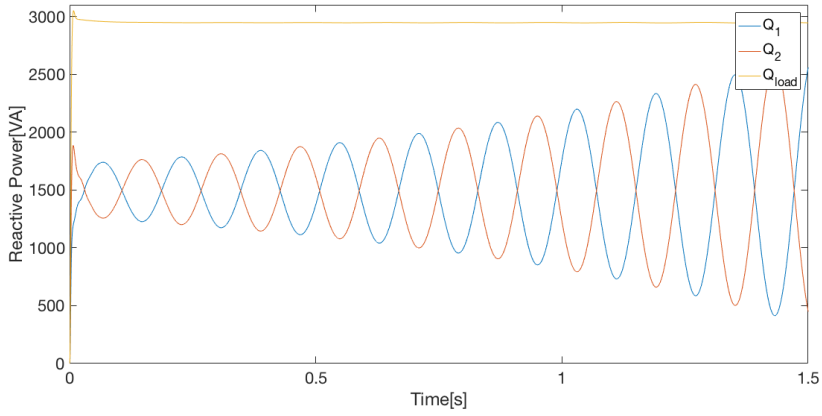


(b)

**Figure 4.10:** Active and reactive power in first simulation with predominantly inductive physical impedance and opposite droop control

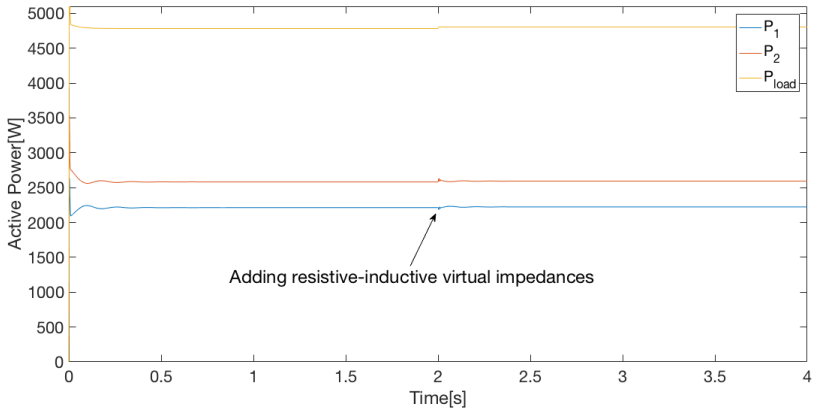


(a)

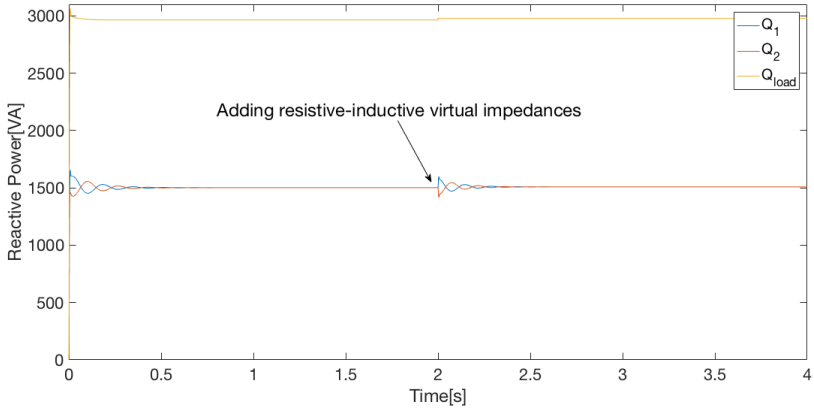


(b)

**Figure 4.11:** Power flows in second simulation with predominantly inductive physical impedance and opposite droop control

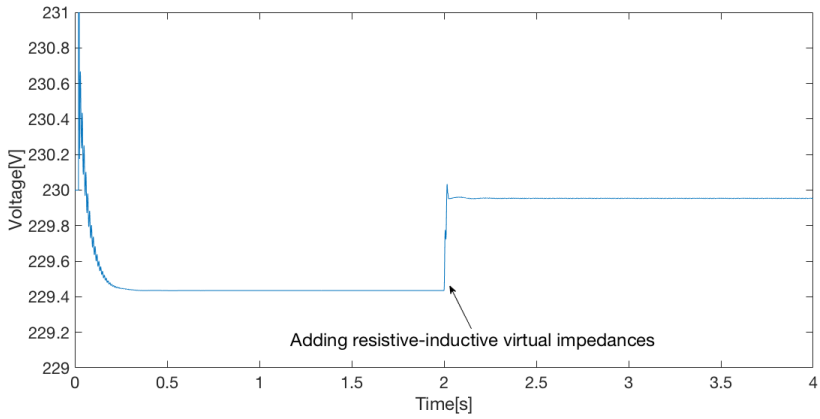


**Figure 4.12:** Output voltage in second simulation with predominantly inductive physical impedance and opposite droop control

Fig.4.10. The powers are alternating with increasing amplitude, resulting in large circulating currents.

The system gets a stable response when utilizing virtual impedance methods, as shown by the power flows from the second simulation in Fig. 4.11. The purely resistive virtual impedances give a behavior almost equivalent to the first time period in case 2 a), with accurate reactive power sharing. The active power is shared with 46 % supplied from inverter 1, and 54 % supplied from inverter 2. The power sharing is not significantly changed when the virtual inductive components are added at t = 2 s.

Figure 4.12 shows the phase-to-ground voltage level at the load's connection point. The voltage drop caused by the resistive virtual impedances are almost canceled by adding the negative inductive impedances. The voltage drop is reduced by 93 % utilizing the proposed virtual impedance method.

## 4.4 Case 3: Estimated Inductive Output Impedance

In the previous cases, the inverters' physical output impedance are assumed to be known. In an actual microgrid, this is normally not the case. This case considers the same cases as those including virtual impedances in case 2. The physical output impedances of the inverters are estimated 25 % lower than the actual values. Since the virtual impedances are selected based on the physical output impedances, the estimations affect their values. The other parameters used in the simulations in this case are the same as in case 2. The physical output impedances are given by Tab. 4.6.

### 4.4.1 Case 3 a): Conventional Droop Control

This case is a reproduction of case 2 a), with use of conventional droop control with predominantly inductive physical output impedances. The simulation is divided into three time slots, as in case 2 a).

- 0-2 seconds: The conventional droop control is implemented without use of virtual impedances.
- 2-4 seconds: A virtual impedance compensating for the difference in physical output impedance is added.
- 4-6 seconds: The inverter located furthest from the load will have a positive virtual impedance equal to half of the value used in the previous time slot. A virtual impedance equal in size, but opposite in sign is added to the closest inverter.

The physical output impedances are assumed to be estimated to be 75 % of the actual physical output impedances. Since the estimated physical output impedances are used to select the virtual impedances, the virtual impedances in this case are 25 % lower than in case 2 a). The virtual

impedances used are shown in Tab. 4.9, where the time periods t = 2-4 s and t = 4-6 s are denoted by time period 1 and time period 2, respectively.

**Table 4.9:** Virtual resistance and inductance used in case 3 a)

| **Parameter** | **Value** |
|---|---|
| $R_{v2}^{1}$ | 0.0418 Ω |
| $L_{v2}^{1}$ | 0.440 $mH$ |
| $R_{v1}^{2}$ | -0.0209 Ω |
| $L_{v1}^{2}$ | -0.220 $mH$ |
| $R_{v2}^{2}$ | 0.0209 Ω |
| $L_{v2}^{2}$ | 0.220 $mH$ |

The power flows from the two inverters are depicted in Fig. 4.13. This figure shows that with 25 % error in the physical output impedance estimations, the effect of the virtual impedances is similar to case 2 a), but with relatively small reactive circulating currents. The power sharing with the conventionally used and the proposed virtual impedance method is effectively equal, as shown in Fig. 4.13. The active power is shared equally among the inverters. With known physical output impedances in case 2 a), the virtual impedances provided almost perfect compensation, resulting in approximately zero circulating currents when they where applied to the system. In this case, a small circulating current appears, where inverter 1 feeds around 48 % of the reactive power, while inverter 2 delivers the remaining 52 %.

In Fig. 4.14, the load's phase-to-ground voltage is shown, which is similar to the voltage level in case 2 a). The voltage drop related to the virtual impedance is reduced by around 91 % by using the proposed virtual impedance method, which is slightly less than in the case with known physical output impedances.

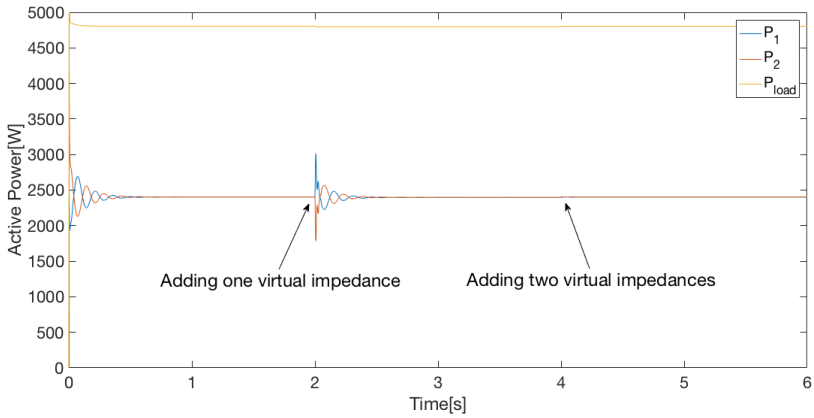


(a)

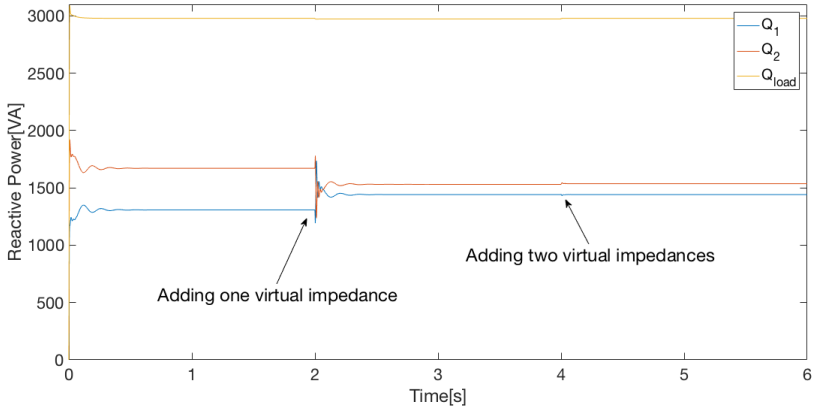


(b)

**Figure 4.13:** Power flows in second simulation with estimated predominantly inductive physical impedance and conventional droop control

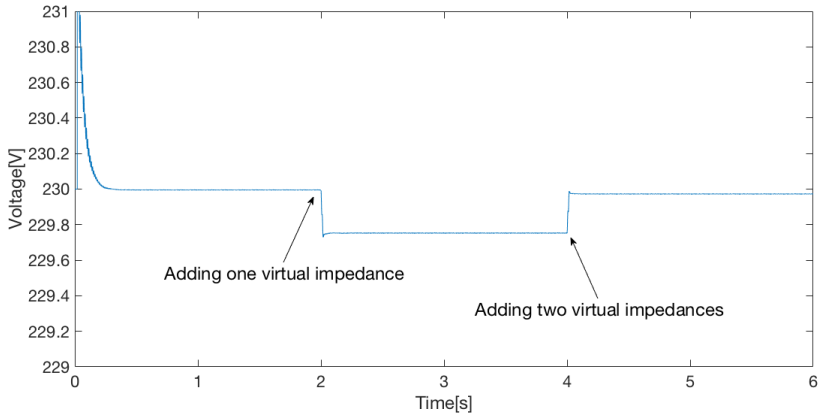


**Figure 4.14:** Output voltage with estimated inductive physical impedance and conventional droop control

### 4.4.2 Case 3 b): Opposite Droop Control

In this case, the simulations including virtual impedances carried out in case 2 b) are reproduced. The physical output impedances are however estimated to be 75 % of the actual values. Case 3 b) will present one simulation, which is divided into two time slots:

- 0-2 seconds: A resistive virtual impedance is added to both inverters to make the equivalent output impedance appear as predominantly resistive.
- 2-4 seconds: In addition to the resistive components, negative inductive impedances are added, equal in size to the resistive component of the largest output impedance in the system.

With the physical output impedances estimated to be 25 % lower than the actual values, the virtual impedances are reduced by the same factor compared to case 2 b). The virtual impedances used in the simulations are listed in Tab. 4.10. Time period 1 and time period 2 are t = 0-2 s and t = 2-4 s, respectively.

**Table 4.10:** Virtual resistance and inductance used in case 3 b)

| Parameter | Value |
|---|---|
| $R^1_{v1}$ | 0.388 $\Omega$ |
| $R^1_{v2}$ | 0.388 $\Omega$ |
| $R^2_{v1}$ | 0.388 $\Omega$ |
| $L^2_{v1}$ | -592 $\mu F$ |
| $R^2_{v2}$ | 0.388 $\Omega$ |
| $L^2_{v2}$ | -592 $\mu F$ |

As when the physical output impedances are known, Fig. 4.15 shows that the reactive power is equally shared among the inverters. The active power flows are also similar to case 2 b). Inverter 1 feeds 46 % of the

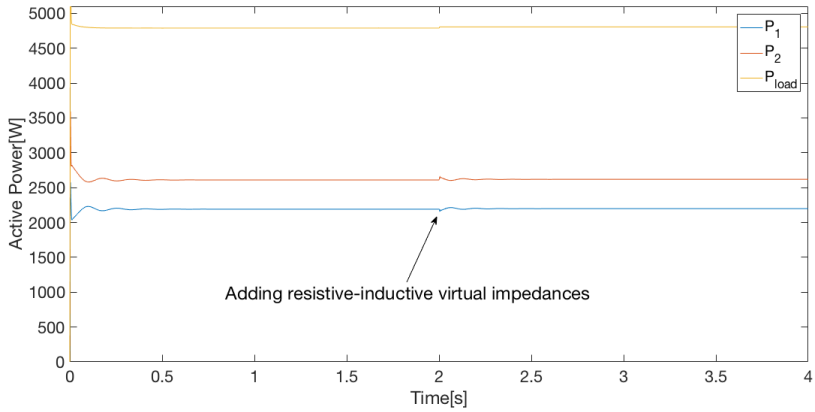


(a)

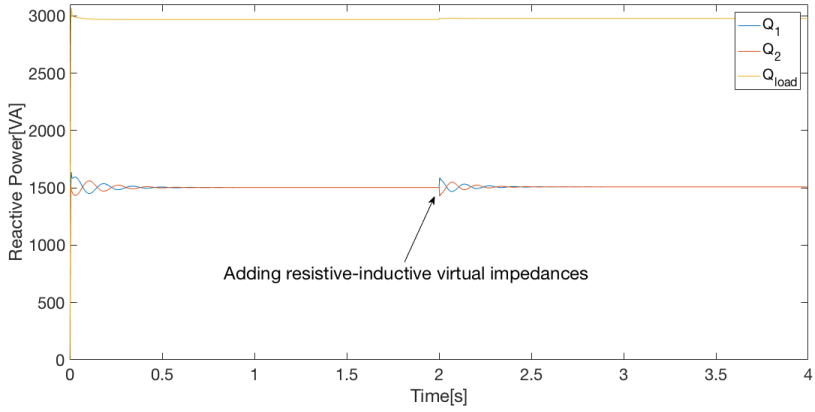


(b)

**Figure 4.15:** Power flows with estimated predominantly inductive physical impedance and opposite droop control

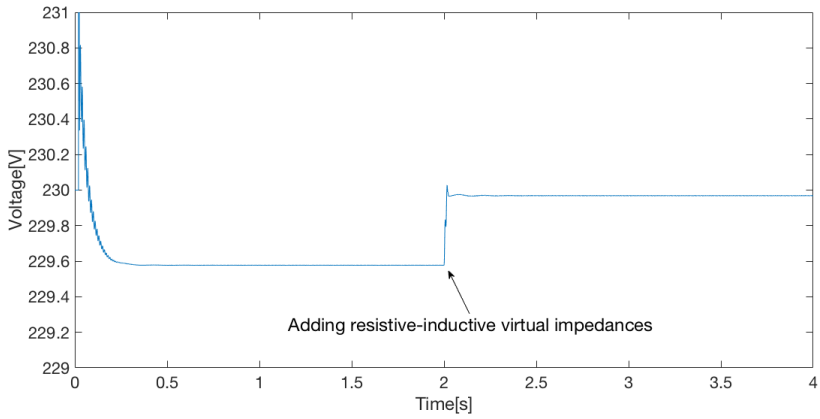


**Figure 4.16:** Output voltage with estimated inductive physical impedance and opposite droop control

load's active power, while inverter 2 delivers 56 %. The circulating current is slightly larger than with known physical output impedances.

The load's phase-to-ground voltage level is shown in Fig. 4.16. With the proposed virtual impedance method, the voltage drop due to the virtual impedances is reduced by 95 % compared to the purely resistive virtual impedance.

## 4.5 Discussion

The islanded microgrid system is implemented and tested through different case studies. The simulations show that the use of virtual impedances improves the power sharing among inverters. The proposed virtual impedance methods have the same power sharing performance as existing methods, but the voltage drop across the virtual impedances are significantly reduced. In this section, simplifications and possible improvements related to the microgrid systems are discussed.

The case studies has shown how virtual impedances are used to improve power sharing among paralleled inverters. A presentation of proposed virtual impedance methods are done, where the methods aim for sufficient power sharing, with less effect on the output voltage. Virtual impedance methods are proposed in six different cases. The simulation results show that for all cases, the proposed methods achieve at least 90 % reduced voltage drop compared to existing virtual impedance solutions. By using the proposed approaches, a larger portion of the power sharing control can be moved from the centralized to the distributed control. With a negligible voltage drop caused by the virtual impedances, the droop controller's voltage reference does not have to be changed because of a load shift, which can have been the case when using the existing virtual impedance methods.

A disadvantage of the proposed method utilized in case 1 a), 2 a) and 3 a), is that the method is dependent on having an even number of inverters, since the virtual impedances are implemented as pairs. Each inverter with a positive virtual impedance should always have another inverter with the same virtual impedance, but with opposite sign. This method may therefore face challenges when having an odd number of inverters.

Another scenario, which will be challenging both when using the conventional and the proposed virtual impedance method used in case 1 a),

2 a) and 3 a), is to have loads connected at several locations in the microgrid. In real life, this would normally be the case. With several loads at different locations in the grid, both the existing- and the proposed impedance matching technique used in case 1 a), 2 a) and 3 a) will have a significant reduction in power sharing performance. Utilization of both the impedance matching techniques presented in this thesis can possibly lead to unstable behavior in a microgrid with several connection points for loads.

The second proposed method, which is utilized in case 1 b), 2 b) and 3 b), may experience challenges related to the selection of the negative component of the virtual impedances. When the method is applied to the conventional droop control method, the virtual impedance will have a positive inductive and a negative resistive component. If the resistive value is selected too large, it can possibly compensate for all of the resistive effects in the physical output impedance. The equivalent output impedances of the inverters will appear as purely inductive. As discussed in Section 3.4.1, a purely inductive output impedance would lead to an unstable behavior, because of no damping effect which is normally utilized by the resistive components [9, chapter 3].

When modelling the microgrid systems, simplifications have been done. One of the largest is the use of the average model VSIs. This inverter model does not produce harmonic oscillations or take inverter losses into consideration. Due to this simplification, harmonic power sharing is not considered. The advantage of the average model is mainly related to the computational time when doing simulations, where this model allows the step size to be larger than alternative methods does. Because of the reduced computational time, this model is preferred instead of more accurate models.

Another simplification is related to the representation of the DG units. They are modelled as ideal dc voltage sources, and are therefore assumed to have an infinite amount of available power. The assumption is done on

the background of this work's main goal, which is focused on studying the power sharing performance for inverters with different physical output impedances. The use of dc voltage sources is for this purpose considered as good enough, since it is focused on the steady-state performance. Most of the reviewed publications focused on power sharing also use this assumption. In a more complete study, the DG units could have been represented with fluctuating power production. In addition, batteries could have been considered to be both charged and discharged, depending on the production and loads in the system.

When considering the simulation results, there are several aspects that should be mentioned. The voltage drops caused by the virtual impedances used in the case studies are relatively small, maximum 1 V. Thus, the proposed methods can be more valuable in a grid with a larger load, which will have a larger voltage drop considering the same voltage level. Since the microgrid feeds a single residential load, a system including a larger load is seen as realistic.

In all the simulations, the parameters of the distribution lines and other components in the grid are assumed to be known, which implies that the physical output impedance is known. This is rarely the case in a real life microgrid, where the parameters often have to be estimated, for instance by using standard values as in Tab. 2.2 [9, chapter 3]. Simulation case 3 is a reproduction of simulation case 2, but the physical output impedances are estimated to be 25 % below the actual values. This is considered as a relatively large error. The results from the two cases are however similar, with only slightly larger circulating currents in case 3. The voltage drops from the virtual impedances are significantly reduced, both in case 3 a) and b). The results thereby show that the virtual impedance methods seem to work also with roughly estimated line impedances, but with a slightly reduced power sharing performance. The proposed virtual impedance methods uti-

lized show an improved behavior compared to the more conventional virtual impedance methods, also in case 3. The two methods provide the same power sharing performance, but the proposed virtual impedance method has an improved voltage level compared to the more conventional virtual impedance method.

The lengths of the predominantly resistive distribution lines used in case 1 are selected to be 500m and 800m. This is considered to be a reasonable difference between the inverters, but also reasonable lengths, relative to the voltage level and the size of the load. With much longer distribution lines, the voltage level of the power system will probably be considered increased, in order to reduce transmission losses [73, chapter 2]. With predominantly inductive physical output impedance in case 2 and 3, the lengths of the distribution lines are assumed to be shorter than in case 1. If the lengths of the lines are increased, it would cause a decreased X/R-ratio, since the distribution lines' impedance will amount to a larger portion of the physical output impedance of the inverters. This would increase the coupling between active and reactive power, which may lead to new requirements, for instance in the selection of the virtual impedances.

This study presents promising results, but should be considered as a preliminary study within the use of virtual impedance for power sharing purposes. The results are carried out based on one specific system, which is based on two ideal inverter-based generation units.

As mentioned, a set of limitations is related to the study. Further investigation should be done, reducing the number of limitations in order to achieve a more complete analysis. Even though there is a need for more research on the topic, it should be noticed that the proposed methods in this thesis achieve improved voltage level without reducing the power sharing performance, compared to the more conventional virtual impedance methods. This utilization of virtual impedance in the distributed control may

therefore make it easier to offer plug-and-play capability, in order to achieve a microgrid which can be easily expanded.

The first suggestion for future work is to do laboratory experiments to validate the simulation results. A laboratory setup is planned, as shown in Fig. 4.17. This setup includes hardware-in-the-loop simulations [74], where the microgrid's inverters and filters are implemented as hardware, while the distribution lines and loads are software. The control systems utilized in this thesis can by the setup shown in Fig. 4.17 be used in a more realistic system, controlling actual inverters.

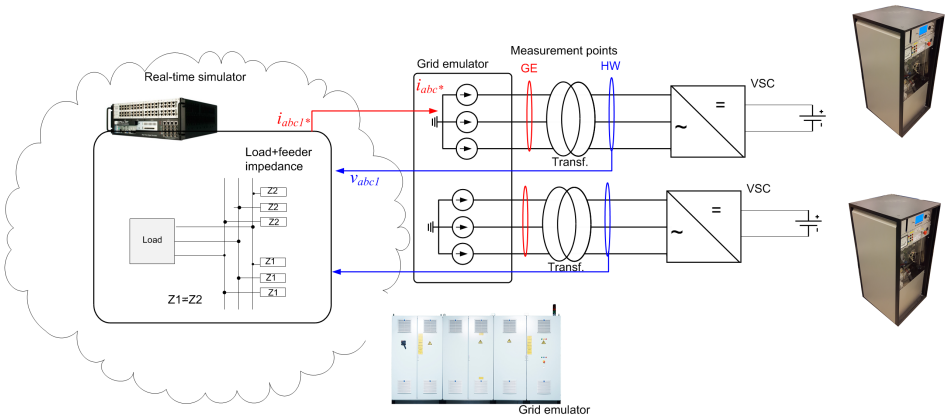


**Figure 4.17:** A representation of a laboratory setup for a microgrid. Used by permission of FME CINELDI.

In addition to a reproduction of the modelling done in this study, it would be interesting to investigate the use of non-linear loads, which possibly lead to further challenges related to the inverters' power sharing performance. The average model VSI can be substituted with a more realistic inverter, in order to investigate harmonic oscillations in the microgrid, as well as their effect on the power sharing. All these aspects could have been considered in an expanded microgrid with several inverters and variable loads.

# 5 | Conclusion

An islanded microgrid system is modelled in order to investigate power sharing between paralleled DG units with different output impedances. In the studied system, two DG units connected through inverters are modelled to feed one linear load. This thesis shows the distributed control structure, including the inner- and primary control. The inner control includes voltage and current control, while the primary control contains a droop control algorithm which takes care of voltage and frequency levels. In this loop, the output impedances of the inverters are modified by use of virtual impedances, which contribute to improved power sharing among the inverters. Six different cases are considered, and it is investigated how virtual impedance can be used to utilize different control systems in grids with mismatching physical output impedances. The system is validated through simulations, divided into three main cases.

Case 1 represents the microgrid system with predominantly resistive physical output impedances. Two different droop control algorithms, conventional and opposite droop control, are considered. In order to improve power sharing, the effectiveness of virtual impedances is validated through simulations. Proposed solutions show how virtual impedances can be used with power sharing performance similar to the conventional methods. The voltage drops due to the virtual impedances are however significantly reduced by utilizing these solutions.

In case 2, predominantly inductive physical output impedances are studied. The same droop control methods are used, and virtual impedance techniques are utilized. As in case 1, existing virtual impedance methods are validated, including proposed solutions with less effect on the voltage levels. The proposed solutions lead to reduced voltage drops, and the power sharing performance is practically the same as for the already existing virtual impedance methods.

In simulation case 3, it is shown that with predominantly inductive physical output impedance roughly estimated, virtual impedance methods can improve the power sharing. At the same time, only small voltage drops are experienced across the proposed virtual impedances. The power sharing performance is however reduced compared to the ideal case, where the physical output impedances are known.

This thesis presents promising results, where virtual impedance methods show well-working power sharing performance, in addition to minor effects on the output voltage level. The results should still be seen as a preliminary study, due to the assumptions that are done. For further work, it is suggested to perform laboratory experiments in order to validate the simulations in a more realistic sceanario. In addition, expansions of the microgrid, the use of non-linear loads and inclusion of more application oriented simulations can be part of future research on the topic of power sharing in islanded ac microgrids.

# Bibliography

[1] Joan Rocabert, Alvaro Luna, Frede Blaabjerg, and Pedro Rodriguez. Control of power converters in ac microgrids. *IEEE transactions on power electronics*, 27(11):4734–4749, 2012.

[2] The paris agreement - status of ratification. http://unfccc.int/paris_agreement/items/9444.php. Accessed: 2018-12-03.

[3] The paris agreement. http://unfccc.int/paris_agreement/items/9485.php. Accessed: 2018-12-03.

[4] The impact of population momentum on future population growth. https://esa.un.org/unpd/wpp/Publications/Files/PopFacts_2017-4_Population-Momentum.pdf. Accessed: 2018-12-03.

[5] Renewable energy: A key climate solution. https://www.irena.org/-/media/Files/IRENA/Agency/Publication/2017/Nov/IRENA_A_key_climate_solution_2017.pdf?la=en&hash=A9561C1518629886361D12EFA11A051E004C5C98. Accessed: 2018-24-05.

[6] Daniel E Olivares, Ali Mehrizi-Sani, Amir H Etemadi, Claudio A Cañizares, Reza Iravani, Mehrdad Kazerani, Amir H Hajimiragha, Oriol Gomis-Bellmunt, Maryam Saeedifard, Rodrigo Palma-Behnke, et al. Trends in microgrid control. *IEEE Transactions on smart grid*, 5(4):1905–1919, 2014.

[7] Key world energy statistics. `https://www.iea.org/publications/freepublications/publication/KeyWorld2017.pdf`. Accessed: 2017-12-17.

[8] Renewablles 2016: Global status report. `http://www.ren21.net/wp-content/uploads/2016/06/GSR_2016_Full_Report.pdf`. Accessed: 2018-24-05.

[9] Nikos Hatziargyriou et al. *Microgrids: architectures and control*. Wiley Online Library, 2014.

[10] SM Shinde, KD Patil, SS Khairnar, and WZ Gandhare. The role of power electronics in renewable energy systems research and development. In *Emerging Trends in Engineering and Technology (ICETET), 2009 2nd International Conference on*, pages 726–730. IEEE, 2009.

[11] Ching-Tsai Pan and Yi-Hung Liao. Modeling and coordinate control of circulating currents in parallel three-phase boost rectifiers. *IEEE Transactions on Industrial Electronics*, 54(2):825–838, 2007.

[12] Santiago Grijalva and Muhammad Umer Tariq. Prosumer-based smart grid architecture enables a flat, sustainable electricity industry. In *Innovative Smart Grid Technologies (ISGT), 2011 IEEE PES*, pages 1–6. IEEE, 2011.

[13] About microgrids. `http://www.microgridinstitute.org/about-microgrids.html`. Accessed: 2018-10-04.

[14] Robert H Lasseter. Microgrids. In *Power Engineering Society Winter Meeting, 2002. IEEE*, volume 1, pages 305–308. IEEE, 2002.

[15] Joan Rocabert, Alvaro Luna, Frede Blaabjerg, and Pedro Rodriguez. Control of power converters in ac microgrids. *IEEE transactions on power electronics*, 27(11):4734–4749, 2012.

[16] Farid Katiraei, Reza Iravani, Nikos Hatziargyriou, and Aris Dimeas. Microgrids management. *IEEE power and energy magazine*, 6(3), 2008.

[17] Hua Han, Xiaochao Hou, Jian Yang, Jifa Wu, Mei Su, and Josep M Guerrero. Review of power sharing control strategies for islanding operation of ac microgrids. *IEEE Transactions on Smart Grid*, 7(1):200–215, 2016.

[18] TL Vandoorn, JM Guerrero, JDM De Kooning, J Vásquez, and L Vandevelde. Decentralized and centralized control of islanded microgrids including reserve management. *IEEE Ind Electron Mag*, pages 1–14, 2013.

[19] Anders Bergheim Holvik. Control of power electronics in microgrids, 2017.

[20] Stavros Papathanassiou, Nikos Hatziargyriou, Kai Strunz, et al. A benchmark low voltage microgrid network. In *Proceedings of the CIGRE symposium: power systems with dispersed generation*, pages 1–8, 2005.

[21] Yasser Mohamed. New control algorithms for the distributed generation interface in grid-connected and micro-grid systems. 2008.

[22] Mohammad Hadi Andishgar, Eskandar Gholipour, and Rahmat-allah Hooshmand. An overview of control approaches of inverter-based microgrids in islanding mode of operation. *Renewable and Sustainable Energy Reviews*, 80:1043–1060, 2017.

[23] Jan Bauer, Jiri Lettl, Petr Pichlik, and Jiri Zdenek. Low power photovoltaic converter control and development. *Transactions on Electrical Engineering*, 1(3), 2012.

[24] Utsav P Yagnik and Mehul D Solanki. Comparison of l, lc & lcl filter for grid connected converter. In *Trends in Electronics and Informatics (ICEI), 2017 International Conference on*, pages 455–458. IEEE, 2017.

[25] Vegard Moritsgård Flatjord. Active filter capability of a voltage source inverter in marine applications. Master's thesis, NTNU, 2017.

[26] Anca Julean. Active damping of lcl filter resonance in grid connected applications. *Aalborg Universitet, Dinamarca, Dissertação de mestrado*, 2009.

[27] Hisham Mahmood, Dennis Michaelson, and Jin Jiang. Accurate reactive power sharing in an islanded microgrid using adaptive virtual impedances. *IEEE Transactions on Power Electronics*, 30(3):1605–1617, 2015.

[28] Ned Mohan, Tore Undeland, and William P. Robbins. *Power electronics: converters, applications, and design*. John Wiley & Sons, 3rd edition, 2003.

[29] Temesgen Mulugeta Haileselassie. Control, dynamics and operation of multi-terminal vsc-hvdc transmission systems. 2012.

[30] Technical guide specifications power wave 3. https://www.onlinepower.com/pdf/powerwave3_TS.pdf. Accessed: 2018-30-05.

[31] Universal bridge. https://se.mathworks.com/help/physmod/sps/powersys/ref/universalbridge.html. Accessed: 2017-12-02.

[32] Zhongming Ye, Praveen K Jain, and Paresh C Sen. Circulating current minimization in high-frequency ac power distribution architecture with multiple inverter modules operated in parallel. *IEEE Transactions on Industrial Electronics*, 54(5):2673–2687, 2007.

[33] Ching-Tsai Pan and Yi-Hung Liao. Modeling and control of circulating currents for parallel three-phase boost rectifiers with different load sharing. *IEEE Transactions on Industrial Electronics*, 55(7):2776–2785, 2008.

[34] Wei Yao, Min Chen, José Matas, Josep M Guerrero, and Zhao-Ming Qian. Design and analysis of the droop control method for parallel inverters considering the impact of the complex impedance on the power sharing. *IEEE Transactions on Industrial Electronics*, 58(2):576–588, 2011.

[35] Xiongfei Wang, Frede Blaabjerg, and Zhe Chen. An improved design of virtual output impedance loop for droop-controlled parallel three-phase voltage source inverters. In *Energy Conversion Congress and Exposition (ECCE), 2012 IEEE*, pages 2466–2473. IEEE, 2012.

[36] Usman Bashir Tayab, Mohd Azrik Bin Roslan, Leong Jenn Hwai, and Muhammad Kashif. A review of droop control techniques for

microgrid. *Renewable and Sustainable Energy Reviews*, 76:717–727, 2017.

[37] Prasenjit Basak, S Chowdhury, S Halder nee Dey, and SP Chowdhury. A literature review on integration of distributed energy resources in the perspective of control, protection and stability of microgrid. *Renewable and Sustainable Energy Reviews*, 16(8):5545–5556, 2012.

[38] Josep M Guerrero, Juan C Vasquez, José Matas, Luis García De Vicuña, and Miguel Castilla. Hierarchical control of droop-controlled ac and dc microgrids—a general approach toward standardization. *IEEE Transactions on Industrial Electronics*, 58(1):158–172, 2011.

[39] K De Brabandere, B Bolsens, J Van den Keybus, A Woyte, J Driesen, R Belmans, and K U Leuven. A voltage and frequency droop control method for parallel inverters. *Power Electronics Specialists Conference, 2004. PESC 04. 2004 IEEE 35th Annual*, 4(4):2501–2507 Vol.4, 2004.

[40] Azziddin M Razali, M Azizur Rahman, and Nasrudin A Rahim. Implementation of dq decoupling and feed-forward current controller for grid connected three phase voltage source converter. In *Industry Applications Society Annual Meeting, 2014 IEEE*, pages 1–8. IEEE, 2014.

[41] Jens G Balchen, Trond Andresen, and Bjarne A. Foss. *Reguleringsteknikk*. Institutt for Teknisk Kybernetikk, NTNU, 2003.

[42] Ned Mohan. *Advanced electric drives: analysis, control and modeling using MATLAB/Simulink*. Wiley, 2014.

[43] Roy Nilsen. Tet4120 electric drives. *Department of Electrical Engineering, NTNU, Trondheim*, 2016.

[44] Ned Mohan. *Electric machines and drives: a first course*. John Wiles & Sons, 2012.

[45] Santiago Sanchez, Gilbert Bergna, and Elisabetta Tedeschi. Tuning of control loops for grid-connected modular multilevel converters under a simplified port representation for large system studies. In *Ecological Vehicles and Renewable Energies (EVER), 2017 Twelfth International Conference on*, pages 1–8. IEEE, 2017.

[46] Jan Machowski, Janusz W. Bialek, and James R. Bumby. *Power System Dynamics. Stability and Control*. John Wiley & Sons, 2nd edition, 2014.

[47] Lianqing Zheng, Chen Zhuang, Jian Zhang, and Xiong Du. An enhanced droop control scheme for islanded microgrids. *International Journal of Control and Automation*, 8(4):63–74, 2015.

[48] Qing-Chang Zhong and Yu Zeng. Can the output impedance of an inverter be designed capacitive? In *IECON 2011-37th Annual Conference on IEEE Industrial Electronics Society*, pages 1220–1225. IEEE, 2011.

[49] Alexander Micallef, Maurice Apap, Cyril Spiteri-Staines, Josep M Guerrero, and Juan C Vasquez. Reactive power sharing and voltage harmonic distortion compensation of droop controlled single phase islanded microgrids. *IEEE Transactions on Smart Grid*, 5(3):1149–1158, 2014.

[50] Alexandra Von Meier. *Electric power systems: a conceptual introduction*. John Wiley & Sons, 2006.

[51] Islam Ziouani, Djamel Boukhetala, Abdel-Moumen Darcherif, Bilal Amghar, and Ikram El Abbassi. Hierarchical control for flexible microgrid based on three-phase voltage source inverters operated in parallel. *International Journal of Electrical Power & Energy Systems*, 95:188–201, 2018.

[52] Alfred Engler and Nikos Soultanis. Droop control in lv-grids. In *Future Power Systems, 2005 International Conference on*, pages 6–pp. IEEE, 2005.

[53] Guzman Diaz, Cristina Gonzalez-Moran, Javier Gomez-Aleixandre, and Alberto Diez. Scheduling of droop coefficients for frequency and voltage regulation in isolated microgrids. *IEEE Transactions on Power Systems*, 25(1):489–496, 2010.

[54] Xiaochao Hou, Yao Sun, Wenbin Yuan, Hua Han, Chaolu Zhong, and Josep M Guerrero. Conventional p-$\omega$/qv droop control in highly resistive line of low-voltage converter-based ac microgrid. *Energies*, 9(11):943, 2016.

[55] Yasser Abdel-Rady Ibrahim Mohamed and Ehab F El-Saadany. Adaptive decentralized droop controller to preserve power sharing stability of paralleled inverters in distributed generation microgrids. *IEEE Transactions on Power Electronics*, 23(6):2806–2816, 2008.

[56] Josep M Guerrero, José Matas, Luis Garcia de Vicuna, Miguel Castilla, and Jaume Miret. Decentralized control for parallel operation of distributed generation inverters using resistive output impedance. *IEEE Transactions on industrial electronics*, 54(2):994–1004, 2007.

[57] Estefanía Planas, Asier Gil-de Muro, Jon Andreu, Iñigo Kortabarria, and Iñigo Martínez de Alegría. General aspects, hierarchical controls

and droop methods in microgrids: A review. *Renewable and Sustainable Energy Reviews*, 17:147–159, 2013.

[58] Ping Zhang, Hengyang Zhao, Huanyu Cai, Jianjiang Shi, and Xiangning He. Power decoupling strategy based on virtual negative resistor for inverters in low-voltage microgrids. *IET Power Electronics*, 9(5):1037–1044, 2016.

[59] Yun Wei Li and Ching-Nan Kao. An accurate power control strategy for power-electronics-interfaced distributed generation units operating in a low-voltage multibus microgrid. *IEEE Transactions on Power Electronics*, 24(12):2977–2988, 2009.

[60] Meng Chen and Xiangning Xiao. Hierarchical frequency control strategy of hybrid droop/vsg-based islanded microgrids. *Electric Power Systems Research*, 155:131–143, 2018.

[61] Andrew D Paquette and Deepak M Divan. Virtual impedance current limiting for inverters in microgrids with synchronous generators. *IEEE Transactions on Industry Applications*, 51(2):1630–1638, 2015.

[62] Apap M. Micallef, A. and C. Spiteri-Staines. Performance comparison for virtual impedance techniques used in droop controlled islanded microgrids. *International Symposium on Power Electronics*, pages 695–700, 2016.

[63] Xiongfei Wang, Yun Wei Li, Frede Blaabjerg, and Poh Chiang Loh. Virtual-impedance-based control for voltage-source and current-source converters. *IEEE Transactions on Power Electronics*, 30(12):7019–7037, 2015.

[64] Xiangyu Wu, Chen Shen, and Reza Iravani. Feasible range and optimal value of the virtual impedance for droop-based control of microgrids. *IEEE Transactions on Smart Grid*, 8(3):1242–1251, 2017.

[65] Herong Gu, Deyu Wang, Hong Shen, Wei Zhao, and Xiaoqiang Guo. New power sharing control for inverter-dominated microgrid based on impedance match concept. *The Scientific World Journal*, 2013, 2013.

[66] Jianjun Su, Jieyun Zheng, Demin Cui, Xiaobo Li, Zhijian Hu, and Chengxue Zhang. An integrated control strategy adopting droop control with virtual inductance in microgrid. *Engineering*, 5(01):44, 2013.

[67] Jinwei He and Yun Wei Li. Analysis, design, and implementation of virtual impedance for power electronics interfaced distributed generation. *IEEE Transactions on Industry Applications*, 47(6):2525–2538, 2011.

[68] TL Vandoorn, JDM De Kooning, Bart Meersman, and Lieven Vandevelde. Improvement of active power sharing ratio of p/v droop controllers in low-voltage islanded microgrids. In *Power and Energy Society General Meeting (PES), 2013 IEEE*, pages 1–5. IEEE, 2013.

[69] Jinwei He, Yun Wei Li, Josep M Guerrero, Frede Blaabjerg, and Juan C Vasquez. An islanding microgrid power sharing approach using enhanced virtual impedance control scheme. *IEEE Transactions on Power Electronics*, 28(11):5272–5282, 2013.

[70] The national smart grid laboratory. `https://www.ntnu.edu/smartgrid`. Accessed: 2017-12-16.

[71] Zhikang Shuai, MO Shanglin, WANG Jun, Z John Shen, TIAN Wei, and FENG Yan. Droop control method for load share and voltage reg-

ulation in high-voltage microgrids. *Journal of Modern Power Systems and Clean Energy*, 4(1):76–86, 2016.

[72] SLS Lima, RFS Dias, and EH Watanabe. Indirect voltage control (ivc) versus direct voltage control (dvc) in distribution grids with renewable energy sources. In *Power Electronics for Distributed Generation Systems (PEDG), 2017 IEEE 8th International Symposium on*, pages 1–6. IEEE, 2017.

[73] Stephen Chapman. *Electric machinery fundamentals*. Tata McGraw-Hill Education, 2005.

[74] What is hardware-in-the-loop simulation? `https://se.mathworks.com/help/physmod/simscape/ug/what-is-hardware-in-the-loop-simulation.html`. Accessed: 2017-12-17.

[75] Robert H Park. Two-reaction theory of synchronous machines generalized method of analysis-part i. *Transactions of the American Institute of Electrical Engineers*, 48(3):716–727, 1929.

# A | Park Transform

In many applications the park transformation is very useful. When applied to control systems, the greatest advantage is to transform sinusoidal three-phase signals in the abc-frame into constant three-phase signals in the rotating dq0-frame. The transformation itself can be denoted by a matrix, T, as shown in (A.1) [75] [42].

$$T = \frac{2}{3} \cdot \begin{bmatrix} cos(\phi) & cos(\phi - \frac{2\pi}{3}) & cos(\phi - \frac{4\pi}{3}) \\ -sin(\phi) & -sin(\phi - \frac{2\pi}{3}) & -sin(\phi - \frac{4\pi}{3}) \\ \frac{1}{2} & \frac{1}{2} & \frac{1}{2} \end{bmatrix} \tag{A.1}$$

The dq0-coordinate system is rotating with a certain frequency. When used for voltage control, this frequency is normally equal to the frequency of the reference signal in the abc-frame. This makes the reference values, which are sinusoidal signals in the abc-frame, to be constant values when transformed to dq0-signals. In a balanced system, only the d- and q-component will be present, since the 0-component is representing an imbalance in the system. The angle $\phi$ represents the angle between the rotating and stationary coordinate systems. Normally, this is the angle between the d-axis in the rotating reference frame, and the a-axis in the stationary. A voltage and current signal can both be transformed to the dq0-frame by the transformation matrix in the same way, as shown in (A.2) and (A.3).

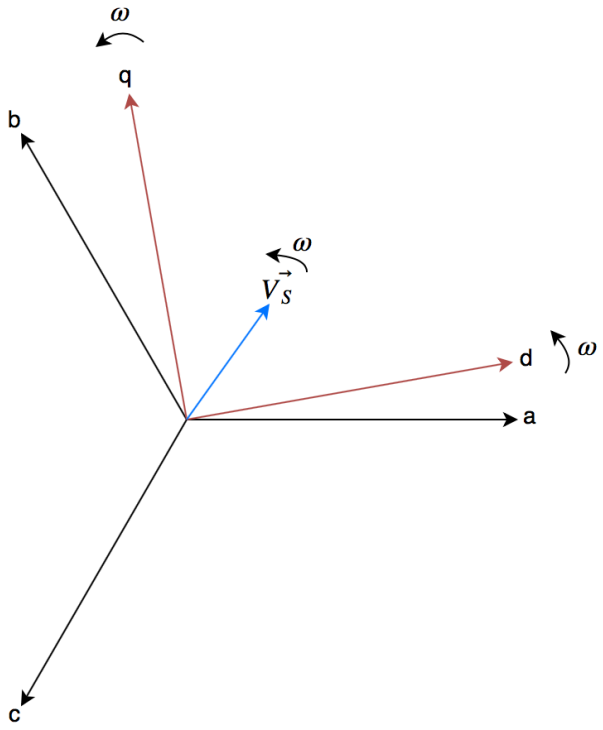


**Figure A.1:** The synchronous reference frame with frequency $\omega$

$$\begin{bmatrix} V_d \\ V_q \\ V_0 \end{bmatrix} = T \cdot \begin{bmatrix} V_a \\ V_b \\ V_c \end{bmatrix} \tag{A.2}$$

$$\begin{bmatrix} I_d \\ I_q \\ I_0 \end{bmatrix} = T \cdot \begin{bmatrix} I_a \\ I_b \\ I_c \end{bmatrix} \tag{A.3}$$

A graphical representation of a rotating dq reference system together with a abc-reference system is depicted in Fig. A.1. Here, the frequency of the synchronous reference frame is denoted as $\omega$, with the voltage vector $V_S$ rotating with the same frequency.

# B Transfer Functions for Low-Pass Filters

In this appendix, the transfer functions for the L-, LC- and LCL-filters are shown. The L-filters has a transfer function as shown in (B.1). Here, R denotes the internal resistor in the inductor, L. $i_{output}$ denotes the output current of the filter, and $v_{input}$ the input voltage level.

$$G_L = \frac{i_{output}}{v_{input}} = \frac{1}{sL + R} \tag{B.1}$$

The LC-filter has a transfer function as shown in (B.2). Here, the transfer function is a relation between the input- and output voltage, instead of the input voltage and output current, as for the L- and LCL-filter. A comparison between the transfer functions' bode-plot will however make it possible to see the difference in e.g. reasonant peak, as was done in Section 2.3. In (B.2), the notation is similar as for the L-filter. In addition to the parameters introduced for (B.1), $v_{output}$ is the output voltage across the capacitor, while $R_C$ is the resistance related to the capacitor, $C$.

$$G_{LC} = \frac{v_{output}}{v_{input}} = \frac{1 + R_C C s}{s^2 LC + sC(R_C + R) + 1} \tag{B.2}$$

The transfer function of the LCL-filter is shown in (B.4), where (B.3) defines the resonant frequency, $\omega_r$.

$$\omega_r = \sqrt{\frac{1}{L_1 C} + \frac{1}{L_2 C} + \frac{1}{L_1 L_2}(R_1 R_2 + R_1 R_C + R_2 R_C)} \tag{B.3}$$

$$\mathrm{G}_{LCL}(s) = \frac{i_{output}(s)}{v_{input}(s)} = \frac{sR_C C+1}{s^3 L_1 L_2 C + s^2(L_2 C(R_1+R_C)+L_1 C(R_2+R_C)) + L_1 L_2 C\omega_r^2 s) + R_1 + R_2} \tag{B.4}$$

$L_1$ and $L_2$ denote the inverter-side and grid-side inductor, respectively. $R_1$ and $R_2$ are the resistances related to these inductors. $i_{output}$ is the current flowing through the grid-side inductor.

# C | Matlab-Code for Bode Plots of LCL-Filters

```
close all;
clear all;
clc;
s = tf('s');

Rpu = 0.01;
V_base = 230*sqrt(2);
S_base = 5.7e3;
I_base = S_base/(1.5*V_base);
Z_base = V_base/I_base;
w_base = 2*pi*50;
L_base = Z_base/w_base;
C_base = 1/(Z_base*w_base);

C_filter = 50e-6;
L_filter = 500e-6;
L_filter_grid = 200e-6;
R_filter = Rpu*Z_base;
```

```
19
20 C_filter_pu = C_filter/C_base;
21 L_filter_pu = L_filter/L_base;
22 L_filter_grid_pu = L_filter_grid/L_base;
23 R_filter_pu = Rpu;
24
25
26 Rconst = Rpu*Z_base*Rpu*Z_base + Rpu*Z_base*Rpu*
       Z_base + Rpu*Z_base*Rpu*Z_base;
27
28 const1 = (Rpu*Z_base/L_filter + Rpu*Z_base/
       L_filter);
29 const2 = (Rpu*Z_base/L_filter_grid + Rpu*Z_base/
       L_filter_grid);
30
31 omegares = sqrt( (1/(L_filter*C_filter)) + (1/(
       L_filter_grid*C_filter)) + ((1/(L_filter_grid*
       L_filter))*Rconst));
32
33 G_lcl = ((s*Rpu*Z_base*C_filter) + 1) / ((s*
       L_filter*L_filter_grid*C_filter)*(s^2 + s*(
       const1 +const2) + omegares^2) + Rpu*Z_base +
       Rpu*Z_base);
34 G_lc = (1 + ((Rpu*Z_base)* C_filter*s))/ (1 +(2*(
       Rpu*Z_base)*C_filter*s)+ s^2*L_filter*C_filter)
       ;
35 G_l = 1/((Rpu*Z_base)+s*L_filter);
36
37 Rpu = 0;
```

```
38 G_lcl_noR =((s*Rpu*Z_base*C_filter) + 1) / ((s*
       L_filter*L_filter_grid*C_filter)*(s^2 + s*(
       const1 +const2) + omegares^2) + Rpu*Z_base +
       Rpu*Z_base);
39
40 bode(G_l);
41 hold on;
42 bode(G_lc);
43 bode(G_lcl);
44 legend('L-filter', 'LC-filter', 'LCL-filter');
45
46 figure;
47 bode(G_lcl);
48 hold on;
49 bode(G_lcl_noR);
50 legend('Included resistances', 'Omitted
       resistances')
51 title('');
```

# D | Additional Simulation Parameters

| Parameter | Symbol | Value |
|---|---|---|
| Assumed Switching Frequency | $f_{sw}$ | 15 kHz |
| Frequency Change | $\Delta f$ | 0.1 Hz |
| Voltage Change | $\Delta E$ | 2.3 V |
| Active Power Change | $P_{change}$ | 2.42 kW |
| Reactive Power Change | $Q_{change}$ | 1.50 kVAr |
| Reference Voltage Case 1 a) | $V_{ref,1a)}$ | 327.4 V |
| Reference Voltage Case 1 b) | $V_{ref,1b)}$ | 327.7 V |
| Reference Voltage Case 2 a) | $V_{ref,2a)}$ | 327.1 V |
| Reference Voltage Case 2 b) | $V_{ref,2b)}$ | 328.8 V |
| Reference Voltage Case 3 a) | $V_{ref,3a)}$ | 327.4 V |
| Reference Voltage Case 3 b) | $V_{ref,3b)}$ | 327.7 V |
| Reference Frequency | $\omega_{ref}$ | 314.16 rad/s |
| Cut Off Frequency Virtual Impedance | $\omega_{cutoff,V.I.}$ | 942.5 rad/s |
| Cut Off Frequency Droop Control | $\omega_{cutoff,droop}$ | 20 rad/s |

**Table D.1:** Parameters used to develop simulation parameters in the case studies

**Table D.2:** Base values used in the per-unit representation

| **Parameter** | Symbol | **Value** |
|---|---|---|
| Voltage Base | $V_{base}$ | 325.27 V |
| Power Base | $S_{base}$ | 5700 VA |
| Current Base | $I_{base}$ | 11.68 A |
| Impedance Base | $Z_{base}$ | 27.84 $\Omega$ |
| Inductance Base | $L_{base}$ | 88.64 mH |
| Capacitance Base | $C_{base}$ | 114.30 $\mu F$ |

# E Tuning of PI-Controllers

## E.1 Current Control

The tuning procedure of the current controller's PI-controller is done by the pole placement method, as described in section 3.3.4. The constants introduced in (E.1) are for the current control loop defined by (E.2) and (E.3)

$$G_{dominant} = \frac{c_1}{s + c_2} \tag{E.1}$$

$$c_1 = \frac{\omega_{base}}{L_{pu}} \tag{E.2}$$

$$c_2 = \frac{R_{pu}\omega_{base}}{L_{pu}} \tag{E.3}$$

By using these constants, (3.13) and (3.14) can be used to select the PI-controller's parameters. In order for the current controller to have a fast dynamic, but avoid noise from the switching frequency, the natural frequency is selected one decade smaller than the switching frequency, as shown in (E.4). The switching frequency, $f_{sw}$, is assumed to be 15 kHz.

$$\omega_{0,i} = \frac{w_{sw}}{10} = \frac{2\pi f_{sw}}{10} \tag{E.4}$$

## E.2 Voltage Control

Similarly as for the current controller, the voltage controller contains a PI-controller tuned by the use of pole placement. The parameters used here are decided on the basis of a natural frequency one decade lower than the current controller's natural frequency, as shown in (E.5). This to be sure that the difference in bandwidth between the two controllers are sufficiently large.

$$\omega_{0,v} = \frac{\omega_{0,i}}{10} = \frac{2\pi f_{sw}}{100} \tag{E.5}$$

The constants in (E.1) are given by (E.6) and (E.7) for the voltage controller.

$$c_1 = \frac{\omega_{base}}{C_{pu}} \tag{E.6}$$

$$c_2 = 0 \tag{E.7}$$

These constant are then used in (3.13) and (3.14) to decide the PI-controller's proportional and integrator gain.

# F | Bode Plots of Current- and Voltage Controllers

Bode plots showing the behavior of the current- and voltage controllers are shown in the following.

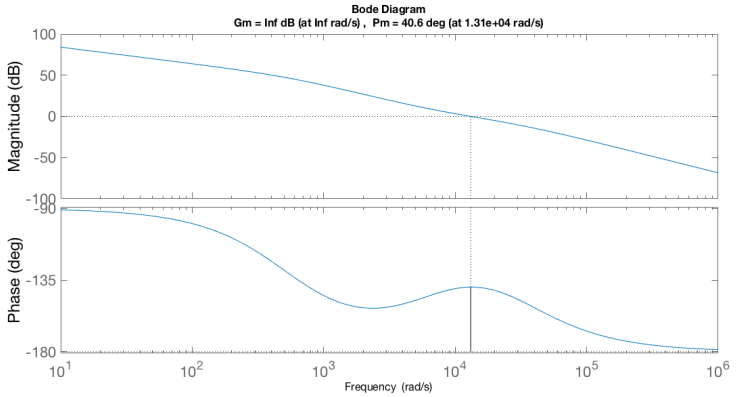


**Figure F.1:** Bode plot of the open current loop

Fig. F.1 and F.2 show bode plots for the open loop transfer functions for the current- and voltage control, respectively. This is the same assumptions done when the voltage controller was designed. The bode plots show that both the controllers have infinite gain margin. The phase margins are both above 40 °, which is seen as satisfying in this study [41, chapter 8].

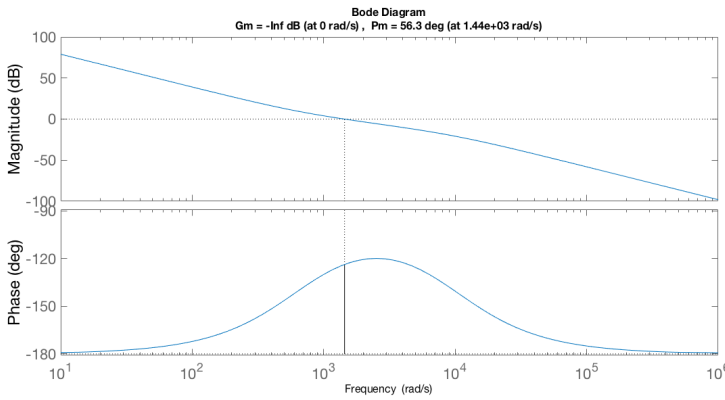


**Figure F.2:** Bode plot of the open voltage loop

# G | MATLAB-Code for Bode-Plots of Current- and Voltage Controllers

```
%Bode plots
close all;
clear all;
%%
Ts = 2e-5;
Tspwm = 2e-7;

w_ref = 2*pi*50;
Eref = 400*sqrt(2)/sqrt(3);

deltaf= 0.1;
deltaomega = deltaf*2*pi;
Sload = 5.7e3;
pf = 0.85;
Pload = Sload*pf;
Qload = sqrt(Sload^2 - Pload^2);
```

```
17 Snom = Sload;
18 Pnom = Snom*pf;
19 Qnom = sqrt(Snom^2 - Pnom^2);
20 deltaE = 23;
21
22 %%
23 %Conventional Droop
24 %m: P-f
25 %n: Q-V
26 m = deltaomega/(Pload/2);%/10;
27 n = deltaE/(Qload/2)/10;%/10;
28
29 %%
30 %Opposite droop
31 %m: for Q-f droop
32 %n: for P-V droop
33
34 m_opposite = deltaomega/(Qnom/2);
35 n_opposite = deltaE/(Pnom/2)/10;
36
37 %%
38 %Low-pass filter for power filtering
39 timeconstfilter = 0.05;
40
41 %Low-pass filter for virtual impedance
42 timeconstVI = 1/(50*3*2*pi);
43
44 %%
45 fsw = 15e3;
```

```
46 Rpu = 0.01;
47 rho = 0.7;
48 t_delay = 0.5*(1/fsw);
49 T_eq = 2*t_delay;
50 wsw = 2*pi*fsw;
51
52 V_base = 230*sqrt(2);
53 S_base = Snom;
54 I_base = S_base/(1.5*V_base);
55 Z_base = V_base/I_base;
56 w_base = 2*pi*50;
57 L_base = Z_base/w_base;
58 C_base = 1/(Z_base*w_base);
59
60 %%
61 %Filter Values
62 C_filter = 50e-6;
63 L_filter = 500e-6;
64 L_filter_grid = 200e-6;
65 R_filter_pu = 0.01;
66 R_filter = R_filter_pu*Z_base;
67
68 C_filter_pu = C_filter/C_base;
69 L_filter_pu = L_filter/L_base;
70 L_filter_grid_pu = L_filter_grid/L_base;
71 R_filter_pu = R_filter/Z_base;
72 %%
73 %current control
74 w_oi = wsw/10;
```

```
75 a = w_base*Rpu/L_filter_pu;
76 c = w_base /L_filter_pu;
77 %
78 K_pi = ((2*rho*w_oi)-a)/c;
79 K_ii = (w_oi)^2 / c;
80
81 %%
82 %Voltage control
83 w_ov = w_oi / 10;
84
85 K_pv = (2*rho*w_ov*C_filter_pu)/w_base;
86 K_iv = (w_ov*w_ov*C_filter_pu)/w_base;
87 %%
88 fsw = 15e3;
89 Lpu = L_filter_pu;
90 Rpu = R_filter_pu;
91 Cpu = C_filter_pu;
92 wbase = 2*pi*50;
93 s = tf('s');
94 t_delay = 0.5/fsw;
95 rho = 0.7;
96 %%
97 %Current controller
98 Gphysicali = (1/Rpu)/(1+(Lpu/(Rpu*wbase)*s));
99 GPWMi = 1/(1+t_delay*s);
100 GPIi = K_pi + K_ii/s;
101
102 Goli = GPIi*GPWMi*Gphysicali;
103 Gcli = Goli / (1+Goli);
```

```
104 figure(1);
105 margin(Goli);
106
107 %%
108 delaycurrent = 1/w_oi;
109 Gdelaycurrent = 1/(1 + delaycurrent*s);
110 %Voltage Controller
111 Gphysicalv = wbase/(s*Cpu);
112 GPIv = K_pv + K_iv/s;
113 Golv = Gphysicalv*GPIv*Gdelaycurrent;
114 Gclv = Golv / (1+Golv);
115
116 figure(2);
117 margin(Golv);
```

# H | Response of the Controllers

In the following, the behavior of the current- and voltage controller will be shown, in addition to both of the droop controllers. The simulations for generating these plots are utilized in a microgrid system without use of virtual impedance.

Figure H.1 and H.2 show how the conventional and the opposite droop controllers follow their reference for one inverter. The figures also show that the conventional droop controller have an accurate active power response, while the reactive power is inaccurate. This causes the poor reactive power sharing mentioned in Chapter 4. A similar behavior is shown for the opposite droop control, but this controller provides accurate reactive power dispatch, while there is a significant error in the active power. By Fig. H.1 and H.2, it can be seen that the control speed of the two droop controllers provide a similar control speed, with a stable response after around 0.3 s.

The voltage controller's response is shown in Fig. H.3. The control speed is much faster than for the droop controllers. An accurate response is provided, both for the d- and q-axis components, where there is a maximum overshoot of around 0.2 pu. The voltage level is relatively stable after 0.1 s, so around three times faster than the outer power control provided by the droop controllers.

The current controller's response is shown in Fig. H.4. The current reference in this figure is not constant, since the reference is given by the

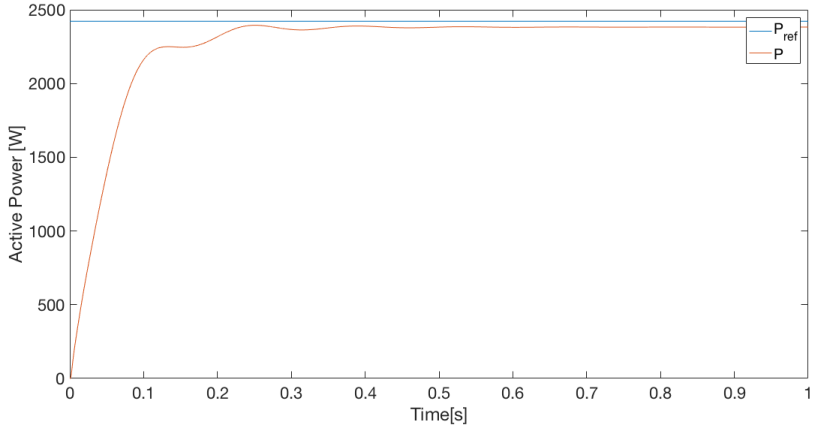


(a) Active Power

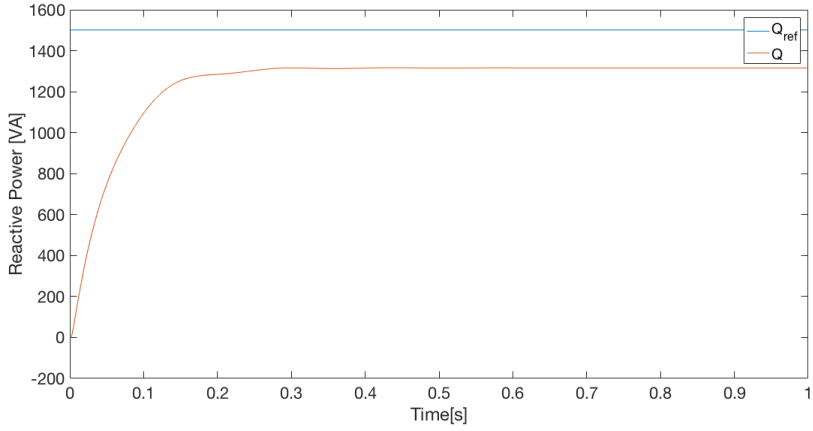


(b) Reactive Power

**Figure H.1:** Response of the conventional droop controller

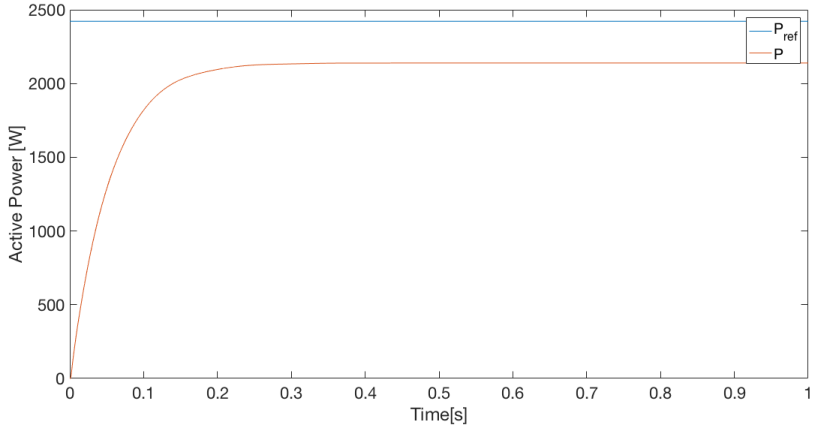


(a) Active Power

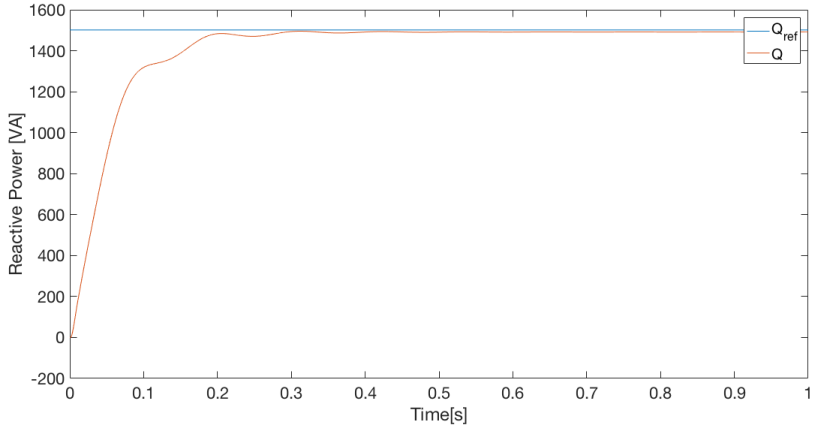


(b) Reactive Power

**Figure H.2:** Response of the opposite droop controller

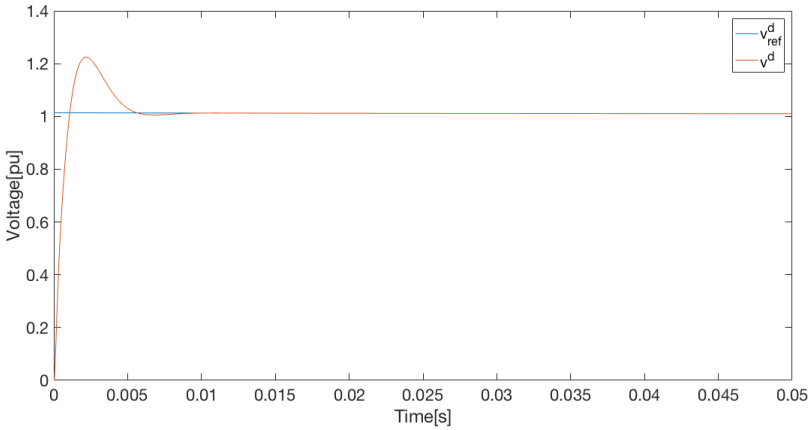


(a) d-axis

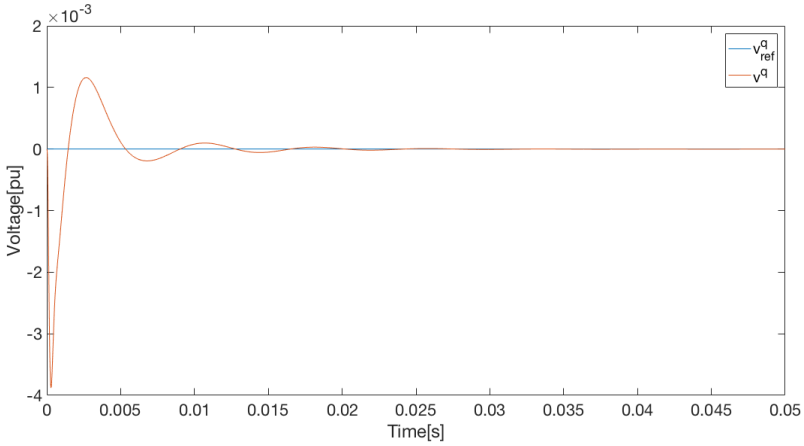


(b) q-axis

**Figure H.3:** Response of the voltage controller

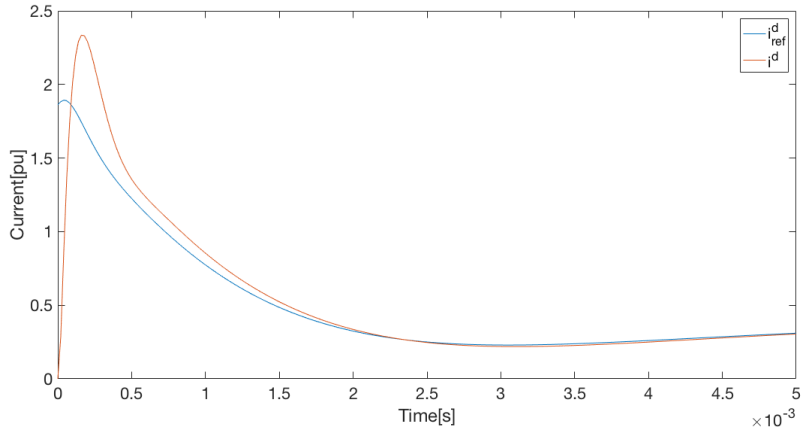


(a) d-axis

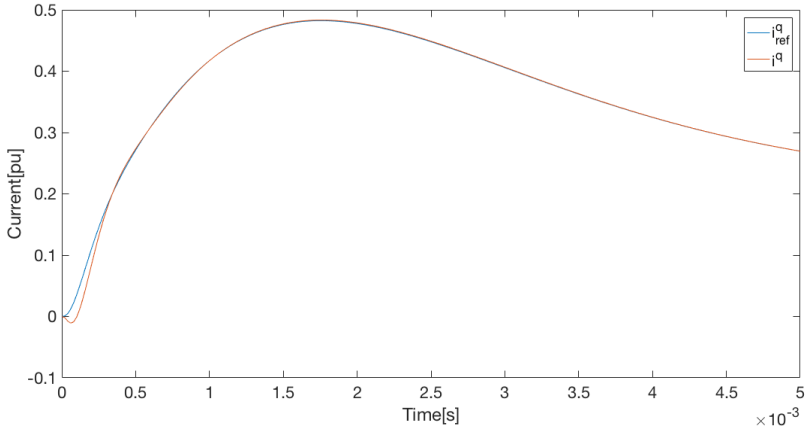


(b) q-axis

**Figure H.4:** Response of the current controller

slower voltage- and power control. The current control speed is much faster than the two other controllers, where the output current follows the reference signal relatively close at around 1.5 ms. Since the parameters are chosen so the controller should be 10 times faster than the voltage control, this is seen as reasonable. With a not-constant current reference, the control is more challenging, causing a slower response.

# I Simulink Models

## I.1 Microgrid Model

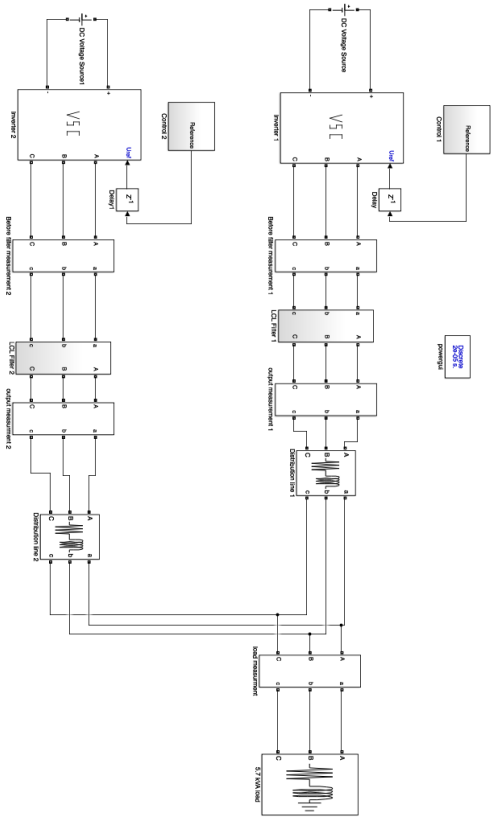

# I.2 Current Controller

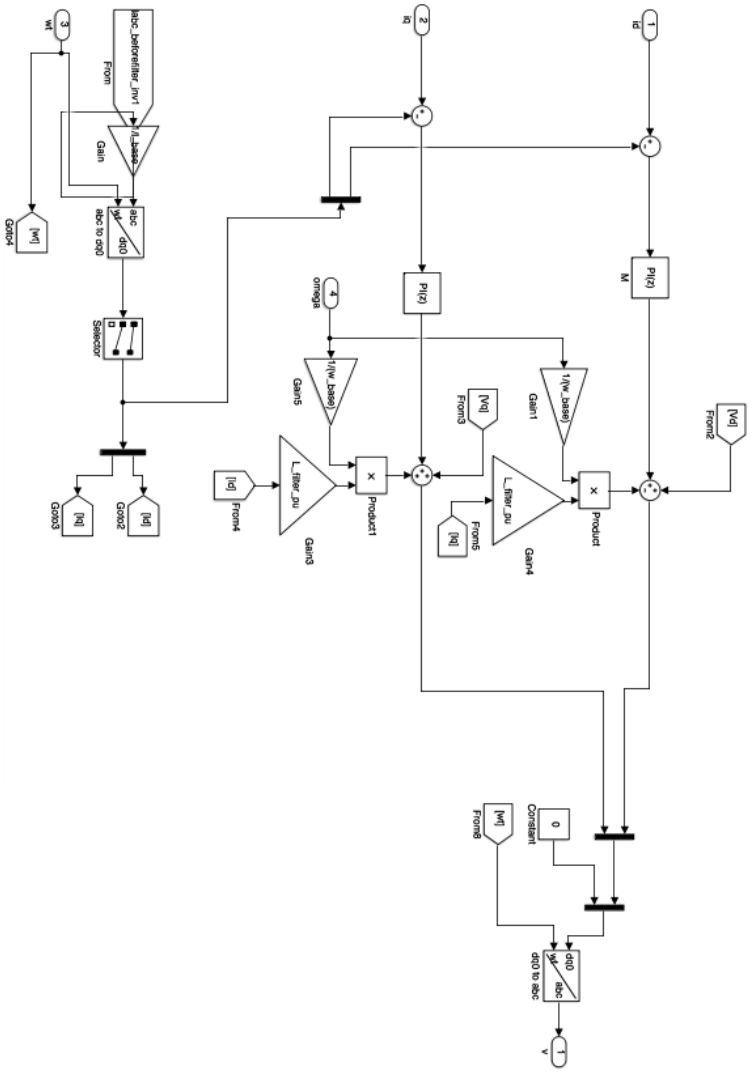

# I.3 Voltage Controller

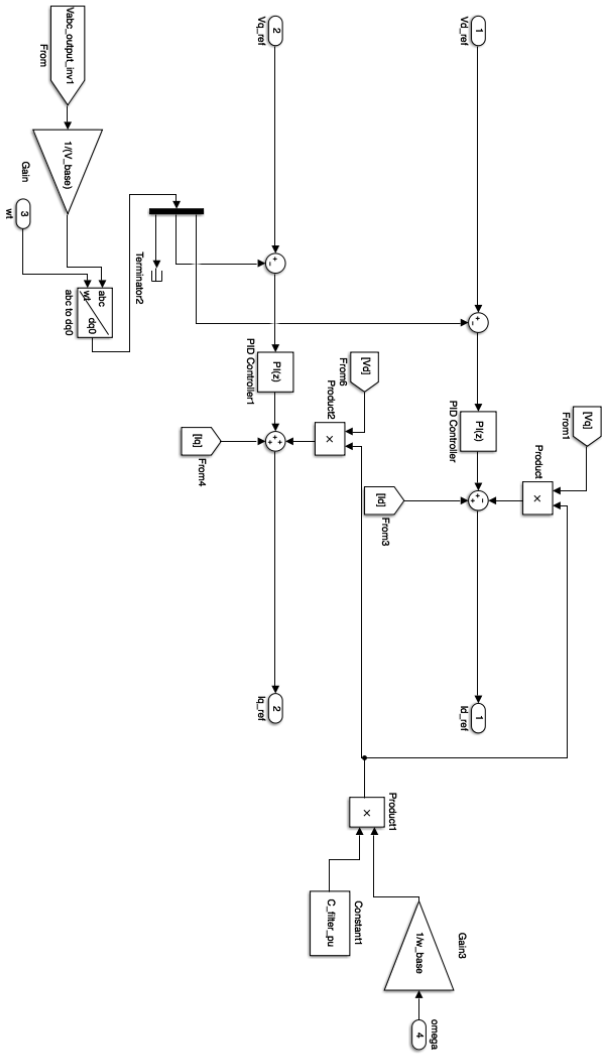

# I.4 Conventional Droop Controller

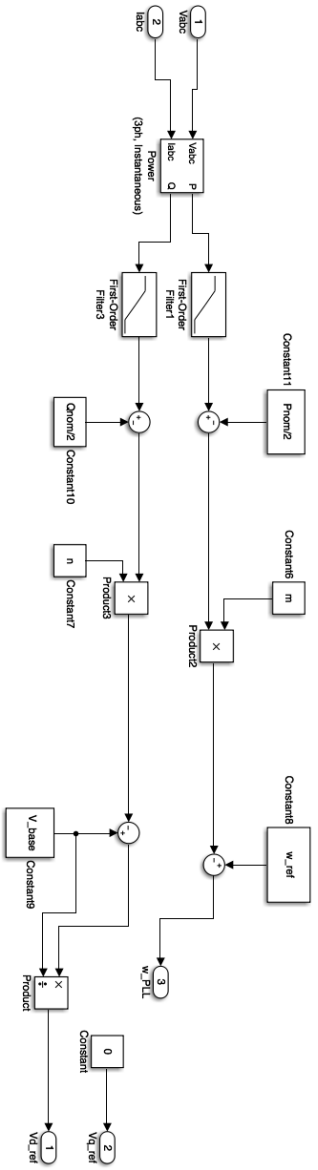

# I.5 Opposite Droop Controller

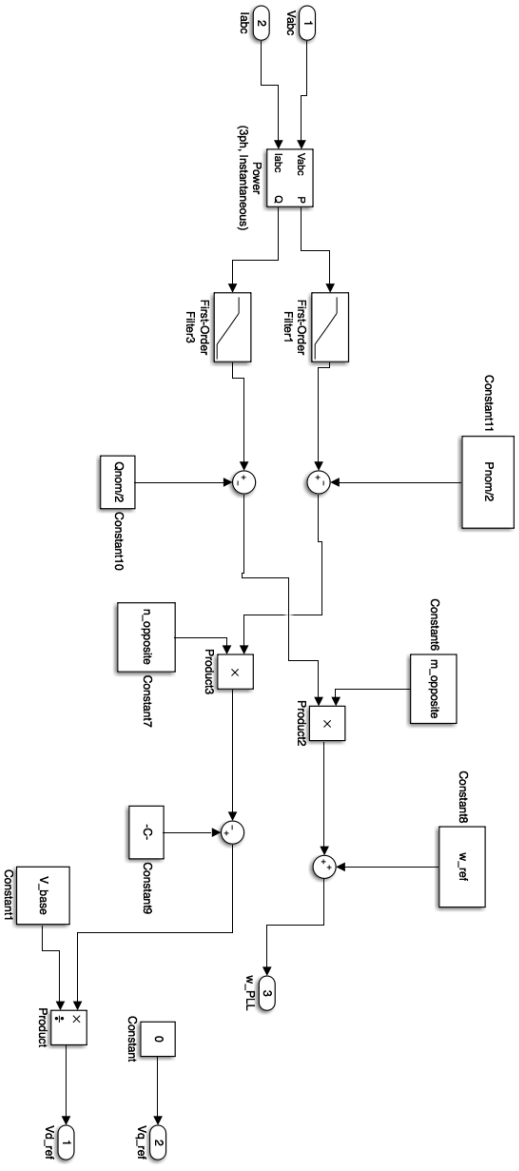

# I.6 Virtual Impedance

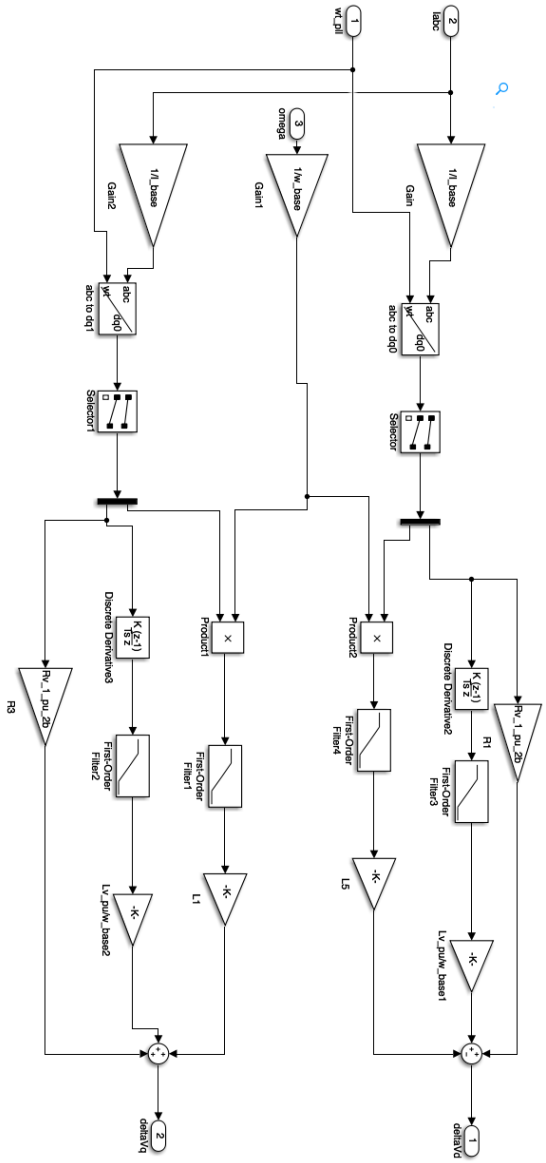

# J Chapter 2 from "Control of Power Electronics in Microgrids"

# 2 | Literature Review

## 2.1 Microgrids

### 2.1.1 Definition

A microgrid is defined as a distribution system including distributed energy resources (DER), energy storage systems (ESS) and flexible loads [2, chapter 1]. It has clearly defined electrical boundaries, and from the main grid, the microgrid should be controllable as a single unit. It has two main operation modes. These are the grid connected mode and "island mode", where the microgrid is disconnected from the main grid. This capability is a strong feature, and advantageous when it comes to securing the electricity supply in the grid [9].

### 2.1.2 Fundamental components

In the operation of a microgrid, there are a number of essential controllable components. With a large amount of unreliable distributed generation, the voltage and power levels from this generation and the energy storage need to be controlled. When operating in grid-connected mode, there has to be a proper interaction with the main grid [14].

A lot of the distributed generation, e.g. a PV-system and also a battery storage device, are based on DC [15, chapter 6]. When connected to a DC-microgrid, a DC/DC-converter is used to convert the voltage level, while in a AC-microgrid, an DC/AC-inverter is used to convert the voltage to a proper AC-voltage [16, chapter 8].

In the following sections, some of the main components of a microgrid will be introduced.

#### Distributed Generation

One of the things that characterize a microgrid, is the use of distributed generation [9] [2, chapter 1]. In contrast to large generation units in the traditional power

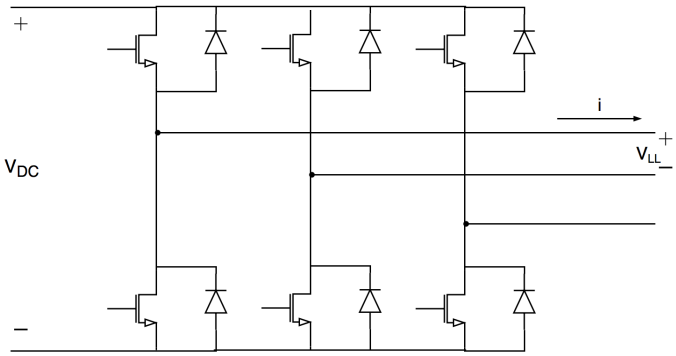


**Figure 2.1:** A schematic showing a voltage source converter

grid, the DGs are normally much smaller, also in terms of power [17]. A lot of the DGs are based on renewable energy resources, which makes them particularly important because of their importance in the future power grid [7].

DG, such as PV-systems and wind-turbines, are clearly dependent on the weather. With less reliable generation, the need for ESSs increases for the required power to be supplied [18]. In contrast to traditional rotating generators, many of the DGs do not have any rotating mass [19]. This leads to challenges when it comes to frequency regulation, as will be further discussed in section 2.2. In section 2.1.7, challenges related to the interaction between several DGs will be studied.

### Voltage Source Converter

Many of the technologies used for DG are based on DC-voltage [15, chapter 6] [15, chapter 8]. In the process of converting a DC-voltage to a three-phase AC-voltage, or opposite, a three-phase voltage source converter (VSC) can be used [17]. A schematic is shown in Fig. 2.1. When the power flow is from the DC to the AC side, the converter operates as an inverter. The output of a three-phase voltage source inverter (VSI) is decided by the input DC-voltage and the operating of the semiconducting devices, acting as switches. A frequently used method to create control signals for VSCs is the pulse width modulation method [16, chapter 8]. A comparison between the reference output waveform and a high-frequency triangular waveform is then used to generate a control signal for the semiconducting devices.

When the power flow can be bidirectional, for example in case of a battery, the VSC has to be able to operate both as an inverter and a rectifier [16]. In this work, the operation of the VSCs are limited to inverter operation.

### Energy Storage System

The ESS can store surplus energy from DGs, and at times with lower generation, it can assist the DGs and the main grid with the power supply [15, chapter 9]. By balancing the difference between production and load, it also helps stabilizing the voltage and frequency in a microgrid, especially in island mode operation [20]. The total storage capacity of a microgrid can consist of one large ESS, or several smaller units, where the total capacity of the microgrid can contribute to decide how long the it can operate in island mode [15, chapter 9]. Electrical vehicles's (EV's) battery can also contribute to the energy storage capacity of the microgrid, through a vehicle-to-grid-solution [21] [11]. For the ESSs, several technologies are available. Examples of common alternatives are flywheel energy storage (FES), supercapacitors and batteries, which will briefly introduced in the following.

In a flywheel energy storage, kinetic energy are stored in a rotating system. By using an electric machine, the flywheel is accelerated, while the flywheel is decelerated when electricity is generated from it. Normally, FESs are used for relatively short time energy storage.[22][23].

A supercapacitor is a large capacitor where the energy is stored as static charge. They are also best suited for applications where short-term charging is needed. Both supercapacitors and FES systems have long lifetime, including many cycling times without much maintenance [23].

Battery Energy Storage (BES) systems are probably the most used energy storage alternative among these, and one of the most used technologies on the market [23]. The energy is stored as electrochemical energy, with several technologies available. Many of these technologies can be used for long term storage, but the capability for number of cycling times can be a drawback compared to the other alternatives [22].

### Loads

The loads connected to a microgrid will have great influence on the electrical parameters, such as current and voltage levels. With more power electronics, the amount of non-linear loads in the power grid will increase [16, chapter 5]. These load also make strict demands on the microgrids control system, in order to keep the electrical parameters within required boundaries [2, chapter 2].

Also, the number of controllable loads can be increased. An example is the electrical vehicles, as already mentioned. They can operate not only as loads, but also as a part of the storage capacity of the grid. Then, a control system must be connected to ensure the charging, as well as controlling the possible reverse power flow.

#### Control System

A microgrid consists of several control systems to achieve satisfying voltage and frequency levels, proper power control and to avoid instability and harmonics. The different levels of control are elaborated in section 2.1.7.

### 2.1.3 Modes of operation

Microgrids are mainly connected to the main grid through one point, often referred to as point of common coupling (PCC) [24]. One of the microgrids main features are their ability to operate in both grid-connected and island mode. This can help securing electricity supply in emergency situations or at times when the main grid is stressed, since the islanded mode can be both intended or caused by an electric fault.

In grid connected mode, the microgrid can both import and export energy, causing a bidirectional power flow through the PCC. This is advantageous, and can be utilized through distributed generation and controllable loads in the microgrid. In addition, the bidirectional power flow causes some challenges, which will be further discussed in section 2.1.6.

When switching from island- to grid-connected mode, the voltage, frequency and phase angle has to be synchronized in order to reduce transient effect. This makes strong requirements to the control system. After a connection, the voltage and frequency in the microgrid will be strictly decided by the main grid's electrical parameters.

When a microgrid is operating in island mode, it has a higher relative load change, and the total inertia of the system is much smaller than in a grid-connected case. These two factors will cause larger voltage and frequency deviations without a well designed control system. The difference between the two modes of operation makes it challenging to design a control system which works well for both modes. In [14], a control strategy for DERs is proposed, independent if they are grid-connected or islanded.

### 2.1.4 Energy Demand Management

Energy Demand Management, also referred to as demand side integration, is a way to manipulate the energy use of the consumers [2, chapter 1] [25]. The control of the load can be divided into two broad categories: Manual or automated control. With the manual approach, the control is done by informing the customers about e.g. prices. By increasing the cost of electricity during peak-hours, the customer will reduce their electricity use by their own. The automated control is done by

shifting loads automatically, where the shifting is based on predefined considerations.

In the automated energy demand management, energy storage devices play an important role. During peak-hours, a larger amount of power can be supplied from the batteries, to reduce the main grid's stress. This is done by a concept often referred to as "peak shaving and valley filling" [15, chapter 9]. The ESS is charged when the load is low, to supply energy at higher-load hours, where the deviation between the DERs production and the total load of the system is the largest. Controllable, flexible loads can also contribute to a good energy demand management, for instance by specifying when an EV should be fully charged. As long as this is met, the battery of the EV can contribute to the grid, as described in previously.

### 2.1.5 Ancillary Services

Since microgrids behave as a single unit from the main grid, they have the ability to provide several ancillary services. They can offer services such as energy demand management, supply of reactive power and contribution to voltage and frequency regulation. These features are powerful attributes of microgrids, where many of them are dependent of the ESS.

### 2.1.6 Technical Challenges

The operation of a microgrid has several technical challenges, compared to the operation of the large power grid. Some of the main challenges can be classified as follows [17].

1. Stability and Power Quality: Many generation units, loads and control systems can cause disturbances. This can affect both the power quality and stability.

2. Protection: More DG also leads to power flow issues such as circulating currents and problems connected to bidirectional power flows. The protection challenges increases, including voltage and frequency control and fault currents for instance.

3. Low Moment of Inertia: With more inverter-based generation, the amount of rotating mass in the system will decrease. This can lead to large frequency deviations, especially when operting in island mode.

4. Uncertainty: More DG based on RES can cause larger reliability issues, since many of the generation units will be non-controllable.

Section 2.2, 2.3 and 2.4 will present solutions for power quality, low inertia and power flow challenges in microgrids. These solutions are based on proper control of power electronics.

### Circulating Current

One of the challenges of particular interest in this work, is the circulating current. The definition of the circulating current, considering one phase, is given in (2.1) [12]. Here, $c_i$ denotes the circulating current from inverter number i. The relative load delivered from the inverters are given as h, where the sum of them are 1. The total number of inverters are given by n.

$$c_i = \sum_{m=1}^{n} (h_m i_i - h_i i_m) \tag{2.1}$$

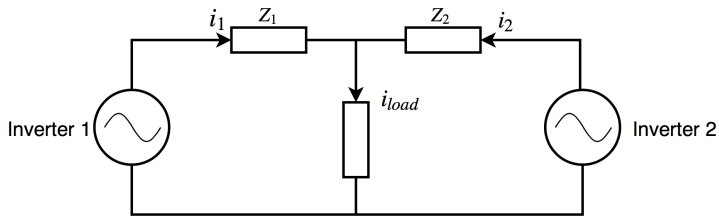


**Figure 2.2:** Two inverters with different line impedance, delivering power to the same load

Figure 2.2 shows a simplified per-phase diagram showing two inverters feeding one load. The line impedances are given as $Z_1$ and $Z_2$, and a difference between these can cause a circulating current. By using (2.1), the circulating current, which causes losses, instability and protection challenges, can be found. It also complicates the power sharing in a system [26].

## 2.1.7 Control

A common approach for controlling microgrids, is by using a hierarchical control structure. As presented in [27], a common way is to divide the control into four different levels, labeled from zero to three. The control speed decreases with increasing level, where level zero is the fastest control loop [17].

The inner control loops are level zero, which include the local control for each device, necessary to keep the system stable. This includes the inverter's current

and voltage control. Level one, the primary control, focuses on the microgrid as a whole. These systems make sure multiple paralleled inverters work together in a sufficient way. Examples on control mechanism used on this level are conventional and opposite droop control.

The secondary and tertiary control represent the two uppermost levels. The secondary control secures that the electrical levels are within certain limits. It can also make sure that the microgrid is synchronized with the main grid. Tertiary control is present in case of a grid-connected microgrid. This level controls the exchange of energy between the main grid and the microgrid.

There are often several inverters operating in parallel in a microgrid. The control of the interaction between these and the rest of the microgrid can in general be divided into centralized control, master slave control and decentralized control [28]. The decentralized control can again be divided into decentralized control with or without communication lines.

Each of these control priciples have their advantages and disadvantages, but in this work, it will be focused on the decentralized control without communication lines, and in particular droop control.

### Park Transform

In many applications the park transformation is very useful. When applied to control systems, the greatest advantage is to make sinusoidal three-phase signal in the abc-frame into a constant three-phase signal in the rotating dq0-frame. The transformation itself can be denoted by a matrix, T, as shown in (2.2) [29] [30].

$$T = \frac{2}{3} \cdot \begin{bmatrix} cos(\phi) & cos(\phi - \frac{2\pi}{3}) & cos(\phi - \frac{4\pi}{3}) \\ -sin(\phi) & -sin(\phi - \frac{2\pi}{3}) & -sin(\phi - \frac{4\pi}{3}) \\ \frac{1}{2} & \frac{1}{2} & \frac{1}{2} \end{bmatrix} \tag{2.2}$$

The dq0-coordinate system is rotating with a certain frequency. When used for voltage control, this frequency is normally equal to the frequency of the reference signal in the abc-frame. This makes the reference values, which are sinusoidal signals in the abc-frame, to be constant values when transformed to dq0-signals. In a balanced system, only the d- and q-component will be present, since the 0-component is representing an imbalance in the system. The angle $\phi$ represents the angle between the rotating and stationary coordinate systems. Normally, this is the angle between the d-axis in the rotating reference frame, and the a-axis in the stationary. A voltage and current signal can both be transformed to the dq0-frame by the transformation matrix in the same way, as shown in (2.3) and (2.4).

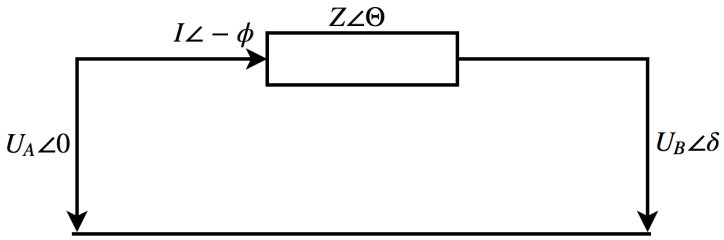


**Figure 2.3:** A representation of power flow through a line

$$\begin{bmatrix} V_d \\ V_q \\ V_0 \end{bmatrix} = T \cdot \begin{bmatrix} V_a \\ V_b \\ V_c \end{bmatrix} \tag{2.3}$$

$$\begin{bmatrix} I_d \\ I_q \\ I_0 \end{bmatrix} = T \cdot \begin{bmatrix} I_a \\ I_b \\ I_c \end{bmatrix} \tag{2.4}$$

### Droop Control

Droop control is a distributed control algorithm where the power flow is controlled without need for communication between the inverters [6, chapter 9] [28]. The principle is based on the relation between the active and reactive power flow, and the frequency and voltage in the grid.

By studying the power flow through a line, as shown in Fig. 2.3, the droop control principle can be explained. With a line impedance represented by Z, the active and reactive power flow in the line is given by (2.5) and (2.6) [28] [31]. Here, $\delta$ represents the power angle, while $\Theta$ is the angle of the impedance, Z. If a small $\delta$ is assumed, $sin(\delta) \simeq \delta$ and $cos(\delta) \simeq 1$. By using these simplifications, $\delta$ can be expressed by (2.7), and the voltage drop by (2.8) [28] [32].

$$P = \frac{U_1^2}{Z} cos(\Theta) - \frac{U_1 U_2}{Z} cos(\Theta + \delta) \tag{2.5}$$

$$Q = \frac{U_1^2}{Z} sin(\Theta) - \frac{U_1 U_2}{Z} sin(\Theta + \delta) \tag{2.6}$$

$$\delta \simeq \frac{XP}{U_1 U_2} \tag{2.7}$$

$$U_1 - U_2 \simeq \frac{XQ}{U_1} \tag{2.8}$$

By (2.7) and (2.8), the conventional droop characteristic is found, represented by (2.9) and (2.10) [17]. Here, $m_P$ and $n_Q$ are the active and reactive droop coefficients. They decide the relation between frequency and active power, and voltage and reactive power, respectively. $E_{ref}$ and $\omega_{ref}$ are the rated voltage and frequency, while $P_{ref}$ and $Q_{ref}$ are the set points for the active and reactive power [28]. E, $\omega$, P and Q are the measured values of the voltage, frequency and active and reactive power. The conventional droop characteristic is summarized in Fig. 2.4 [17].

In a pure reactive line the power angle, $\delta$, is dependent on the active power, while the voltage drop on the reactive power. Therefore, the power angle can be controlled by the active power fed into the line. Because of the relation between the power angle and frequency [33, chapter 4.3.3], the active power fed into the line can be controlled by the frequency deviations. The reactive power is controlled by voltage fluctuations. This is the conventional droop control method[34] [28].

The droop coefficients $m_P$ and $n_P$ represent the change in frequency and voltage amplitude relative to power. In the equations used in this work, the values of $m$ and $n$ are always positive, they denote the absolute value of the slope in Fig. 2.4 and 2.5. The transient responses in the microgrid can be controlled by these coefficients. In section 2.2, it is studied how the inverters behaviour can imitate the behaviour of a synchronous machine when using the conventional droop control. These coefficients can also be customized to make different DGs feed the load differently [34].

$$\omega - \omega_{ref} = m_P(P_{ref} - P) \tag{2.9}$$

$$E - E_{ref} = n_Q(Q_{ref} - Q) \tag{2.10}$$

In a purely resistive line, a similar correlation can be found. By (2.5) and (2.6), and still assuming that $\delta$ is small, (2.11) and (2.12) can be derived.

$$\delta \simeq -\frac{RQ}{U_1 U_2} \tag{2.11}$$

$$U_1 - U_2 \simeq \frac{RP}{U_1} \tag{2.12}$$

As it can be seen from these equations, the power angle, and therefore frequency, is now dependent on the reactive power, while the voltage drop depends

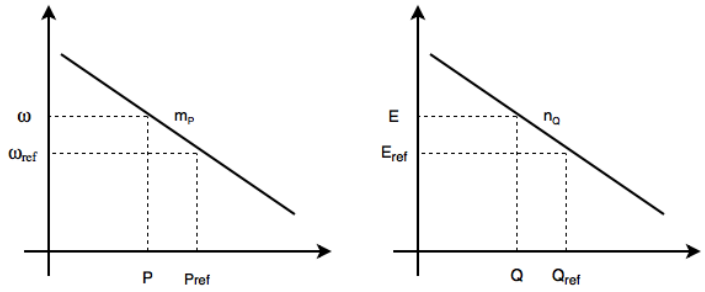


**Figure 2.4:** The characteristic of the conventional droop control

on the active power[28] [35]. This situation is often referred to as opposite droop [34].

In a low-voltage microgrid, the line impedance is normally mixed inductive and resistive, with a dominating resistive term. For this reason, an opposite droop is often a good choice for this type of grid. With a line impedance where neither the inductive or resistive term can be neglected, a coupling between the active and reactive power is present. This means that they cannot be controlled independently [18]. This form the basis for new solutions, including the use of virtual impedances, which will be discussed in section 2.4.

$$\omega - \omega_{ref} = m_Q(Q - Q_{ref}) \tag{2.13}$$

$$E - E_{ref} = n_P(P_{ref} - P) \tag{2.14}$$

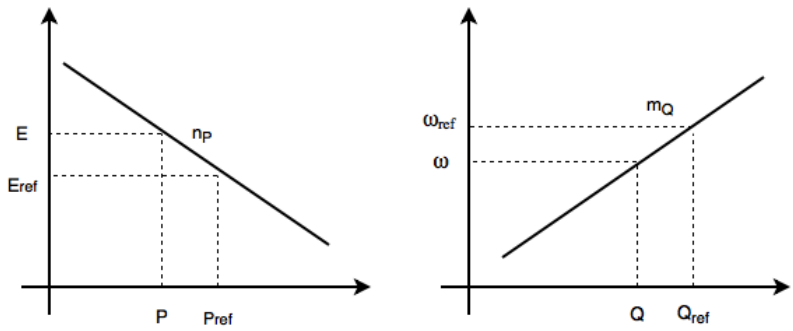


**Figure 2.5:** The characteristic of the opposite droop control

One of the greatest advantages of droop control is its lack of communication, which possibly can lead to significant reductions in costs [2, chapter 3]. Since the

control is located at each inverter, and each unit will adapt to the entire system, it is well suited for expansions in the grid. The reliability is high, and it can be applied for generation of different power ratings. The similarity between the behaviour of the conventional droop control and a synchronous machine is also an advantage, which will be further discussed.

Unfortunately, the method also has significant drawbacks, as discussed in [36]. This includes a slow transient response and poor harmonic sharing between non-linear loads. It is not well suited for RESs, due to their continuous changes in production. The conventional droop control is based on a line impedance which is inductive dominant, while the theory behind the opposite droop control assumes a dominating resistive component in the line impedance. In a real line, a coupling between the active and reactive power will often be present.

If two inverters feed the same load, but with different line impedances, the conventional droop control will give unequal reactive power sharing, while the opposite droop will give different active power flow. This is due to the power flows relation to the voltage drop in the two different techniques [34]. There are many proposed solutions, as presented in [36].

In this work, the effect of the droop coefficients are considered. The voltage and frequency deviations related to the power change will therefore be studied in detail.

### Improved Droop Control

Since active and reactive power normally are coupled, droop control algorithms with improved behaviour under these conditions are desired. In [28], an improved droop control method is suggested. An imaginary active and reactive power are found, dependent on the transmission lines R/X-ratio. These powers are called modified active and reactive power. The conventional droop control method can be used to control the frequency and voltage level independently. The frequency is then dependent of the modified active power, while the voltage of the modified reactive power.

[28] also suggests a droop control algorithm which instead of the modified active and reactive power, is based on a modified active and reactive current. This method has an advantage compared to the modified power method when the voltage is far from its rated voltage.

## 2.2 Virtual Synchronous Machine

In a traditional grid with large synchronous generators, the frequency in the grid are held relatively stable due to their large moment of inertia. Microgrids, dominated by inverter-based DGs, does not have this stabilizing inertia, since inverter-based generation have low, or zero rotating inertia [19]. Therefore, rapid load changes can possibly cause much larger deviation in frequency.

A solution which makes the inverter-based DGs act more like large synchronous generators, is the method called virtual synchronous machines (VSG), also frequently called virtual inertia. By control systems, DGs together with ESSs behave similar as synchronous machines [37] [19]. The virtual inertia of the system can be adapted to the operation at different times, and even the non-physical concept of negative inertia can be applied to the system.

The virtual synchronous machines can be used for balancing the power, and thus frequency, to limit the voltage during short circuit faults [38] [19], and improve the rotor angle stability in power systems [39]. In this work, the focus is mainly on the frequency and power regulation.

In [40], the method of VSG is used in a droop controlled microgrid to improve the transient response. By changing the droop coefficients, which is implemented in the controller, a virtual inertia is applied to the system. A change in the active power load will cause different frequency deviation based on the droop coefficient, in the same way as an inertia in the system will relate to how fast the frequency of the system is changing because of a load change.

When an energy storage unit starts injecting power into a grid due to a difference in the power generated and the power required from the loads, the starting time of the power exchange is important. If it takes too long before an energy exchange is present, frequency deviations in the grid can be so large that loads are disconnected due to safety[19]. Threshold values are therefore set, both in frequency deviation and rate of frequency change.

A general control scheme for the control of a VSG is shown in Fig. 2.6 [19]. In this figure, the VSG algorithm calculates the need of virtual rotational inertia, based on the frequency deviation and the rate of frequency change compared with the predefined threshold values.

### 2.2.1 Challenges

The operation of VSGs can be challenging in a grid containing both VSGs and traditional SGs. A coordination between them is needed [19]. The VSGs have a limited storage capacity, thus, the traditional SGs should eventually change their production to get rid of the difference between generation and load. Since the deviations in frequency normally brings a change in production by the SGs, this

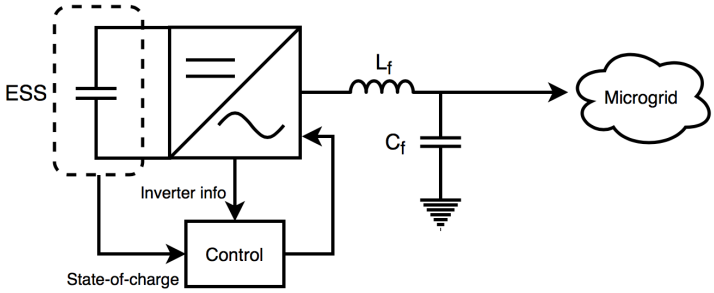


**Figure 2.6:** General control scheme for virtual synchronous machine

change will not happen when VSGs take care of the rapid frequency changes. Due to this, a coordination between the VSGs and SGs operating in the same grid is necessary.

## 2.3 Active Filtering

Power electronics devices provide several efficient services to the future electricity grid, but they also contribute to more non-linear loads in the system. These loads lead to harmonic and reactive currents [41]. Passive filters can be used for filtering harmonics, but have drawbacks such as large size, resonance and fixed compensation. Instead of these, power electronic devices can be used to compensate for harmonics. Such devices used to increase the power quality is known as active filters (AFs), where for instance voltage source converters can be used. This technique gives an improved filtering, but at a higher cost than passive filters.

To improve the power quality, AFs can provide voltage regulation, filtering harmonics, reactive power control and power factor correction[42] [43]. AFs can be implemented both as series active filters, shunt active filters, as shown in Fig. 2.8 and 2.7. An AF can also be a combination of the two, often called a power quality conditioner [44].

The shunt AF is the most used of the active filtering techniques. Harmonic currents are fed by the filter to compensate for the harmonic currents flowing in the line. An advantage of this technique is that the AF only has to be designed for a relatively small current, the harmonic compensating current. Figure 2.7 shows a basic illustration of the shunt AF in a grid.

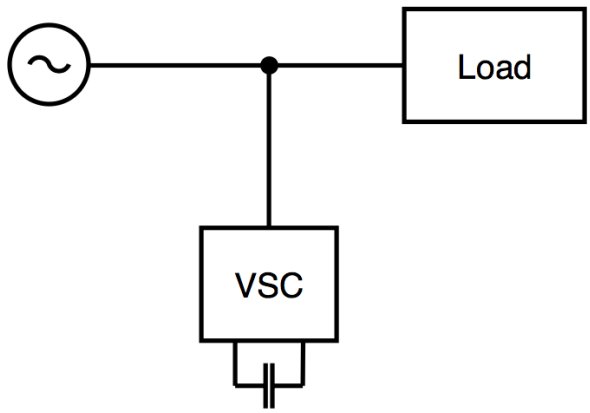


**Figure 2.7:** A basic diagram showing a shunt active filter

Instead of current harmonics, series AFs cancel voltage harmonics. As shown in Fig. 2.8, it can be done by using a transformer, connected in series with the line. A drawback of this method is that the series AF has to carry the entire load current. The current ratings of these filters must therefore be much larger than for the shunt

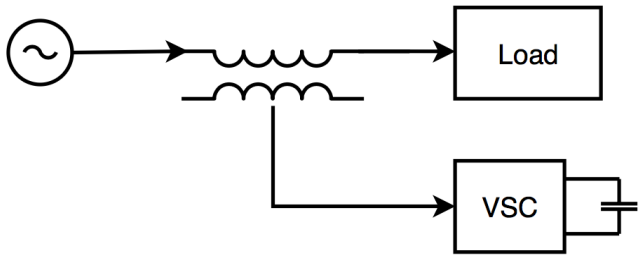


**Figure 2.8:** A basic diagram showing a series active filter

AFs, which makes the shunt alternative more common. The series alternative is used in applications that are voltage sensitive, and therefore need a high-quality voltage. It is also possible to combine active and passive filters. This configuration is called a hybrid filter [41] [45] [42], where either the series or shunt alternative can be used in combination with the passive filter.

## 2.4 Virtual Impedance

In a power grid with multiple DG units located in the grid, the power sharing between the different units can be challenging. The concept of virtual impedance is a control mechanism which is frequently used for this purpose, often in combination with droop control [46] [47].

In addition to power sharing, virtual impedances can be used in converter control for applications such as harmonic compensation and increased stability [48]. In the same paper, the concept is divided into two categories: Inner- and outer virtual impedance. Inner virtual impedance-loops are used for harmonic compensations and current limiting, and the signal from the loop is applied at the PWM. Harmonic voltage compensation, control of power flow, mitigation of unbalanced voltage and sharing between nonlinear loads in a power system is done by the use of outer virtual impedance, which modifies the reference signal of the controller.

These two categories of virtual impedances are both used to shape the output impedance of the converter. Because of its many applications, the value of this impedance has to be decided based on the purpose. In [49], the value of the virtual impedance is studied, in order to optimize the performance by keeping the voltage within certain limits, have sufficient reactive power sharing, system damping and decouple the active and reactive power.

A virtual impedance imitates the behaviour of an actual impedance, without losses. The converters can also be controlled as if the non-physical concept of a negative impedance is applied to the system [48]. A control circuit diagram where a virtual impedance is used is shown in Fig. 2.9 [47]. Here, $Z_v$ denotes the virtual impedance. As shown in this figure, the voltage reference is modified based on the output current and the virtual impedance. Using the classification from [48], this is an outer virtual impedance, which are used for e.g. power sharing.

In [47], a performance comparison between different kinds of outer virtual impedances are done. Here, a droop control algorithm is used, in addition to the use of virtual impedance. Simulations for resistive, inductive, inductive-resistive and resistive-capasitive virtual impedances are done, all of them dominating to the actual output impedance. The system simulated consists of three inverters operating in an island mode microgrid, where the inverters are supposed to share the power equally. With the same virtual impedance applied in the control of all the inverters, the resistive-capasitive virtual impedance loop gives the best performance. It gives a slightly better current sharing than the other alternatives, but with a lower THD for the voltage at PCC.

In [31], [50] and [51], virtual impedances are used to keep the active and reactive power in a low-voltage microgrid decoupled. This way, P-f and Q-E-droops can be used, and by this improved power sharing is obtained. This kind of micro-

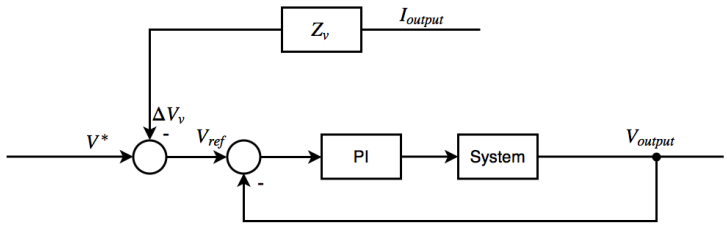


**Figure 2.9:** Block diagram showing an outer virtual impedance loop

grid has a line impedance which is mostly resistive [31]. The virtual impedance must therefore have a dominating reactive term to decouple the active and reactive power, as shown in [51].

Normally, the virtual impedances are designed to be dominating compared to the line impedance [32]. When applying a inductive-dominating term to the line impedance, the conventional droop method can be used for power sharing. A resistive virtual impedance can improve the decoupling for using the opposite droop control. Resistive and capacitive components will contribute to dampen voltage harmonics and improve stability in the grid. In [32], it is shown how a reactive virtual impedance can be used to cancel out inductive terms in the grid as well.

The use of virtual impedances for improved power sharing will be the primary focus in this work. The virtual impedances will be applied to even out the difference in line impedance between two inverters. When the virtual impedance is relatively large compared to the output impedance, an equal virtual impedance can be applied to all inverters. Also, individually selected virtual impedance for each inverter can be used to achieve an improved power sharing [32].

$$V_{ref} = V^* - Z_v \cdot I_{output} \tag{2.15}$$

However, a clear disadvantage by applying virtual impedances, are its tendency of reducing the voltage reference, as can be evident from (2.15). This is something that has to be taken into consideration when the impedance value is selected.

In [46], a table summarizing the advantages and disadvantages by virtual impedance with different kinds of droop controls are presented.

After this review on microgrid and some of their control mechanisms, the following chapters will do further investigation on this. This is done through simulations, where the next chapter will introduce the simulation models used.

# Bibliography


[1] Global emissions. https://www.c2es.org/content/international-emissions/. Accessed: 2017-12-16.

[2] Nikos Hatziargyriou et al. *Microgrids: architectures and control*. Wiley Online Library, 2014.

[3] Frede Blaabjerg, Zhe Chen, and Soeren Baekhoej Kjaer. Power electronics as efficient interface in dispersed power generation systems. *IEEE transactions on power electronics*, 19(5):1184–1194, 2004.

[4] Vannkraft. https://www.statkraft.no/Energikilder/Vannkraft/. Accessed: 2017-11-06.

[5] World electricity generation in 2015, by energy source. https://www.statista.com/statistics/269811/world-electricity-production-by-energy-source/. Accessed: 2017-11-07.

[6] Jan Machowski, Janusz W. Bialek, and James R. Bumby. *Power System Dynamics. Stability and Control*. John Wiley & Sons, 2014.

[7] Key world energy statistics. https://www.iea.org/publications/freepublications/publication/KeyWorld2017.pdf. Accessed: 2017-12-17.

[8] Ali Keyhani. *Design of Smart Power Grid Renewable Energy Systems*. John Wiley and Sons, 1st edition, 2011.

[9] Nikos Hatziargyriou, Hiroshi Asano, Reza Iravani, and Chris Marnay. Microgrids. *IEEE power and energy magazine*, 5(4):78–94, 2007.

[10] Huang Jiayi, Jiang Chuanwen, and Xu Rong. A review on distributed energy resources and microgrid. *Renewable and Sustainable Energy Reviews*, 12(9):2472–2483, 2008.

[11] Joan Rocabert, Alvaro Luna, Frede Blaabjerg, and Pedro Rodriguez. Control of power converters in ac microgrids. *IEEE transactions on power electronics*, 27(11):4734–4749, 2012.

[12] Ching-Tsai Pan and Yi-Hung Liao. Modeling and control of circulating currents for parallel three-phase boost rectifiers with different load sharing. *IEEE Transactions on Industrial Electronics*, 55(7):2776–2785, 2008.

[13] Universal bridge. `https://se.mathworks.com/help/physmod/sps/powersys/ref/universalbridge.html`. Accessed: 2017-12-02.

[14] Mohammad B Delghavi and Amirnaser Yazdani. A unified control strategy for electronically interfaced distributed energy resources. *IEEE Transactions on Power Delivery*, 27(2):803–812, 2012.

[15] Gilbert M. Masters. *Renewable and Efficient Electric Power Systems*. John Wiley and Sons, 2nd edition, 2013.

[16] Ned Mohan, Tore Undeland, and William P. Robbins. *Power electronics: converters, applications, and design*. John Wiley & Sons, 3rd edition, 2003.

[17] Daniel E Olivares, Ali Mehrizi-Sani, Amir H Etemadi, Claudio A Cañizares, Reza Iravani, Mehrdad Kazerani, Amir H Hajimiragha, Oriol Gomis-Bellmunt, Maryam Saeedifard, Rodrigo Palma-Behnke, et al. Trends in microgrid control. *IEEE Transactions on smart grid*, 5(4):1905–1919, 2014.

[18] Hua Han, Xiaochao Hou, Jian Yang, Jifa Wu, Mei Su, and Josep M Guerrero. Review of power sharing control strategies for islanding operation of ac microgrids. *IEEE Transactions on Smart Grid*, 7(1):200–215, 2016.

[19] Hassan Bevrani, Toshifumi Ise, and Yushi Miura. Virtual synchronous generators: A survey and new perspectives. *International Journal of Electrical Power & Energy Systems*, 54:244–254, 2014.

[20] Xingguo Tan, Qingmin Li, and Hui Wang. Advances and trends of energy storage technology in microgrid. *International Journal of Electrical Power & Energy Systems*, 44(1):179–191, 2013.

[21] Zhenpo Wang and Shuo Wang. Grid power peak shaving and valley filling using vehicle-to-grid systems. *IEEE Transactions on power delivery*, 28(3):1822–1829, 2013.

[22] Xing Luo, Jihong Wang, Mark Dooner, and Jonathan Clarke. Overview of current development in electrical energy storage technologies and the application potential in power system operation. *Applied Energy*, 137:511–536, 2015.

[23] Francisco Díaz-González, Andreas Sumper, Oriol Gomis-Bellmunt, and Roberto Villafáfila-Robles. A review of energy storage technologies for wind power applications. *Renewable and sustainable energy reviews*, 16(4):2154–2171, 2012.

[24] Dennis Hansen. Ieee 519 misapplications—point of common coupling issues. In *Power and Energy Society General Meeting-Conversion and Delivery of Electrical Energy in the 21st Century, 2008 IEEE*, pages 1–3. IEEE, 2008.

[25] Wei-Yu Chiu, Hongjian Sun, and H Vincent Poor. Demand-side energy storage system management in smart grid. In *Smart Grid Communications (SmartGridComm), 2012 IEEE Third International Conference on*, pages 73–78. IEEE, 2012.

[26] Xiongfei Wang, Frede Blaabjerg, and Zhe Chen. An improved design of virtual output impedance loop for droop-controlled parallel three-phase voltage source inverters. In *Energy Conversion Congress and Exposition (ECCE), 2012 IEEE*, pages 2466–2473. IEEE, 2012.

[27] Josep M Guerrero, Juan C Vasquez, José Matas, Luis García De Vicuña, and Miguel Castilla. Hierarchical control of droop-controlled ac and dc microgrids—a general approach toward standardization. *IEEE Transactions on Industrial Electronics*, 58(1):158–172, 2011.

[28] K De Brabandere, B Bolsens, J Van den Keybus, A Woyte, J Driesen, R Belmans, and K U Leuven. A voltage and frequency droop control method for parallel inverters. *Power Electronics Specialists Conference, 2004. PESC 04. 2004 IEEE 35th Annual*, 4(4):2501–2507 Vol.4, 2004.

[29] Robert H Park. Two-reaction theory of synchronous machines generalized method of analysis-part i. *Transactions of the American Institute of Electrical Engineers*, 48(3):716–727, 1929.

[30] Ned Mohan. *Advanced electric drives: analysis, control and modeling using MATLAB/Simulink*. Wiley, 2014.

[31] Lianqing Zheng, Chen Zhuang, Jian Zhang, and Xiong Du. An enhanced droop control scheme for islanded microgrids. *International Journal of Control and Automation*, 8(4):63–74, 2015.

[32] Alexander Micallef, Maurice Apap, Cyril Spiteri-Staines, Josep M Guerrero, and Juan C Vasquez. Reactive power sharing and voltage harmonic distortion compensation of droop controlled single phase islanded microgrids. *IEEE Transactions on Smart Grid*, 5(3):1149–1158, 2014.

[33] Alexandra Von Meier. *Electric power systems: a conceptual introduction*. John Wiley & Sons, 2006.

[34] Alfred Engler and Nikos Soultanis. Droop control in lv-grids. In *Future Power Systems, 2005 International Conference on*, pages 6–pp. IEEE, 2005.

[35] Josep M Guerrero, José Matas, Luis Garcia de Vicuna, Miguel Castilla, and Jaume Miret. Decentralized control for parallel operation of distributed generation inverters using resistive output impedance. *IEEE Transactions on industrial electronics*, 54(2):994–1004, 2007.

[36] Estefanía Planas, Asier Gil-de Muro, Jon Andreu, Iñigo Kortabarria, and Iñigo Martínez de Alegría. General aspects, hierarchical controls and droop methods in microgrids: A review. *Renewable and Sustainable Energy Reviews*, 17:147–159, 2013.

[37] Jaber Alipoor, Yushi Miura, and Toshifumi Ise. Distributed generation grid integration using virtual synchronous generator with adoptive virtual inertia. In *Energy Conversion Congress and Exposition (ECCE), 2013 IEEE*, pages 4546–4552. IEEE, 2013.

[38] Vu Van Thong, Achim Woyte, Mihaela Albu, Marcel Van Hest, Jan Bozelie, Javier Diaz, Tom Loix, Dan Stanculescu, and Klaas Visscher. Virtual synchronous generator: Laboratory scale results and field demonstration. In *PowerTech, 2009 IEEE Bucharest*, pages 1–6. IEEE, 2009.

[39] MPN Van Wesenbeeck, SWH De Haan, Pablo Varela, and Klaas Visscher. Grid tied converter with virtual kinetic storage. In *PowerTech, 2009 IEEE Bucharest*, pages 1–7. IEEE, 2009.

[40] Nimish Soni, Suryanarayana Doolla, and Mukul C Chandorkar. Improvement of transient response in microgrids using virtual inertia. *IEEE transactions on power delivery*, 28(3):1830–1838, 2013.

[41] Bhim Singh, Kamal Al-Haddad, and Ambrish Chandra. A review of active filters for power quality improvement. *IEEE transactions on industrial electronics*, 46(5):960–971, 1999.

[42] Radu-Florin Marinescu, Petre-Marian Nicolae, Denisa-Gabriela Firiucă, Lucian-Dinuţ Popa, Maria Diana Cristina, and Pănescu Cătălin. Aspects of power quality improvement in a driving system using an active filter. In *Modern Power Systems (MPS), 2017 International Conference on*, pages 1–6. IEEE, 2017.

[43] Amit Kumar Jindal, Arindam Ghosh, and Avinash Joshi. The protection of sensitive loads from interharmonic currents using shunt/series active filters. *Electric Power Systems Research*, 73(2):187–196, 2005.

[44] Hideaki Fujita and Hirofumi Akagi. The unified power quality conditioner: the integration of series-and shunt-active filters. *IEEE transactions on power electronics*, 13(2):315–322, 1998.

[45] Hideaki Fujita and Hirofumi Akagi. A practical approach to harmonic compensation in power systems-series connection of passive and active filters. *IEEE Transactions on industry applications*, 27(6):1020–1025, 1991.

[46] Usman Bashir Tayab, Mohd Azrik Bin Roslan, Leong Jenn Hwai, and Muhammad Kashif. A review of droop control techniques for microgrid. *Renewable and Sustainable Energy Reviews*, 76:717–727, 2017.

[47] Apap M. Micallef, A. and C. Spiteri-Staines. Performance comparison for virtual impedance techniques used in droop controlled islanded microgrids. *International Symposium on Power Electronics*, pages 695–700, 2016.

[48] Xiongfei Wang, Yun Wei Li, Frede Blaabjerg, and Poh Chiang Loh. Virtual-impedance-based control for voltage-source and current-source converters. *IEEE Transactions on Power Electronics*, 30(12):7019–7037, 2015.

[49] Xiangyu Wu, Chen Shen, and Reza Iravani. Feasible range and optimal value of the virtual impedance for droop-based control of microgrids. *IEEE Transactions on Smart Grid*, 8(3):1242–1251, 2017.

[50] Jianjun Su, Jieyun Zheng, Demin Cui, Xiaobo Li, Zhijian Hu, and Chengxue Zhang. An integrated control strategy adopting droop control with virtual inductance in microgrid. *Engineering*, 5(01):44, 2013.

[51] Jinwei He and Yun Wei Li. Analysis, design, and implementation of virtual impedance for power electronics interfaced distributed generation. *IEEE Transactions on Industry Applications*, 47(6):2525–2538, 2011.

[52] Stavros Papathanassiou, Nikos Hatziargyriou, Kai Strunz, et al. A benchmark low voltage microgrid network. In *Proceedings of the CIGRE symposium: power systems with dispersed generation*, pages 1–8, 2005.

[53] Christopher N Rowe, Terrence J Summers, Robert E Betz, David J Cornforth, and Timothy G Moore. Arctan power–frequency droop for improved microgrid stability. *IEEE Transactions on Power Electronics*, 28(8):3747–3759, 2013.

[54] Juergen K Steinke. Use of an lc filter to achieve a motor-friendly performance of the pwm voltage source inverter. *IEEE transactions on Energy Conversion*, 14(3):649–654, 1999.

[55] Patricio Cortés, Gabriel Ortiz, Juan I Yuz, José Rodríguez, Sergio Vazquez, and Leopoldo G Franquelo. Model predictive control of an inverter with output $lc$ filter for ups applications. *IEEE Transactions on Industrial Electronics*, 56(6):1875–1883, 2009.

[56] Jinwei Li, Jianhui Su, Xiangzhen Yang, and Tao Zhao. Study on microgrid operation control and black start. In *Electric Utility Deregulation and Restructuring and Power Technologies (DRPT), 2011 4th International Conference on*, pages 1652–1655. IEEE, 2011.

[57] abc to dq0, dq0 to abc. `https://se.mathworks.com/help/physmod/sps/powersys/ref/abctodq0dq0toabc.html`. Accessed: 2017-12-14.

[58] Pll (3ph). `https://se.mathworks.com/help/physmod/sps/powersys/ref/pll3ph.html?searchHighlight=pll&s_tid=doc_srchtitle`. Accessed: 2017-12-14.

[59] Jens G Balchen, Trond Andresen, and Bjarne A. Foss. *Reguleringsteknikk*. Institutt for Teknisk Kybernetikk, NTNU, 2003.

[60] Santiago Sanchez. Stability investigation of power electronics systems; a microgrid case. 2015.

[61] Dibakar Das, Gurunath Gurrala, and U Jayachandra Shenoy. Transition between grid-connected mode and islanded mode in vsi-fed microgrids. *Sādhanā*, 42(8):1239–1250, 2017.

[62] Islam Ziouani, Djamel Boukhetala, Abdel-Moumen Darcherif, Bilal Amghar, and Ikram El Abbassi. Hierarchical control for flexible microgrid based on three-phase voltage source inverters operated in parallel. *International Journal of Electrical Power & Energy Systems*, 95:188–201, 2018.

[63] Forskrift om leveringskvalitet i kraftsystemet. https://lovdata.no/dokument/SF/forskrift/2004-11-30-1557#KAPITTEL_4. Accessed: 2017-12-14.

[64] Christopher N Rowe, Terrence J Summers, Robert E Betz, Timothy G Moore, and Christopher D Townsend. Implementing the virtual output impedance concept in a three phase system utilising cascaded pi controllers in the dq rotating reference frame for microgrid inverter control. In *Power Electronics and Applications (EPE), 2013 15th European Conference on*, pages 1–10. IEEE, 2013.

[65] Ned Mohan. *Electric machines and drives: a first course*.

[66] The national smart grid laboratory. https://www.ntnu.edu/smartgrid. Accessed: 2017-12-16.

[67] What is hardware-in-the-loop simulation? https://se.mathworks.com/help/physmod/simscape/ug/what-is-hardware-in-the-loop-simulation.html. Accessed: 2017-12-17.